VAAL UNIVERSITY OF TECHNOLOGY

Zein, Collagen and PVA polymer fibre blends embedded with metal (Mn and Fe) oxide nanoparticles for wastewater treatment.

Nompumelelo Sharol Mbali Kubheka

Student number: 210008792

BTech (Chemistry)

Dissertation submitted in fulfilment of the requirement for the degree of

MAGISTER TECHNOLOGIAE: CHEMISTRY

FACULTY OF APPLIED AND COMPUTER SCIENCES

DEPARTMENT OF CHEMISTRY

Supervisor: Prof M.J Moloto (VUT, Department of Chemistry)
Co-**supervisor:** Mrs N Mkhumbeni (VUT, Department of Health Sciences)

September 2020

DECLARATION

I, Nompumelelo. S.M Kubheka, student number 210008792 declare that this Dissertation is my work. It has been submitted in the fulfilment for the degree of Magister Technologiae: Chemistry in the Faculty of Applied and Computer Sciences at the Vaal University of Technology. It has not been submitted for any degree or examination in any other university.

Signature …… Date……

DEDICATION

I would to dedicate this dissertation to my daughter, she was my strength and motivation to study further. I would also like to dedicate this dissertation to my family for what they have done for me through these years. I would not have been able to get to where I am today without their love and support. Lastly dedication to God almighty for granting me the strength and health in order make this work a possibility and for providing all the necessary resources required.

ACKNOWLEGDEMENTS

I would like to thank God, for making all impossibilities possible, for granting me good health throughout the milestones of my dissertation. I would like to thank my supervisor Prof M.J Moloto for his dedication, discipline and assistance throughout my research. The knowledge and motivation I have acquired has been immense, thank you very much Prof M.J Moloto. I would also like to thank my co-supervisor, Mrs Nolutho Mkhumbeni for her contribution to my research.

My deepest thank you to Vaal University of Technology for allowing me to utilise their resources and helping me with financial support. I would like to thank NRF for their financial support. I would also like to extend my gratitude to Ms D.S More and Ms S.C Nkabinde for their continuous mentorship in electrospinning and research, Mr E.B AttahDaniel and Mr P Ngoy for their assistance, the XRD analysis team in the department of metallurgical engineering for their assistance. Finally thank you to the NCAP and Nanotechnology research groups for all the meetings that contributed to my research.

CONFERENCES AND PUBLICATIONS

Conferences

1. Poster Presentation: Electrospin2018 5th International Conference (16-18 January 2018), silver nanoparticles embedded in the fibres of PVA/chitosan blends.
2. Oral Presentation: 3rd VUT interdisciplinary postgraduate conference (17-18 October 2018), Electrospinning of zein fibres: trials, tribulations and comparison to PVA/ chitosan.
3. Oral Presentation: 8th Annual Gauteng Nanoscience's Young Researcher's Symposium (16 November 2018), Electrospun zein nanofibres: optimizing voltage and concentration.
4. Oral Presentation: ANSO-MMU-SAJOREC INTERNATIONAL CONFERENCE (4-6 September 2019), Electrospun zein/PVA/Mn_2O_3 nanocomposite fibres as adsorbent for chrysoidine g from aqueous media
5. Poster Presentation: WOMEN IN STEM CONFERENCE (17-20 February 2020), Electrospun Mn_2O_3/ zein/PVA nanocomposite fibres as adsorbent for chrysoidine g from aqueous media

Publications

Manuscript under preparation

1. N.S.M, Kubheka, M.J Moloto and N Mkhumbeni, Fabrication of zein/ PVA fibre blends: Optimizing concentration and applied voltage, Intended journal – Fibres and polymers
2. N.S.M, Kubheka, M.J Moloto and N Mkhumbeni, Synthesis and characterisation of iron oxide and manganese oxide nanoparticles: Variable morphological and optical properties, intended journal – Journal of Nanomaterials
3. N.S.M, Kubheka, M.J Moloto and N Mkhumbeni, Structural changes of metal oxide (Fe_2O_3/ Mn_2O_3) nanoparticles embedded onto zein/PVA polymer fibre blends and their impact on applications. Intended journal – RSC Advances.

ABSTRACT

The polymer and their blended fibres provide good surface and intermolecular chemistry that bring additional functionalities and structural changes that can be adapted for new usages. Natural polymers are known to possess desirable qualities in terms of biocompatibility and biodegradability. The natural polymers are chosen due to their abundance but have difficulties in the preparations hence the addition of a synthetic polymer is vital. An important property of the polymer blended fibres is its miscibility which affects the mechanical properties, the morphology and degradation. Metal oxide nanoparticles embedded into polymer blended fibres enhances the performances of the polymer blended fibre permeability, selectivity, strength, and hydrophilicity. This study reports on the synthesis and characterization of zein, collagen nanofibres, zein/PVA fibre blends, iron oxide, manganese oxide nanoparticles, Fe_2O_3/zein /PVA and Mn_2O_3/zein/PVA fibre nanocomposite blends. The zein nanofibres and zein/PVA fibre blends were electrospun using electrospinning technique. Parameters such as the concentration and voltage were investigated. These parameters had an effect on the fibre morphology. The electrospun zein nanofibres and zein/PVA fibre blends were characterized using scanning electron microscopy (SEM), UV-Visible spectroscopy, Photoluminescence (PL), X-ray diffraction (XRD), Fourier transformer infrared (FTIR) spectroscopy and Thermal gravimetric analysis (TGA). The SEM results illustrated that an increase in the concentration of zein nanofibres improved the morphology of the fibres into ribbon like shape and had an effect on the average diameter size. The addition of PVA into zein nanofibres enhanced electrospinnabilty and the mechanical strength of zein was dependent on the presence of PVA. The optical properties, XRD, FTIR and thermal studies confirmed that zein/PVA (80/20) blend weight ratio was miscible and the other blend weight ratios remained immiscible, this was due to stronger interaction of hydrophilic performance of zein and PVA through hydrogen bonding. Therefore, fibre blend weight ratios of zein/PVA (90/10, 80/20, 70/30, 60/40 and 50/50) were successfully fabricated. The optimisation of collagen nanofibres favoured electrospraying instead of electrospinning hence collagen nanofibres could not be fabricated.

Iron oxide nanoparticles was synthesized using hydrothermal method and manganese oxide nanoparticles was synthesized through co-precipitation method. The TEM results revealed well defined shapes of metal oxide nanoparticles illustrating that the increment of temperature had an influence on the crystallinity and particle size of α-Fe_2O_3 , α-MnO_2 and α-Mn_2O_3

nanoparticles. The XRD confirmed the crystalline pattern of the metal oxide nanoparticles were of rhombohedral α-Fe_2O_3 structures (JCPDS 00-033-0664), cryptomelane phase α-MnO_2 (JCPDS No. 29-1020) and orthorhombic crystalline phase of α-Mn_2O_3 (JCPDS No. 04-007-088). The metal oxide nanoparticles were thermally stable. Three different concentrations (4.25 wt%, 4.75 wt% and 5.25 wt %) of α-Fe_2O_3 and α- Mn_2O_3 were embedded onto zein/PVA (80/20) fibre blends and electrospun. The SEM, optical properties, XRD and TGA confirmed that the embedment of metal oxide nanoparticles enhanced the zein/PVA fibre blends performance, mechanical strength and resistance to wear therefore 5.25 wt% of α-Fe_2O_3/zein/PVA and α-Mn_2O_3/zein/PVA were explored further for the adsorption of chrysoidine G removal from wastewater. The adsorption studies of zein/PVA (80/20), α-Fe_2O_3/zein/PVA and α-Mn_2O_3/zein/PVA were carried out in a batch system on the effects of contact time, pH, initial concentration and adsorbent dosage. All the nanoadsorbents could rapidly reach adsorption equilibrium within 30 min at room temperature. The maximum removal efficiency of chrysoidine G of zein/PVA, α-Mn_2O_3/zein/PVA was higher than α-Fe_2O_3/zein/PVA. The dye adsorption equilibrium data were well-fit with Langmuir isotherm rather than Freundlich isotherm. The comparison of kinetic models revealed that the overall adsorption process was described well by pseudo second-order kinetics. The polymeric materials were cost effective hence regeneration studies were implemented for three cycles. These nanoadsorbents are easily available and are expected to be economical.

TABLE OF CONTENTS

List of Figures

List of Tables

List of Abbreviations

PVA	Poly (vinyl alcohol)
PVP	Poly (vinylpyrrolidone)
PEO	Poly (ethylene) oxide
PU	Polyurethane
PANI	Polyaniline
PAN	Polyacrylonitrile
Fe_xO_y	Iron oxide
Mn_xO_y	Manganese oxide
kV	kilovolts
nm	Nanometre
HFIP	1, 1, 1, 3, 3, 3-hexafluoro-2-propanol
PBS	Phosphate-buffered saline
TFE	Trifluroethanol
Col	Collagen
CR	Congo red
AC	Activated carbon
OMS	Octahedral molecular sieves
NP	Nanoparticles
wt %	weight percentage
Fig	Figure
DW	Distilled water
SEM	Scanning Electron Microscopy
TEM	Transmission Electron Microscopy
PL	Photoluminescence
UV-vis	Ultraviolet spectroscopy
FT-IR	Fourier transformer infrared spectroscopy
XRD	X-ray Diffraction
TGA	Thermogravimetric Analysis
PFO	Pseudo-first-order
PSO	Pseudo-second order

Research outline

The research focuses on producing zein/collagen: PVA polymer nanofibre blends through electrospinning technique and investigate the removal of chrysoidine dye in wastewater. The dissertation will be divided into the following chapters which provide information on the synthesis, characterization and application of the prepared polymer fibre nanomaterials embedded with nanoparticles.

- **Chapter 1**

  This chapter provides a general background on nanotechnology, polymer fibres and polymer fibre blends, nanoparticles, polymer nanocomposites and wastewater applications for dye removal. The overall literature review on the fabrication of zein nanofibres, collagen nanofibres, zein/PVA nanofibre blends, collagen/PVA fibre blends and Synthesis of Fe_xO_y and Mn_xO_y nanoparticles is discussed in this chapter. The problem statement, aim and objectives of the study are also stated in this chapter.

- **Chapter 2**

  This chapter explains the materials used and preparation of zein nanofibres, zein/PVA blends, collagen, Fe_xO_y and Mn_xO_y nanoparticles and adsorption of chrysoidine dye. The characterization techniques are also discussed in this chapter

- **Chapter 3**

  This chapter entails the results and discussion of the fabrication of zein nanofibres, zein/PVA blends. The synthesized Fe_xO_y and Mn_xO_y nanoparticles embedded onto zein/PVA fibre blends.

- **Chapter 4**

  The results and discussion on the Adsorption of Chrysoidine dye in wastewater using iron oxide and manganese oxide nanoparticles embedded onto zein/PVA fibre blends is explained in this chapter.

- **Chapter 5**

  Conclusions and suggestions for research

CHAPTER 1

INTRODUCTION

1.1. Background

1.1.1. Nanotechnology

Nanotechnology is an assuring field that is extensively applied for advancing water and wastewater treatment with improved treatment efficiency, lower cost and energy consumption. It is considered one of the largest research, scientific and engineering innovations since the industrial revolution (Evanoff & Chumanov, 2005; Wang *et al.*, 2013; Kumar *et al.*, 2019). Nanotechnology and nanoscience has expanded in the last six decades and has therefore been studied worldwide in various applications across all other fields such as applied chemistry, biochemistry, material science and engineering (Meyer & Persson, 1998). Nanotechnology is the creation and usage of materials at the level of atoms, super molecular structures and the manipulation of their properties at the nanoscale level (Gleiter, 2000). The emergence of nanotechnology raised much attention in the past years in wastewater treatment technologies which led to the novel approach called electrospinning. Electrospinning produces polymeric nanomaterials such as zein, collagen, PVA and many other polymers embedded with nanoparticles such as manganese oxide, iron oxide etc. The advantages of electrospinning usage in the past decades are that it is a simple technique to setup (**Fig. 1-1**) and it is inexpensive. It has the potential to be utilized in various applications of numerous fields like filtration membranes (Arsuaga *et al.*, 2013), fibre based sensors, catalytic nanofibres and adsorbent nanofibres (Kayaci et al., 2013; Hong *et al.*, 2015).

1.1.2. Electrospinning process

Electrospinning is a method that utilises an electric field to fabricate the formation and deposition of polymers nanofibres from a variety of both natural and synthetic polymers. This method is proficient, fast, and cost effective (Matthews *et al.*, 2002). Electrospinning is amongst the flexible techniques used to obtain ultrafine polymer nanofibres with a range of 10 micrometres to 100 nanometres (Wang & Ryan, 2011). The scope of nanofibres has been broadened in recent years with all fibres of diameter less than 1000 nm included (Huang et al.,

2012 ; Zdraveva *et al.*, 2017) . Electrospinning process has raised attention in the last ten years because of the vast diversity of polymeric materials produced from electrospinning and also the ability to consistently spin polymer fibres in the submicron range (Züger, 2017). Polymer fibres such as zein, (PVP), poly(ethylene oxide) (PEO), silk fibroin (SF) polyurethane (PU), poly ethylene oxide (PEO), chitosan, collagen, gelatin, elastin and poly(vinyl alcohol) (PVA) fabricated from electrospinning have been implemented in a variety of applications. Example of applications include frameworks for tissue engineering, wound dressings, drug discharge materials, fibre reinforcement composites, and water treatment applications: (Reneker & Chun 1996; Ramakrishna *et al*., 2005). The advantages of electrospun polymer nanofibres are that the high surface area to volume ratio or proportions and small pores have played a vital role in fibre fabrication and hence electrospun materials have been used in adsorption and photocatalytic applications for wastewater treatment worldwide.

1.1.3. Principles of electrospinning

Electrospinning occurs when high voltage is used on the surface of a polymer solution contained in the syringe pump to create an electrically charge jet. Depending on the type of application field, natural polymers like zein, collagen and synthetic polymers like PVA have an electrically charge that overcomes the surface tension of the polymer solution and it is discharged as a jet. The charge build-up causes a protrusion to appear on the end of the droplet, altering the solution droplet into a conical shape known as the Taylor cone (Reznik *et al.*, 2004; (Taylor, 1969). A standard electrospinning set up (Fig. 1-1) consist of a syringe, a metallic (copper) needle, a superior voltage power supply and a fibre collector (Huang *et al.*, 2003).

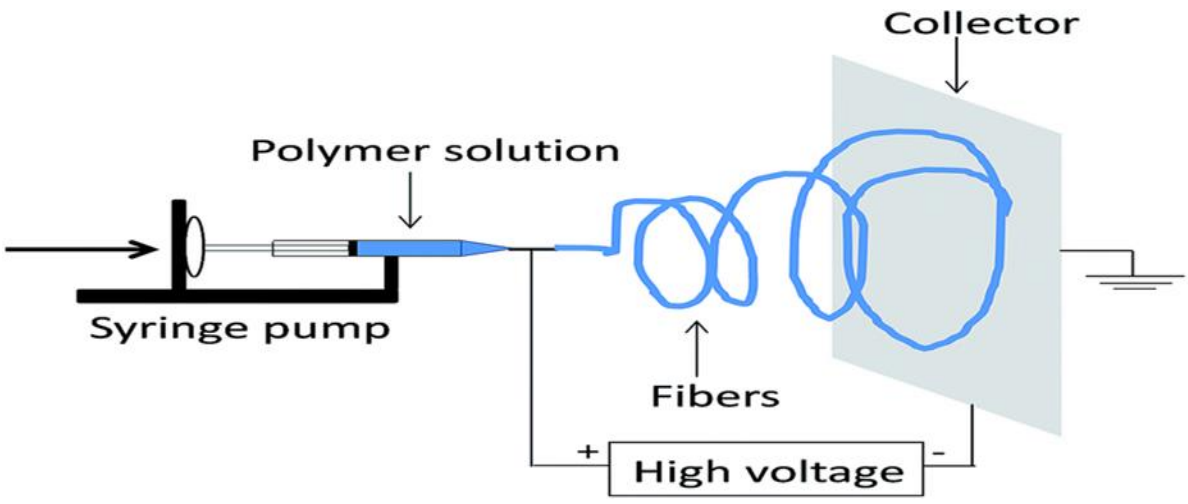

Fig. 1-1. Schematic representation of the electrospinning set-up (Tas et al., 2015)

There are various parameters that influence electrospinning therefore making uniform polymer fibre fabrication and reproducibility challenging. The parameters can be classified into three categories namely: solution parameters, process parameters and ambient parameters, the effects on fibre morphology are detailed on **Table 1.1**.

Table 1.1. Electrospinning Parameters (Solution, Processing and Ambient) and their Effects on fibre Morphology (Bhardwaj & Kundu, 2010).

Parameters	Effects on fibre morphology
Solution parameters	The higher concentration and the more viscous the polymer solution the fibre diameter increases which lead to disappearance of beads on the fibre morphology. The number of beads decreases with increasing molecular weight, whereas the high conductivity of the solution and surface tension plays a vital role in lowering the fibre diameter producing a stable polymer jet.
Process parameters	The high applied voltage decreases the fibre diameter, and the generation of beads is produced when a distance is too short or too large, therefore, a minimum distance is required from the tip to the collector. The low flow rate is favourable for small fibre diameter and limitation of beads formation thus promoting uniform fibre formation.
Ambient parameters	High humidity results in circular pores on the fibres and increasing the temperature results in decrease in fibre diameter.

In order to understand the nature of electrospinning, the choice of polymer has an effect on the desired application such as adsorption. Therefore natural polymers like zein and collagen have amphiphilic, hydrophilic, biocompatible, biodegradable and non-toxic properties. Such properties of natural polymers are suitable for wastewater treatment applications especially when cross-linked with a synthetic polymer such as PVA because it water soluble, contains high mechanical strength, and it has low toxicity (Zhang *et al.*, 2005; Qureshi *et al.*, 2017; Tian *et al.*, 2017) . Various researchers have studied the effect of polymers to improve wastewater treatment which has been a global challenge affecting the environment and health of people because of toxic effluents such as chrysoidine dye released by textile industries (Lofrano *et al.*, 2016; Yin & Deng, 2015).

1.1.4. Polymer fibres and their blends

Fibres can be classified as natural or man-made substances that are significantly longer than wide. Polymer fibres are a subset of man-made fibres which are based on synthetic chemicals rather than natural materials through physical process. Examples of polymer fibres are polyamide nylon, polyethylene, polyvinyl chloride, polyvinyl alcohol, chitosan, zein, cellulose, polyacrylamide etc. Polymer fibre blends are a mixture of at least two polymers interacting through interdiffusion. There are several examples of polymer fibre blends such as collagen-PEO, polyaniline (PANI)/PEO blend, PVP/zein, polyaniline/polystyrene, silk/PEO, chitosan/PVA (Huang *et al.*, 2003; Jiang *et al.*, 2012). The fabrication of natural (zein and collagen) polymer fibres including synthetic polymers (PVA) and polymer fibre blends has gained much attention for the development of innovative nanomaterials with properties that are suitable to address the challenges related to wastewater treatment. Polymer nanofibres are fibres with very small fibre diameters of less than 1000 nm (Huang *et al*., 2012). Polymer nanofibres have different functionalities and properties such as the large surface-to-area ratio, high porosity, flexibility and stability (Agarwal *et al*., 2008). The morphology of the nanofibres is a great probable solution for numerous environmental applications (Thavasi et al., 2008). The fabrication of polymers or polymer fibre blends is a good alternative and inexpensive process compared to other unselective techniques for wastewater treatment. Therefore polymer fibres can be good adsorbents to capture chrysoidine dye.

1.1.5. Nanoparticles and polymer nanocomposites

Nanoparticles are materials that are widely used which include particulate substances that have at least one dimension less than 100 nm (Laurent *et al.*, 2008). Nanoparticles are complex molecules that consist of three layers i.e. (a) the surface layer, which may entail a variety of small molecules, metal ions, and polymers. (b) The shell layer, which is a chemically different material from the core in all features, and (c) the core, which is basically the central portion of the nanoparticles also referred as the nanoparticle itself (Shin *et al.*, 2016). Nanoparticles can also be referred as polymer nanoparticles or polymer nanocomposites, these are nanoparticles that are mostly nanospheres or nanocapsular shaped (Mansha *et al.*, 2017). Nanocomposite materials are a multiphase material which at least one dimension of the constituent phases is <100 nm (Tesh & Scott, 2014; Yin & Deng, 2015a). Nanocomposite are commonly fabricated by loading desired nanoparticles onto various supporting materials, such as polymers or membranes. Polymer nanocomposites contain remarkable features of both nanoparticles and

polymers. Polymer nanocomposites consist of unique physical and chemical properties, the high interfacial reactivity of nanofillers, exceptional mechanical properties and compatibility owing to their polymer matrix (Pan *et al.*, 2009; Zhao *et al.*, 2011). Incorporation or embedding of inorganic nanoparticles into the polymer fibres has been considered a way to make polymeric nanomaterials more attractive to be commercialized. Polymer nanocomposites are providing new solutions and opportunities to ensure sustainable energy and environments for the future. Therefore in this study low concentrations of iron oxide and manganese oxide nanoparticles will be embedded into polymer fibre blends. The addition of the chosen metal oxide nanoparticles was attributed by the multifunctionality of iron oxide and manganese oxide nanoparticles such as thermal stability, improving of mechanical strength, endurance, hydrophilicity, magnetic properties and enhancement of polymer fibres as adsorbents.

1.1.6. Wastewater treatment applications.

Nanotechnology and nanoscience exhibit a great perspective for advancing water and wastewater treatment with improved treatment efficiency, lower energy consumption and cost. Applications of nanotechnology in water and wastewater treatment, i.e., adsorption, separation, catalytic oxidation, ozonation, electrocoagulation, aerobic degradation, disinfection and sensing are amongst many techniques used to improve wastewater treatment challenges (Zhang *et al*., 2016). These techniques are classified as physical, chemical, electrochemical or biological treatment methods for effective removal of dyes from wastewater (**see Table 1.2**). The coagulation-flocculation technique is commonly used in textile wastewater treatment plants to remove dyes and organic pollutants (Golob *et al*., 2005) . However, this method increases sludge production and results to incomplete dye removal *(Riera-Torres et al*., 2010). Ozonation on the other hand has a short half-life between 20 to 30 minutes which demands continuous application resulting in it being a cost intensive process (Salleh *et al.*, 2011; Galdeano *et al.*, 2018). Therefore some of the wastewater treatment techniques have limitations such as the production of toxic sludge, high operational cost, and technical limitations (García *et al*., 2014).

Techniques such as nanofiltration and ultrafiltration have been previously implemented for the removal of azo dyes. These techniques also have limitations such as membrane clogging that decrease the flux due to the low biodegradability of dyes. Dyes are classified into three broad categories: (a) anionic direct- reactive, azo dyes and acidic dyes, (b) cationic-all basic dyes and (c) non-ionic-dispersed dyes (Purkait *et al.*, 2004). The chemical classes of dyes used more

frequently on industrial scale are the azo, anthraquinone, sulfur, indigoid, triphenylmethyl (trityl), and phthalocyanine. There are 12 classes of chromogenic groups the most common being that of azo type which consist of 60-70% of all textile dye stuff produced (Salleh *et al.*, 2011). The dye molecules that consist of chromophore components are responsible for the production of colors which fix the dye onto or within the fibres or textiles dye stuff. Effluents containing such dyes results in major environmental problems because it also affects the people who may use effluents for living purposes such as washing, bathing and drinking (Sharma & Sobti, 2000; Bée *et al.*, 2017). In wastewater treatment there is no single process that provides adequate treatment hence a combination of different processes is often used to achieve the desired water quality in the most economical way (Crini & Badot, 2008). Therefore, it has been recognized that adsorption using low-cost adsorbents is an effective and economic method for water decontamination (Nadaroglu *et al*., 2010).

Table 1.2. Different methods of dye removal from wastewater (Crini & Badot, 2008; Khandare & Govindwar, 2015)

Physical Physical/Chemical	• Adsorption • Flocculation- coagulation • Membranes • Irradiation • Ion exchange
Chemical	• Ozonation • Advanced Oxidation Processes • Catalytic degradation • Chemical precipitation • Reduction
Electrochemical	• Electrocoagulation • Indirect oxidation
Biological	• Fungal degradation • Algal treatment • Anaerobic and Aerobic digestion • Microbial fuel cells

Adsorption is a phase transfer process that is commonly used to remove substances from a gas or liquid phase. **Fig 1-2**. A typical example of chrysoidine (azo dye) adsorption on a polymeric nanocomposite materials.

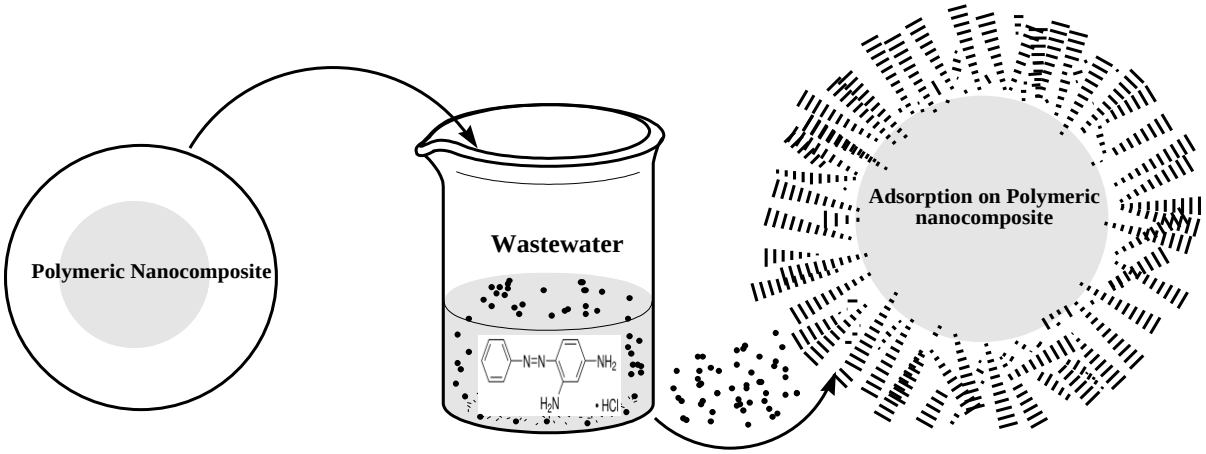

Fig. 1-2. Schematic diagram of adsorption on polymeric nanocomposite material (Khan et al., 2016)

Adsorption is an economically viable application that is vital for the removal of dye in wastewater because it is a physical and a chemical process extensively used to eliminate azo dyes from wastewater. The removal of dye (pollutant) in wastewater is essentially important for the achievement of clean water and a sustainable environment. Therefore removal of dye by adsorption is an alternative process because of extraordinary effectiveness and capability. Adsorption is a suitable method for large-scale applicability and it has minimal sludge production (Bée *et al.*, 2017). It is less costly than other separation methods and the easy operational systems are less affected by the contaminated materials (Chakraborty *et al.* 2003; Nollet *et al.* 2003 & Lin *et al.* 2012). Adsorption has created opportunities for polymers and polymer nanocomposites enabled in wastewater treatment (Zhang et al., 2016).

1.2. Literature review

1.2.1. Nanomaterials in wastewater treatment

Wastewater loaded with dye from fabric, medicinal, laser printing, parchment industries is amongst serious science-related concerns, which affect our environment (Ogugbue & Sawidis, 2011; El-Zawahry *et al.*, 2016). There are a various chemical dyes employed more frequently on an industrial scale, namely azo, anthraquinone, sulphur, indigoid, triphenylmethyl (trityl) and phthalocyanine derivatives (Forgacs et al., 2004). The occurrences of these colorants in wastewater are problematic to remove due to their complicated chemical structure (Tang *et al.*, 2014) and inappropriately, there are no authorised rules that demonstrate the acceptable restrictions of dye discharges from the industries (Hessel *et al.*, 2007). Therefore the emergence of nanomaterials and polymer fibres has created opportunities for the exploration of potential adsorption implementations to limit or eliminate the presence of dyes in wastewater. There are numerous nanofabrication techniques that have been implemented in the previous years.

Electrospinning is amongst the various techniques, which is receiving enormous attention nowadays due to its consistent removal of contaminant without fabrication of any harmful derivatives, particularly in decontaminated water purification processes (Ng *et al.*, 2013). Electrospinning is a technique used to produce polymer fibres, nanocomposites embedded with metal oxides or nanoparticles. The advantages of polymer fibres are that they form better control of pore size, are highly flexible, there is less space required for setting up as they are less costly than inorganic fibres. Polymer fibres composed of metal oxides or nanoparticles are drawing interest in the market because of their high robustness (i.e. permeability, selectivity, strength and hydrophilicity) in numerous water sanitisation applications or systems (Skluzacek *et al.* 2007; Bottino et al., 2001; Aerts *et al.*, 2001). There are different types of natural and synthetic polymers that hold a great potential for advancing water and wastewater treatment with improved treatment efficiency. In this study, nanomaterial's will be used for the adsorption of dye in wastewater will be natural polymers such zein, collagen and synthetic polymer (vinyl alcohol), metal oxides such as iron oxide and manganese oxide nanoparticles which will be embedded on the polymer fibre blends.

1.2.2. Natural and synthetic polymer fibres

Zein is an amorphous natural polymer that is amphiphilic, it has a large fraction of nonpolar amine and carboxyl functional groups. **Fig 1-3** illustrates the composition of the amide bond linked to the carboxyl functional groups and zein is aquaphobic (Qureshi *et al.* 2017). It was first discovered in 1897 due to its solubility in aqueous alcohol (Osborne, 1897). Zein is a dried "yellowish" powder obtained from grinded maize or corn. It is a protein mixture of four classes: $\alpha, \beta, \gamma \; and \; \delta$ which are expressed sequentially in maize and are found to interact with each other to reach stabilization (Torres-giner *et al.*, 2008). Zein possesses excellent properties of being renewable, biodegradable and biocompatible (Shukla & Cheryan, 2001;Yao *et al*., 2006). Miyoshi et al. (2005) studied the preparation of ultrafine fibrous zein membranes via electrospinning. It was reported that zein nanofibres were produced from 80 wt% ethanol solution and the diameter obtained was 700 nm. It was further reported that the morphology of the beads and fibres was affected by parameters such as polymer concentration and electric field. Zein fibres were mainly generated above a polymer concentration of 21 wt% when spun at 15kV to 30 kV.

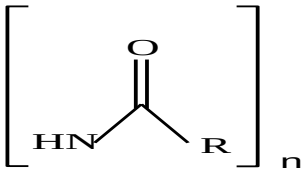

Fig. 1-3. The molecular structure of zein.

Fabrication of zein nanofibres and crosslinking by electrospinning was reported previously in a number of studies (Selling *et al.*, 2007a; Xu *et al.*, 2008; Jiang and Yang, 2011; Karthikeyan *et al.*, 2012; Neo *et al.*, 2012; Zhang *et al.*, 2014). In the past two decades zein has attracted much attention in decontaminated water purification processes such as treating dye that reacts fast in contaminated water, which alters the exterior morphology into resonating sphere-shape to creating a larger area of interaction to confine dye (El-Zawahry *et al.* 2016). Zein contains numerous groups with lone pairs of electrons and partial negative charges. These groups allow protein molecules to absorb metal ions or dyes through electrostatic interaction and/or chelation. Their ''positive" interactions with heavy metal ions can further exert their actions in treating wastewater provided that these functional groups can be converted into electrospun nanofibre mats. The mats can provide huge porosity and large surface areas for the contact of heavy metal ions/ dyes with the functional groups on the nanofibres' surface, thereby resulting

in higher levels of functional performance (Wen *et al.*, 2016). Qureshi *et al*. (2017) studied the electrospun zein nanofibre as green and recyclable adsorbent for the removal of reactive black 5 (RB5) from aqueous phase. It was reported that the zein nanofibres that lead to the RB5 adsorption were predominantly electrostatic contained hydrogen bonding and aquaphobic. The nanofibres of zein were approved to be an adaptable green nanoadsorbent material due to its high surface area, large number of exposed active sites and environmentally pleasant nature. Wen *et al*. (2016) conducted a study on zein nanoribbons, which were electrospun for treatment of lead present in wastewater. It was reported that nanoribbon mats of zein showed efficient performance in lead adsorption experiments. The equilibrium of adsorption was reached within one hour; therefore, it proved that these nanomaterials have a great potential in polluted water treatment applications.

Collagen is the most abundant connective tissue protein in animals. There are around 16 different types of collagen in the human body but 80 - 90% of the body collagen consists of type I, II, and III. Matthews *et al.* (2003) studied collagen type I, II, and III solubilization in HFIP and electrospun from solutions at 0.05g/ mL^{-1} concentration and higher. It was reported that HFIP solvent played a vital role in collagen solubilization, with the two trifluoro- methyl groups assisting in breakage of hydrophobic interactions and the mildly acidic secondary alcohol hydroxyl assisting in breaking hydrogen bonding. **Fig. 1-4** shows the structure orientation of the functional groups of collagen.

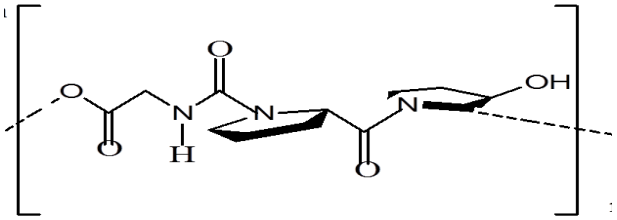

Fig. 1-4. The molecular structure of collagen.

Collagen has been studied extensively in biomedical and tissue engineering applications and limited research has been implemented on collagen for the application of wastewater treatment (Davis & Maffia 1995; Kwon & Matsuda 2005; Zhong *et al.* 2005; Zeugolis *et al.* 2008; Haugh *et al*. 2009 & Chakrapani *et al.* 2012). Dong *et al.*, (2009) studied the preparation of collagen nanofibres obtained from phosphate-buffered saline (PBS) and C_2H_6O in the presence of NaCl. It was observed that 16 wt% of collagen was soluble when the NaCl was 5 wt% or greater. Therefore a high salt concentration decreased the average fibre diameter. Castilla-casadiego *et al.*(2016) studied the production of collagen nanofibres from acetic acid with controlled fibre

diameter, orientation, and mechanical properties. It was reported that the secondary structure of collagen was successfully preserved when using acetic acid as the solvent and the modulation of fibre diameter in a range of ≈175–400 nm was obtained. The collagen nanofibres were obtained without any cross-linker or plasticizer. Therefore the report suggested that weak acids such as acetic acid can be considered as an attractive solvent for the production of collagen nanofibres because they enhance the formation of stable nanofibres with uniform morphology that maintains collagen's secondary structure without any distortion. Kazanci (2014) studied the solvent and temperature effects on folding of electrospun collagen nanofibres. It was reported that collagen was extremely sensitive to temperature variation hence this could be one of the reasons for the discrepancy in experimental results in literature and there was no real success of obtaining electrospun collagen nanofibres from acidic solvents. Therefore the stipulated research studies demonstrated electrospinning as a versatile technique to produce collagen nanofibres and illustrated the effect of varying different parameters during electrospinning for successful fabrication of collagen nanofibres.

Polyvinyl alcohol (PVA) is a synthetic polymer that has a regular structure with a backbone composed of carbon-carbon bonds and hydroxyl groups , it has been mainly used in fibre and film products for many years (Zhang *et al.* 2005). Moreover, PVA (**Fig. 1-5**) is hydrophilic, biocompatible, is non-toxic and exhibits surface active properties (Dobritoiu & Patachia 2013) moreover, it can reportedly protect bacteria (El-Naas *et al*. 2009) . Furthermore, owing to its good fibre-forming ability due to the presence of hydroxyl groups in PVA chains, which have the capability to generate hydrogen bond with many anions which enhances the solubility of the natural polymers or metal salt in the PVA solution. PVA has been chosen as a polymer additive to produce electrospun nanofibrous mats (Zhang *et al.*, 2005; Islam & Rezaul, 2010).

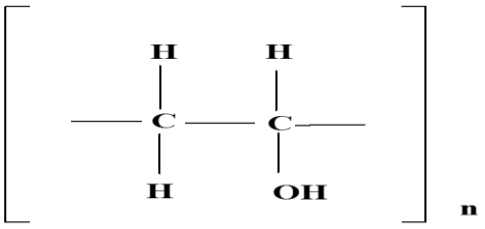

Fig. 1-5. The molecular structure of PVA

Electrospun polymer fibres from several proteins share similar disadvantages, namely the low mechanical strength mainly when saturated and their poor morphological strength in liquid which causes a decrease on the exterior and pore volumes. The mentioned disadvantages limit

the electrospinning of protein fibre applications, therefore, zein and collagen need to be blended with other polymers (PVA) to improve the mechanical properties and water stability of protein fibres (Barnes *et al.*, 2007; Vrana *et al.*, 2007; Sisson *et al.*, 2009). Nevertheless, one of the major issues concerned about the zein/PVA system is its compatibility. Polymer-polymer interaction and compatibility was previously studied by (Bui & Choi, 2017; Polacco *et al.*, 2015; Nakazawa *et al.*, 2016), it was evident that blends from zein/PVA polymers were not fully miscible, there were weak interactions at the molecular level, on condition of the fraction of a certain composition or the preparation processing (Kun & Pukánszky, 2017). Therefore, modification of PVA through crosslinking could improve compatibility (Chang *et al.*, 2017). Blencowe *et al.* (2009) studied the core cross-linked star polymers via controlled radical polymerisation and proved that certain hydroxyl-based cross-linkers and amino-based cross-linkers could be well cross-linked with blends from polymer. Miscibility of collagen/PVA nanofibres is not a major concern except that the choice of solvent plays a vital role in the production of the blended polymer fibres. Zhang et al. (2015) studied electrospinning and rheological behaviour of poly (vinyl alcohol)/collagen blended solutions using acetic acid as a solvent because it is environmentally friendly and does not denature the structure of collagen. It was reported that (PVA/COL) micro-nanofibres were successfully prepared and the fibre diameter of the electrospun mats decreased with increasing content of collagen, hence concentration of collagen in the sample solutions had an effect in the diameter and morphology of the fibres.

Zhang et al. (2016) studied the electrospun and crosslinking of COL/PVA nanofibre-microsphere containing salicylic acid for drug delivery. The results obtained showed that COL/PVA-SA efficiently controlled the release of drugs by the crosslinking of UV-radiation, but the morphology was destroyed when meeting water. Therefore this illustrates that the polymers were instable in water since there are both hydrophilic in nature. Al-kahtani *et al.* (2017) studied gelatin/CuS/ PVA nanocomposites for the photo degradation of rhodamine B dye in wastewater using solar light as a form of irradiation. It was reported that photocatalytic degradation of the dye under solar light showed good results at low initial concentration and the nanocomposites were of the pseudo-first-order kinetics. The investigation showed that the nanocomposites could be effective and suitable photocatalysts for eliminating rhodamine B dye from wastewater using the degradation method. There are several studies on electrospun natural/synthetic blended nanofibres but limited studies on the incorporation of nanoparticles onto zein/collagen/PVA nanofibres for adsorption of dye in wastewater or aqueous media.

Therefore, this study suggests the potential of nanoparticles to improve the limitations of natural/synthetic polymer blends. The incorporation of the nanoparticles is thought to improve the stability of fibers or their blends as well as improving the effectiveness of the polymer materials for their applications.

1.2.3. Synthesis of iron oxide nanoparticles and iron oxide/polymer nanocomposite for wastewater treatment

Iron oxide nanoparticles are widely used due to their low cost, easy separation and enhanced stability (Carabante *et al.* 2009; Fan *et al.* 2012). Iron oxide is one of the most important transition metal oxide. Iron oxide exhibits different phases such as FeO, α-Fe_2O_3, γ -Fe_2O_3, β -Fe_2O_3 and Fe_3O_4. There are several methods to synthesis iron oxide nanoparticles such as chemical precipitation (Glisenti, 1998), hydrothermal reaction (Chen *et al.*, 2002; Li *et al.*, 2007) sol–gel method (Huo *et al.*, 2005), solvothermal method (Zhang *et al.*, 2014) etc. Lassoued *et al.* (2018) conducted a study on the synthesis, photoluminescence and magnetic properties of iron oxide (α-Fe_2O_3) nanoparticles through precipitation or hydrothermal methods. It was reported that the prepared hematite nanoparticles through hydrothermal method had the smallest size (21 nm), best crystallinity, highest band gap (1.94–2.10 eV) and best value of saturation magnetization compared to the hematite elaborated by the precipitation method. The hematite nanoparticles that were prepared from hydrothermal method had potential for investigations of photocatalytic applications in effluent water treatment. Incorporation of nanoparticles into polymer matrix allows the development of new features that differs from the pure materials. Hoque et al. (2018) studied the fabrication and comparative study of magnetic Fe and α-Fe_2O_3 nanoparticles dispersed hybrid polymer (PVA+Chitosan) novel nanocomposite film. It was reported that the synthesized α-Fe_2O_3 nanoparticles possessed better magnetic properties than the Fe nanoparticles. The iron oxide dispersed (16.67 wt.%) nanocomposite α-Fe_2O_3/PVA/Chitosan showed the highest tensile strength and elastic modulus than the PVA polymer alone, therefore, the fabricated nanocomposite was considered to be useful for various biomedical applications.

Iron oxide nanoparticles have a promising approach for various high-technological applications such as catalysis, adsorption, pigments, sensors and biomedical applications. Khedr et al. (2009) studied the photocatalytic degradation of ($C_{32}H_{24}N_6O_6S_2$) dye using nanoparticles of iron oxide. The nanoparticles were prepared by thermic vaporisation and co-precipitation

method. The supreme elimination proficiency was 96 percent at 100 nanometre in size. The radiation had no noticeable effects on the disintegration of the catalytic aptitude, although the speed of degradation had accelerated when light was present. Wang *et al*. (2007) studied the gold/ iron oxide aerogels, which were used as photocatalysts to disperse blue 79 azo dye in water under ultraviolet light illumination. The blending of metals with iron oxide nanoparticles led to the increment of the oxidation-reduction reaction kinetics and was certainly an effective method for photocatalytic improvement. Umar *et al.* (2011) studied the high yield synthesis of well-crystalline Fe_2O_3 nanoparticles. It was reported that structural characterizations revealed that the nanoparticles were almost spherically shaped with average diameters of 35±5 nm. It was further confirmed that the nanoparticles exhibited good photocatalytic properties on the photocatalytic decomposition of methylene blue. Afkhami & Moosavi (2010) studied the adsorptive removal of Congo red, a carcinogenic textile dye, from aqueous solutions by maghemite nanoparticles. The adsorption isotherm data for the CR was derived at room temperature and treated according to Langmuir and Freundlich models. Langmuir model was more successful in representing experimental isotherm data for the adsorption of CR on maghemite nanoparticles and was considered a good adsorbent material.

Dyes are amongst various contaminants which are visible to observe in water. Different industries such as such as plastics, leather, pharmaceutical, food, cosmetics, and textiles utilize dyes to color the produced products. As a results considerable pollution on wastewater is generated. Therefore fabrication of nanocomposite adsorbents is necessary to eliminate decontamination caused by dyes in water or aqueous media. The nanoparticles incorporated into polymer fibres increases the performances of the fibres such as absorptivity (pore size), and hydrophilicity including the magnetic properties possessed by nanoparticles, which makes them a distinct choice for adsorption or decolourisation of different dyes (Joo & Zhao 2017). Several studies have been conducted in the past about the effectiveness of iron nanoparticles incorporated into polymeric nanomaterials for wastewater treatment. Zhua et al. (2014) conducted a study on novel magnetically separable γ -Fe_2O_3/crosslinked chitosan adsorbent it was reported that the magnetic γ -Fe_2O_3/crosslinked chitosan composite adsorbents exhibited faster adsorption rate towards methyl orange compared with crosslinked chitosan. The adsorption kinetics followed the pseudo-second-order therefore the obtained experimental results were remarkable for the adsorption of methyl orange. Greenstein et al. (2018) studied performance comparison of hematite (α-Fe_2O_3)-polymer composite and core-shell nanofibres as point-of-use filtration platforms for metal sequestration. It was reported that the performance

of embedded (PAN/Fe_2O_3) and core-shell (PAN/Fe_2O_3@Fe_2O_3) composites for adsorption of As (V), Cr(VI), Cu(II), and Pb(II) generally matched expectations from more traditional iron oxide sorbents across a range of initial metal concentrations, pH values and metal uptake on embedded nanofibres increased with α-Fe_2O_3 loading. It was further concluded that these materials were a promising approach as a nano-enabled technology for point-of-use water treatment.

1.2.4. Synthesis of manganese oxide nanoparticles and manganese oxide/polymer nanocomposite for wastewater treatment

Manganese oxide (MnO_x) constituents have attained attention due to its usage in comprehensive applications because it has unique magnetic properties (Sessoli *et al.* 1993; Wernsdorfer *et al.* 2002), catalytic activity (Zouni, 2001) and high energy density (Thackeray *et al.* 2005; Yabuuchi & Komaba 2014; Nitta *et al.* 2015). MnO_2 has numerous types of polymorphic characteristics, such as alpha, beta, sigma and omega type, contributing significant physical and chemical properties, as the [MnO_6] octahedron correlates in diverse ways. Among the polymorph, the alpha MnO_2 are commonly utilised as nano-catalysts (Li *et al*. 2005). Soejima et al. (2018) studied the preparation of uniform sized MnO_x nanoparticles. The nanoparticles were characterised after the preparation and chemical reactivity was further studied. It was reported that the obtained manganese oxides monodisperse nanostructures have proved to have oxidative degradation ability for RhB dye in acid solution conditions with no preservatives like chemically reacting agents and detectable light radiation.

Thota et al. (2010) conducted a study on formation and magnetic behaviour of manganese oxide nanoparticles. It was reported that the magnetic susceptibility data revealed antiferro-magnetic nature for Mn_2O_3, Mn_5O_8 and MnO with the Néel temperature of 75 K, 131 K and 115 K, respectively and an orthorhombic to cubic crystallographic transition for Mn_2O_3 at 310 K. Therefore manganese oxalate dihydrate ($MnC_2O_4 \cdot 2H_2O$) was successfully synthesized by sol–gel process. Its decomposition yielded Mn_2O_3 and MnO nanoparticles as major phase(s) in oxygen or air and nitrogen or argon environment, respectively. Porous magnetic manganese oxide nanostructures were studied by Chen *et al.* It was reported that manganese oxide nanostructures were successfully synthesized by mixing oleic acid capped Fe_3O_4 nanoparticles in a $KMnO_4$ solution at a relatively low temperature. The synthesized manganese oxide nanostructures exhibited strong magnetism which makes this material an easy and efficient

choice for separation means in wastewater treatment under an external magnetic field. Manganese oxides nanoparticles and manganese oxide nanocomposites have attracted a great deal of attention to remove organic dye pollutants due to their unique structures and physio-chemical properties. Numerous studies have been conducted about the removal of dye by various manganese oxides nanoparticles or (Mn_yO_x) nanocomposites through adsorption and catalytic degradation.

Chen *et al.* (2010) conducted a study on the synthesis and pseudocapacitive studies of composite films of polyaniline and manganese oxide nanoparticles. It was reported that the presence of surface modified MnO_2 nanoparticles increased the active surface area of the PANI and MnO_2 composite film thereby enhanced the electrochemical performance. Therefore MnO_2 nanoparticles improved the morphology of PANI which also provides useful insights for developing new nanocomposite structures. Kannan *et al.* (2011) conducted a study on synthesis and catalytic studies of layered and OMS type nano manganese oxide materials. It was reported that the manganese oxide of both types (layer and OMS) proved to be an excellent material for the decolorization of methylene blue & acid black 10 dye. Among the two octahedral molecular sieve (OMS) type showed slightly better efficiency than layer MnO_2, which could have been attributed by the intercalation of the dye molecule into the layered structure. Therefore the produced material was promising approach for kinetics of the decolorization of dyes. Cui *et al*. (2015) studied the different Mn_xO_y for the decolourisation of rhodamine B dye and influence of crystal type and solution pH, it was reported that the colour removal efficiencies of the dye for the three manganese oxides all increased with decline in pH of the solution. Hence, the results indicated that three manganese oxides, particularly α-MnO_2, could have potential in degradation of dye pollutants. Khan *et al.* (2019) studied manganese dioxide nanoparticles/activated carbon composite as efficient UV and visible light photocatalyst and it was reported that MnO_2 NPs had a cylindrical and spherical shape. The Mn/AC composite degraded about 98.53% of Congo red dye within 5 min while MnO_2 NPs degraded 66.57% of dye within the same irradiation time. Both photocatalysts were highly active, which might be due to the presence of various mineral ions in tap water. It was conclusive that the NPs were well dispersed on the surface of AC which had a great contribution to the activity of the photocatalyst under visible light. Numerous studies have been reported over the past years about dye degradation or adsorption from wastewater using either nanocomposites/ composites as adsorbents of dye and photocatalysts. The innovation of nanocomposites/ composite materials are a promising approach for the removal of dyes in wastewater or aqueous media.

1.2.5. Adsorption of chrysoidine dye

Chrysoidine **(Fig. 1-6**) is a type of azo dye that is basic and an organic molecule with unsaturated groups. Chrysoidine is recognised as a cancer-causing agent that results in acute and persistent harm to mammals if it is consumed orally or administered to the skin (Reyns *et al*. 2010). It is made up from a group of atoms known as a chromophore, which are large groups of molecules that absorb light at a particular frequency to impart colour. Chromophores have unsaturated groups such as C=O and –N=N–, which are often delocalised electron systems involving aromatic rings (Johns et al. 2003).

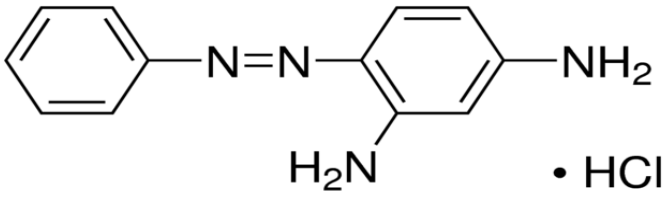

Fig. 1-6. Molecular structure of chrysoidine dye

Matheswaran & Karunanithi (2007) studied adsorption capacity of dye by utilising the fly residue obtained from the thermal power plant in batch method. The fly residue was an effectual adsorbing material for eliminating chrysoidine R dye from polluted water. It had been reported that dye contained in the wastewater was effectively detached from the sedimentary solution utilising the fly residue method. Chrysoidine R adsorptivity on fly residue was successful by the adsorption kinetic model of pseudo-first-order. Their research revealed that fly residue had the potential to be a productive adsorbent material for colorant elimination. Some researchers (Purkait *et al*. 2010; Nurchi *et al.* 2014) conducted studies on chrysoidine dye and concluded adsorption as an efficient and effective method to eliminate the presence of dye in wastewater. Purkait et al. (2004) conducted a study on the adsorption behavior of chrysoidine dye on activated charcoal and its regeneration characteristics by using different surfactant. It was reported that the adsorption of chrysoidine dye was more at the basic pH and the percentage adsorption increased with an increase in time for the different initial dye concentrations. Freundlich isotherm and pseudo second-order kinetics was found to be suitable for chrysoidine adsorption onto AC. Hence, it was concluded that dyes like chrysoidine, were very sensitive to the pH of the solution.

Bagheri et al. (2015) studied CuS-NP-AC that was utilised as an adsorbent for the enhanced elimination of chrysoidine G aided by ultrasonic. Three adsorption kinetic models were assessed and more than 94 percent chrysoidine G dye had been eliminated by using little amounts of adsorbing material (0.03g of CuS-NP-AC) in a short period of six minutes and the Langmuir kinetic model had the best symmetrical data. Waqar et al. (2019) studied the adsorption of textile dye (chrysoidine) from aqueous solutions using activated sawdust. The experimental results revealed that sawdust had a high adsorption efficiency, and the adsorption of chrysoidine followed Freundlich isotherm. It was concluded that raw sawdust proved to be slightly less efficient in comparison to chemically treated sawdust. Although in economic terms, raw sawdust is more cost-effective as the difference in the percent dye removal was less than the difference in the manufacturing costs. Based on previous research studies conducted the removal of chrysoidine dye in wastewater or aqueous media is essential.

1.3. Problem statement

Polymeric materials and nanoparticles have been utilized for the removal of dyes in wastewater due to good physio-chemical properties such as pore forming mechanism, higher flexibility, chemical stability and relatively low costs. However, these nanomaterials have limitations such as permeability, selectivity and low resistance to fouling (Yin & Deng, 2015). Therefore the development of polymer nanocomposites has proven to be an effective and promising approach in wastewater treatment (Yin & Deng, 2015; Lofrano et al., 2016; Zhang et al., 2016). One of the major global challenges to sustain the modern society is to secure sufficient water resources of desirable quality for various designated uses. The presence of synthetic dyes in wastewater cause considerable environmental pollution due to large-scale production and extensive application. Chrysoidine dye is an azo dye known to be potentially toxic and carcinogenic due to its complex chemical structure which is difficult to remove (Reyns et al. 2010). Hence, cost-effective nanomaterials and technologies are essential to extend water resources and solve water pollution problems. This study seeks to make use of polymer nanocomposites that will eliminate or reduce the organic dye presence in wastewater in order to make our surrounding environment sustainable and health risk free. The study is focused on synthesising zein, collagen and PVA nanofibres embedded with Fe_xO_y and Mn_xO_y nanoparticles to determine which material will be effective for adsorption of chrysoidine dye for wastewater treatment.

1.4. Aim and Objectives

The research aims to produce zein/collagen: PVA polymer nanofibre blends through electrospinning technique and investigate the removal of chrysoidine dye in wastewater by achieving the following objectives.

- To prepare zein and collagen polymer fibres by optimising concentration and voltage using the electrospinning technique.
- To prepare zein/PVA and collagen/PVA fibre blends by varying concentration, voltage and distance of the solution to the collector.
- To characterise the prepared zein, collagen, PVA nanofibre mats using SEM, XRD FTIR spectroscopy and TGA.
- To synthesise the Fe_xO_y and Mn_xO_y nanoparticles and characterise them using a combination of TEM, UV-vis spectroscopy, PL, XRD and TGA.
- To incorporate the Fe_xO_y and Mn_xO_y nanoparticles in the polymer fibre blends.
- To characterise the incorporated polymer fibre composite blends using SEM, UV-vis spectroscopy, PL, XRD, FTIR spectroscopy and TGA.
- To investigate the chemical removal of chrysoidine dye in wastewater using UV-vis spectroscopy using selected fibre composite blended materials.

1.6. References

Aerts, P., Greenberg, A.R., Legsen, R., Krantz, W.B., Reinsch, V.E and Jacobs, P.A. (2001). The influence of filler concentration on the compaction and filtration properties of Zirfon®-composite ultrafiltration membranes. *Separation and Purification Technology*, 22–23, pp. 663–669. doi: 10.1016/S1383-5866(00)00165-9.

Afkhami, A. and Moosavi, R. (2010). Adsorptive removal of Congo red , a carcinogenic textile dye , from aqueous solutions by maghemite nanoparticles. *Journal of Hazardous Materials* 174, 174, pp. 398–403. doi: 10.1016/j.jhazmat.2009.09.066.

Al-kahtani, A. A. (2017). Photocatalytic Degradation of Rhodamine B Dye in Wastewater Using Gelatin / CuS / PVA Nanocomposites under Solar Light Irradiation, pp. 66–82. doi: 10.4236/jbnb.2017.81005.

Bagheri, A. R., Ghaedi, M., Hajati, S., Ghaedi, a.M., Goudarzi, A and Asfaram, A. (2015). RSC Advances Random forest model for the ultrasonic-assisted removal of chrysoidine G by copper sulfide nanoparticles loaded on activated carbon ; response surface methodology approach. *RSC Advances*. Royal Society of Chemistry, 5, pp. 59335–59343. doi: 10.1039/C5RA08399K.

Barnes, C. P., Pemble, D., Simpson, D.G and Bowlin, G.L. (2007). Cross-Linking Electrospun Type II Collagen Tissue Engineering Scaffolds with Carbodiimide in Ethanol. *Tissue Engineering*, 13(7), pp. 1593–1605. doi: 10.1089/ten.2006.0292

Bée, A., Obeid, L., Mbolantenaina, R., Welschbillig, M., & Talbot, D. (2017). Magnetic chitosan/clay beads: A magsorbent for the removal of cationic dye from water. *Journal of* Magnetism and Magnetic Materials, 421, pp. 59–64. doi: 10.1016/j.jmmm.2016.07.022

Bhardwaj, N., & Kundu, S. C. (2010). Electrospinning : A fascinating fiber fabrication technique. *Biotechnology Advances 28*, pp. 325–347. doi: 10.1016/j.biotechadv.2010.01.004

Blencowe, A. Tan, J., Goh, T.K., Qiao, G.G. (2009). Core cross-linked star polymers via controlled radical polymerisation. *Polymer*. Elsevier Ltd, 50(1), pp. 5–32. doi: 10.1016/j.polymer.2008.09.049.

Bottino A, Capannelli G, D'Asti V, P. P. (2001). Preparation and properties of novel organic–inorganic porous membranes. *Separation and Purification Technology*, 22–23(1–2), pp. 269–

275. doi: 10.1016/S1383-5866(00)00127-1.

Bui, V. and Choi, H. (2017). Surface Morphology and Wettability Control of Polymer Substrates : A Comparison of Water- Miscible and Water-Immiscible Mixture Solvents. *European Polymer Journal*. 98, pp. 158-166. doi: 10.1016/j.eurpolymj.2017.05.039.

Carabante, I., Grahn, M., Holmgren, A., Kumpiene, J., Hedlund, J. (2009). Adsorption of As (V) on iron oxide nanoparticle films studied by in situ ATR-FTIR spectroscopy. *Colloids and Surfaces A: Physicochemical and Engineering Aspects*, 346(1–3), pp. 106–113. doi: 10.1016/j.colsurfa.2009.05.032.

Castilla-casadiego, D. A. Ramos-Avilez, H,V, Herrera-Posada, S., Calcagno, Barbara, Loyo, L., Shipmon, J., Acevedo, A., Quintana, A., Almodovar, J. (2016). Engineering of a Stable Collagen Nanofibrous Scaffold with Tunable Fibre Diameter, Alignment, and Mechanical Properties. *Materials and Engineering Macromolecular*, 301(9), pp. 1064-1075. doi: 10.1002/mame.201600156.

Chakraborty, S., Purkait, M. K., DasGupta, S., De, S., & Basu, J. K. (2003). Nanofiltration of textile plant effluent for color removal and reduction in COD. *Separation and Purification Technology*, *31*(2), pp. 141–151. doi:10.1016/S1383-5866(02)00177-6

Chang, C. , Wang, T., Hu, Q., Luo, Y. (2017). Caseinate-zein-polysaccharide complex nanoparticles as potential oral delivery vehicles for curcumin: Effect of polysaccharide type and chemical cross-linking. *Food Hydrocolloids*. Elsevier Ltd., 72, pp. 254-262. doi: 10.1016/j.foodhyd.2017.05.039.

Chen, H., Chu, P.K., He, J, Hu, T., Yang, M. (2011). Porous magnetic manganese oxide nanostructures: Synthesis and their application in water treatment. *Journal of Colloid and Interface Science*. Elsevier Inc., 359(1), pp. 68–74. doi: 10.1016/j.jcis.2011.03.089.

Chen, L., Sun, L., Luan, F., Liang, Y., Li,Y., Liu, X. (2010). Synthesis and pseudocapacitive studies of composite films of polyaniline and manganese oxide nanoparticles. *Journal of Power Sources*. Elsevier B.V., 195(11), pp. 3742–3747. doi: 10.1016/j.jpowsour.2009.12.036.

Chen, L. X., Lui, T., Thurnauer, M.C, Csencsits, R. and Rajh, T. (2002). Fe_2O_3 Nanoparticle Structures Investigated by X-ray Absorption Near-Edge Structure , Surface Modifications , and Model Calculations. *Journal of Phys. Chem*, 106, pp. 8539–8546.

Crini, G., & Badot, P. M. (2008). Application of chitosan, a natural aminopolysaccharide, for dye removal from aqueous solutions by adsorption processes using batch studies: A review of recent literature. *Progress in Polymer Science (Oxford)*, 33(4), pp. 399–447. doi: 10.1016/j.progpolymsci.2007.11.001

Davis, J. F. and Maffia, G. J. (1995). Collagen dispersions for liquid-solid separations in water treatment and sludge dewatering. *Separations Technology* , 5, pp. 147–152.

Dobritoiu, R. and Patachia, S. (2013). Applied Surface Science A study of dyes sorption on biobased cryogels. *Applied Surface Science*. Elsevier B.V., 285, pp. 56–64. doi: 10.1016/j.apsusc.2013.07.164.

Dong, B., Arnoult, O., Smith, M.E, Wnek, G.E.. (2009). Electrospinning of collagen nanofibre scaffolds from benign solvents. *Macromolecular Rapid Communications*, 30(7), pp. 539–542. doi: 10.1002/marc.200800634.

El-Naas, M. H., Al-Muhtaseb, S. A. and Makhlouf, S. (2009). Biodegradation of phenol by Pseudomonas putida immobilized in polyvinyl alcohol (PVA) gel. *Journal of Hazardous Materials*, 164(2–3), pp. 720–725. doi: 10.1016/j.jhazmat.2008.08.059.

El-Zawahry, M. M. , Abdelghaffar, F., Abdelghaffar, R.A., Ahmed, G. (2016). Equilibrium and kinetic models on the adsorption of Reactive Black 5 from aqueous solution using Eichhornia crassipes/chitosan composite. *Carbohydrate Polymers*. Elsevier Ltd., 136, pp. 507–515. doi: 10.1016/j.carbpol.2015.09.071.

El-Naas, M. H., Al-Muhtaseb, S. A., & Makhlouf, S. (2009). Biodegradation of phenol by Pseudomonas putida immobilized in polyvinyl alcohol (PVA) gel. *Journal of Hazardous Materials*, *164*(2–3), pp. 720–725. doi:10.1016/j.jhazmat.2008.08.059

El-Zawahry, M. M., Abdelghaffar, F., Abdelghaffar, R. A., & Hassabo, A. G. (2016). Equilibrium and kinetic models on the adsorption of Reactive Black 5 from aqueous solution using Eichhornia crassipes/chitosan composite. *Carbohydrate Polymers*, *136*, pp. 507–515. doi:10.1016/j.carbpol.2015.09.071

Evanoff, D. D., & Chumanov, G. (2005). Synthesis and optical properties of silver nanoparticles and arrays. *ChemPhysChem*, *6*(7), pp. 1221–1231. doi:10.1002/cphc.200500113

Fan, F. L., Qin, Z., Bai, J., Rong, W. D., Fan, F. Y., Tian, W., Wu, X. L., Wang, Y., & Zhao,

L. (2012). Rapid removal of uranium from aqueous solutions using magnetic Fe_3O_4@SiO_2composite particles. *Journal of Environmental Radioactivity*, *106*, pp. 40–46. doi: 10.1016/j.jenvrad.2011.11.003

Ferreira, K. N., Iverson, T. M., Maghlaoui, K., & Barber, J. (2004). Architecture of the Photosynthetic Oxygen-Evolving Center. *Science*, *303*(19), pp. 1831–1839. dio: 10.1126/science.1093087

Forgacs, E., Cserháti, T., & Oros, G. (2004). Removal of synthetic dyes from wastewaters: A review. *Environment International*, *30*(7), pp. 953–971. doi:10.1016/j.envint.2004.02.001

Galdeano, M. C., Wilhelm, A. E., Goulart, I. B., Tonon, R. V., Freitas-Silva, O., Germani, R., & Chávez, D. W. H. (2018). Effect of water temperature and pH on the concentration and time of ozone saturation. *Brazilian Journal of Food Technology*, *21*, pp. 1–7. doi:10.1590/1981-6723.15617

García E.R, Medina R.L , Lozano M.M , Pérez I.H, V. M. . and M. F. (2014). Adsorption of Azo-Dye Orange II from Aqueous Solutions Using a Metal-Organic Framework Material: Iron- Benzenetricarboxylate. *Materials*, 7(12), pp. 8037–8057. doi:10.3390/ma7128037

Gleiter, H. (2000). Nanostructured materials: basic concepts and microstructure . Acta Maaterialia, *48*, pp. *1-29*.

Glisenti, A. (1998). Interaction of formic acid with FeO powders under di † erent atmospheres : an XPS and FTIR study. *J. Chem. Soc., Faraday Trans.*, *94*, 3671–3676.

Golob, V., Vinder, A., & Simonič, M. (2005). Efficiency of the coagulation/flocculation method for the treatment of dyebath effluents. *Dyes and Pigments*, *67*(2), pp. 93–97. doi:10.1016/j.dyepig.2004.11.003

Greenstein,K.E., Myung, N.V., Parkin, G.F, Cwiertny, D. M. (2018). Performance comparison of hematite (α-Fe_2O_3)-polymer composite. *Water Research*, 137, pp. 3–42. doi: 10.1016/j.watres.2018.10.048

Haugh, M. G., Jaasma, M. J. and O'Brien, F. J. (2009). The effect of dehydrothermal treatment on the mechanical and structural properties of collagen-GAG scaffolds. *Journal of Biomedical Materials Research - Part A*, 89(2), pp. 363–369. doi: 10.1002/jbm.a.31955.

Hessel, C., Allegre, M., Maisseu,M., Charbit, F., Moulin, P. (2007). Guidelines and legislation for dye house effluents. *Journal of Environmental Management*, 83(2), pp. 171–180. doi: 10.1016/j.jenvman.2006.02.012.

Hong, G., Li, X., Shen, L., Wang, M., Wang, C., Yu, X., & Wang, X. (2015). High recovery of lead ions from aminated polyacrylonitrile nanofibrous affinity membranes with micro/nano structure. *Journal of Hazardous Materials*, *295*, pp. 161–169. doi:10.1016/j.jhazmat.2015.04.020

Hua-Yue Zhua, Ru Jiang, Ling Xiao, W. L. (2010). A novel magnetically separable gamma-Fe_2O_3/crosslinked chitosan adsorbent : preparation , characterization and adsorption application for removal of hazardous azo dye. *Journal of Hazardous Materials*, *179*(2010), pp. 251–257.

Huang, F., Wei, Q., & Cai, Y. (2012). Surface functionalization of polymer nanofibers. In Functional Nanofibers and their Applications. Woodhead Publishing Limited. pp. 92-118. doi:10.1533/9780857095640.1.92

Huang, Z., Zhang, Y., Kotaki, M., & Ramakrishna, S. (2003). A review on polymer nanofibers by electrospinning and their applications in nanocomposites. *Composite Science and Technology 63(15)*, pp. 2223–2253. doi:10.1016/S0266-3538(03)00178-7

Huo, L., Li, Q., Zhao, H., Yu, L., Gao, S., & Zhao, J. (2005). Sol – gel route to pseudocubic shaped α -Fe_2O_3 alcohol sensor : preparation and characterization. *Sensors and Actuators B*, *107*, pp. 915–920. doi:10.1016/j.snb.2004.12.046

Islam, S., & Rezaul, M. (2010). : Physicochemical and Engineering Aspects Fabrication and characterization of poly (vinyl alcohol)/ alginate blend nanofibers by electrospinning method. *Colloids and Surfaces A, 366*, pp.135–140.doi:10.1016/j.colsurfa.2010.05.038

Jiang, Q., & Yang, Y. (2011). Water-Stable Electrospun Zein Fibers for Potential Drug Delivery. *Journal of Biomaterials Science, Polymer Edition*, *22(10)*, pp. 37–41. doi:10.1163/092050610X508437

Jiang, Y., Mo, H., & Yu, D. (2012). Electrospun drug-loaded core – sheath PVP / zein nanofibers for biphasic drug release. *International Journal of Pharmaceutics*, *438*(1–2), pp. 232–239. doi:10.1016/j.ijpharm.2012.08.053

Johns C , Miroslav M, H. P. (2003). Highly sensitive indirect photometric detection of cations by capillary electrophoresis with the cationic dye chrysoidine. *Journal of Chromatography A*, *997*(1–2), pp. 87–94. doi:10.1016/S0021-9673(03)00062-1

Joo, S. H., & Zhao, D. (2017). Environmental dynamics of metal oxide nanoparticles in heterogeneous systems: A review. *Journal of Hazardous Materials*, *322*, pp. 29–47. doi:10.1016/j.jhazmat.2016.02.068

Kannan, R., Jegan, A., Ramasubbu, A., Karunakaran, K., & Vasanthkumar, S. (2011). Synthesis and catalytic stuides of layered and oms type nano manganese oxide material. *Digest Journal of Nanomaterials and Biostructures*, *6*(2), pp.755–760.

Karthikeyan, K., Guhathakarta, S., Rajaram, R., & Sai, P. (2012). Electrospun zein / eudragit nanofibers based dual drug delivery system for the simultaneous delivery of aceclofenac and pantoprazole. *International Journal of Pharmaceutics*, *438*(1–2), pp. 117–122. doi:10.1016/j.ijpharm.2012.07.075

Kayaci, F., Aytac, Z., & Uyar, T. (2013). Surface modification of electrospun polyester nanofibers with cyclodextrin polymer for the removal of phenanthrene from aqueous solution. *Journal of Hazardous Materials*, 261. pp. 286-294 doi:10.1016/j.jhazmat.2013.07.041

Kazanci, M. (2014). Solvent and temperature effects on folding of electrospun collagen nano fibers. *Materials Letters*, *130*, pp. 223–226. doi:10.1016/j.matlet.2014.05.114

Khan, I., Sadiq, M., Khan, I., & Saeed, K. (2019). Manganese dioxide nanoparticles / activated carbon composite as efficient UV and visible-light photocatalyst. *Environmental Science and Pollution Research*, *26*, pp. 5140–5154. doi:10.1007/s11356-018-4055-y

Khandare, R., & Govindwar, S. (2015). Spectrophotometric method for optical band gap and electronic transitions determination of semiconductor materials. *Environmental Waste Management*, pp. 399–439. doi:10.1201/b19243-15

Khedr, M. H., Halim, K. S. A., & Soliman, N. K. (2009). Synthesis and photocatalytic activity of nano-sized iron oxides. *Materials Letters*, *63*(6–7), pp. 598–601. doi:10.1016/j.matlet.2008.11.050

Kumar, V. V., Lee, J., Yoong, K., Esmaeely, R., Sankunny, N., & Gurusamy, S. (2019).

Electrospun nanofiber interleaving in fiber reinforced composites. *Materials and Processing Communications*, 1(1), pp. 1–8. doi:10.1002/mdp2.24

Kun, D., & Pukánszky, B. (2017). Polymer/lignin blends: interactions, properties, applications. In *European Polymer Journal*, 9, pp. 618-641. doi:10.1016/j.eurpolymj.2017.04.035

Kwon, I. K., & Matsuda, T. (2005). Co-electrospun nanofiber fabrics of poly(L-lactide-co-ε-caprolactone) with type I collagen or heparin. *Biomacromolecules*, *6*(4), pp. 2096–2105. doi:10.1021/bm050086u

Lassoued, A., Lassoued, M. S., Dkhil, B., Ammar, S., & Gadri, A. (2018). Synthesis, photoluminescence and Magnetic properties of iron oxide (α-Fe_2O_3) nanoparticles through precipitation or hydrothermal methods. *Physica E: Low-Dimensional Systems and Nanostructures*, *101*, pp. 212–219. doi:10.1016/j.physe.2018.04.009

Laurent, S., Forge, D., Port, M., Roch, A., Robic, C., Elst, L. Vander, & Muller, R. N. (2008). Magnetic Iron Oxide Nanoparticles : Synthesis , Stabilization , Vectorization , Physicochemical Characterizations , and Biological Applications. *Chemical Reviews*, 108(6), pp. 2064–2110.

Li Z, Ding Y, Xiong Y,Yang Q, X. T. (2005). One-step solution-based catalytic route to fabricate novel α-MnO_2 hierarchical structures on a large scale. *Chem. Commun.*, *7*, pp. 918–920. doi:10.1039/B414204G

Lili Li, Y. C. and Y. L. D. (2007). Synthesis and characterization of ring-like α-Fe_2O_3 nanpoarticles. *Nanotechnology*, 18(2007), pp. 1–7. doi:10.1088/0957-4484/18/10/105603

Lin, J., Li, C., Zhao, Y., Jianchan, H amd Zhang, L. (2012). Co-electrospun Nanofibrous Membranes of Collagen and Zein for Wound Healing. *ACS Appl. Mater. Interfaces,* 4, pp. 1050-1057.

Lofrano, G., Carotenuto, M., Libralato, G., Domingos, R. F., Markus, A., Dini, L., Gautam, R. K., Baldantoni, D., Rossi, M., Sharma, S. K., Chattopadhyaya, M. C., Giugni, M., & Meric, S. (2016). Polymer functionalized nanocomposites for metals removal from water and wastewater: An overview. *Water Research*, *92*, pp. 22–37. doi:10.1016/j.watres.2016.01.033

Hoque,M .A, Ahmed, M.R. , Rahman, G.T. , Rahman, M.T. , Islam, M.A. , Mubarak A.,

Khan, M. K. H. (2018). Fabrication and comparative study of magnetic Fe and α-Fe_2O_3 nanoparticles dispersed hybrid polymer (PVA+Chitosan) novel nanocomposite film. *Results in Physics*, 10, pp. 434–443. doi:10.1016/j.rinp.2018.06.010.

Mansha, M., Khan, I., Ullah, N., & Qurashi, A. (2017). Synthesis , characterization and hydrogen evolution reaction of carbazole-containing conjugated polymers. *International Journal of Hydrogen Energy,* 420(16), pp 10952-10961. doi:10.1016/j.ijhydene.2017.02.053

María Arsuaga, J., Sotto, A., del Rosario, G., Martínez, A., Molina, S., Teli, S. B., & de Abajo, J. (2013). Influence of the type, size, and distribution of metal oxide particles on the properties of nanocomposite ultrafiltration membranes. *Journal of Membrane Science, 428*, pp.131–141. doi:10.1016/j.memsci.2012.11.008

Matheswaran, M., & Karunanithi, T. (2007). Adsorption of Chrysoidine R by using fly ash in batch process. *Journal of Hazardous Materials*, *145*, pp. 154–161. doi:10.1016/j.jhazmat.2006.11.006

Matthews, J. A., Boland, E. D., Wnek, G. E., Simpson, D. G., & Bowlin, G. L. (2003). Compatible Polymers Electrospinning of Collagen. *Journal of Bioactive and Compatible Polymers*, *18*(125), pp. 125–134. doi:10.1177/088391103033856

Matthews, J. A., Wnek, G. E., Simpson, D. G., & Bowlin, G. L. (2002). Electrospinning of Collagen Nanofibers. *Biomacromolecules*, *3*, pp. 232–238. doi:10.1021/bm015533u

Meyer, M., & Persson, O. (1998). Nanotechnology - interdisciplinarity, patterns of collaboration and differences in application. *Scientrometrics*, *42*(2), pp. 195–205.

Miyoshi, T., Toyohara, K., & Minematsu, H. (2005). Preparation of ultrafine fibrous zein membranes via electrospinning. *Polym Int*, *54*, pp. 1187–1190. doi:10.1002/pi.1829

Nadaroglu, H., Kalkan, E., & Demir, N. (2010). Removal of copper from aqueous solution using red mud. *Desalination*, *251*(1–3), pp. 90–95. doi:10.1016/j.desal.2009.09.138

Nakazawa, T., Ikoma, A., Kido, R., Ueno, K., Dokko, K., & Watanabe, M. (2016). Effects of compatibility of polymer binders with solvate ionic liquid electrolytes on discharge and charge reactions of lithium-sulfur batteries. *Journal of Power Sources*, *307*, pp. 746–752. doi:10.1016/j.jpowsour.2016.01.045

Neo, Y. P., Ray, S., Easteal, A. J., Nikolaidis, M. G., & Quek, S. Y. (2012). Influence of

solution and processing parameters towards the fabrication of electrospun zein fibers with sub-micron diameter. *Journal of Food Engineering*, *109*(4), pp. 645–651. doi:10.1016/j.jfoodeng.2011.11.032

Ng, L. Y., Mohammad, A. W., Leo, C. P., & Hilal, N. (2013). Polymeric membranes incorporated with metal/metal oxide nanoparticles: A comprehensive review. *Desalination*, *308*, pp. 15–33. doi:10.1016/j.desal.2010.11.033

Nitta, N., Wu, F., Lee, J. T., & Yushin, G. (2015). Li-ion battery materials: Present and future. *Materials Today*, *18*(5), pp. 252–264. doi:10.1016/j.mattod.2014.10.040

Nollet, H., Roels, M., Lutgen, P., Van Der Meeren, P., & Verstraete, W. (2003). Removal of PCBs from wastewater using fly ash. *Chemosphere*, *53*(6), pp. 655–665. doi:10.1016/S0045-6535(03)00517-4

Nurchi, V. M., Crespo-Alonso, M., Pilo, M. I., Spano, N., Sanna, G., & Toniolo, R. (2014). Sorption of ofloxacin and chrysoidine by grape stalk. A representative case of biomass removal of emerging pollutants from wastewater. *Arabian Journal of Chemistry*, *12*(7), pp. 1141–1147. doi:10.1016/j.arabjc.2015.01.006

Ogugbue, C. J., & Sawidis, T. (2011). Bioremediation and Detoxification of Synthetic Wastewater Containing Triarylmethane Dyes by *Aeromonas hydrophila* Isolated from Industrial Effluent. *Biotechnology Research International*, *2011*, pp. 1–11. doi:10.4061/2011/967925

Pan, B., Pan, B., Zhang, W., Lv, L., Zhang, Q., & Zheng, S. (2009). Development of polymeric and polymer-based hybrid adsorbents for pollutants removal from waters. Chemical Engineering*, 151*, pp. 19–29. https://doi.org/10.1016/j.cej.2009.02.036

Polacco, G., Filippi, S., Merusi, F., & Stastna, G. (2015). A review of the fundamentals ofpolymer-modified asphalts: Asphalt/polymer interactions and principles of compatibility. *Advances in Colloid and Interface Science*, *224*, pp. 72–112. doi:10.1016/j.cis.2015.07.010

Purkait, M. K., Gusain, D. S., & Dasgupta, S. (2004). Adsorption Purkait, M. K., Gusain, D.S, DasGupta, S. and De, S. Adsorption behavior of chrysoidine dye on activated charcoal and its regeneration characteristics by using different surfactants. *Separation Science and Technology*, 39(10), pp. 2419–2440. doi: 10.1081/SS-120039347.

Purkait, M. K., Gusain, D. S. and Dasgupta, S. (2010). Adsorption Behavior of Chrysoidine Dye on Activated Charcoal and Its Regeneration Characteristics by Using Different Surfactants Adsorption Behavior of Chrysoidine Dye on activated charcoal and its regeneration characteristics by using different surfactant. *Separation Science and Technology* , 39(10), pp. 2419-2440,. doi: 10.1081/SS-120039347.

Qureshi, U. A., Khatri, Z., Ahmed, F., Khatri,M. and Kim, I. (2017). Electrospun Zein Nano fibre as a Green and Recyclable Adsorbent for the Removal of Reactive Black 5 from the Aqueous Phase. *ACS Sustainable Chem. Eng*., 5, pp. 4340-4351. doi:10.1021/acssuschemeng.7b00402.

Ramakrishna S, Fujihara K, Teo W.E, L. T. . and M. Z. (2005). An Introduction to Electrospinning and Nanofibers. *Front Matter*, *35*, i–xi. doi:0.1142/9789812567611_fmatter

Reyns, T., Fraselle, S., Laza, D., & Van Loco, J. (2010). Rapid method for the confirmatory analysis of chrysoidine in aquaculture products by ultra-performance liquid chromatography-tandem mass spectrometry. *Biomedical Chromatography*, *24*(9), pp. 982–989. doi:10.1002/bmc.1396

Reznik, S. N., Yarin, A. L., Theron, A., & Zussman, E. (2004). Transient and steady shapes of droplets attached to a surface in a strong electric field. *Journal of Fluid Mechanics*, *516*, pp. 349–377. doi:10.1017/S0022112004000679

Riera-Torres, M., Gutiérrez-Bouzán, C., & Crespi, M. (2010). Combination of coagulation-flocculation and nanofiltration techniques for dye removal and water reuse in textile effluents. *Desalination*, *252*(1–3), pp. 53–59. doi:10.1016/j.desal.2009.11.002

Salleh, M. A. M., Mahmoud, D. K., Karim, W. A. W. A., & Idris, A. (2011). Cationic and anionic dye adsorption by agricultural solid wastes: A comprehensive review. *Desalination*, *280*(1–3), pp. 1–13. doi:10.1016/j.desal.2011.07.019

Selling, G. W., Biswas, A., Patel, A., Walls, D. J., Dunlap, C., & Wei, Y. (2007). Impact of Solvent on Electrospinning of Zein and Analysis of Resulting Fibers. *Macromolecular Chemistry and Physics*, 208, pp. 1002–1010. doi:10.1002/macp.200700056

Sessoli, R., Gatteschi, D., Caneschi, A., & Novak, M. A. (1993). Magnetic bistability in a metal-ion cluster. *Nature*, *365*(6442), pp. 141–143. doi:10.1038/365141a0

Sharma, M. K., & Sobti, R. C. (2000). Rec effect of certain textile dyes in Bacillus subtilis. *Mutation Research - Genetic Toxicology and Environmental Mutagenesis*, *465*(1–2), pp. 27–38. doi:10.1016/S1383-5718(99)00201-6

Shin, W., Cho, J., Kannan, A. G., Lee, Y., & Kim, D. (2016). Cross-linked Composite Gel Polymer Electrolyte using Mesoporous Methacrylate- Functionalized SiO_2 Nanoparticles for Lithium-Ion Polymer Batteries. *Nature Publishing Group*, *pp.* 1–10. doi:10.1038/srep26332

Shukla, R., & Cheryan, M. (2001). Zein : the industrial protein from corn. *Industrial Crops and Products*, *13*, pp. 171–192.

Sisson, K., Zhang, C., Farach-Carson, M. C., Chase, D. B., & Rabolt, J. F. (2009). Evaluation of cross-linking methods for electrospun gelatin on cell growth and viability. *Biomacromolecules*, *10*(7), pp. 1675–1680. doi:10.1021/bm900036s

Skluzacek, J. M., Tejedor, M. I. and Anderson, M. A. (2007). NaCl rejection by an inorganic nanofiltration membrane in relation to its central pore potential. *Journal of Membrane Science*, 289(1–2), pp. 32–39. doi: 10.1016/j.memsci.2006.11.034

Soejima, T., Nishizawa, K. and Isoda, R. (2018). Journal of Colloid and Interface Science Monodisperse manganese oxide nanoparticles : Synthesis , characterization , and chemical reactivity. *Journal of Colloid And Interface Science*. Elsevier Inc., 510, pp. 272–279. doi: 10.1016/j.jcis.2017.09.082.

Tang, L. , Cai, Ye., Yang, G., Liu, Y., Zeng, G., Zhou, Y., L, S., Wang, J., Zhang, S., Fang, Y., He, Y. (2014). Cobalt nanoparticles-embedded magnetic ordered mesoporous carbon for highly effective adsorption of rhodamine B, *Applied Surface Science*. Elsevier B.V., 314, pp. 746–753. doi: 10.1016/j.apsusc.2014.07.060.

Tas S, Kaynan O, Ozden-Yenigun E, N. K. (2016). Polyacrylonitrile (PAN)/crown ether composite nanofibers for the selective adsorption of cations. *RSC Advances*, *6*, pp. 3608–3616. doi:10.1039/C5RA23214G

Taylor, G. (1969). Electrically Driven Jets. *Proceedings of the Royal Society A: Mathematical, Physical and Engineering Sciences*, *313*(1515), pp. 453–475. doi:10.1098/rspa.1969.0205

Tesh, S. J., & Scott, T. B. (2014). Nano-composites for water remediation: A review. *Advanced Materials*, *26*(35), pp. 6056–6068. doi:10.1002/adma.201401376

Thackeray, M. M., Johnson, C. S., Vaughey, J. T., Li, N. & Hackney, S. A. (2005). Advances in manganese-oxide 'composite' electrodes for lithium-ion batteries. *Journal of Materials Chemistry*, *15*(23), pp. 2257. doi:10.1039/b417616m

Thavasi, V., Singh, G., & Ramakrishna, S. (2008). Electrospun nanofibers in energy and environmental applications. *Energy and Environmental Sciences*, pp. 205–221. doi:10.1039/b809074m

Osborne, T.B, (1897). The amount and properties of the proteids of maize kernel. *Journal of the American Chemical Society*, *19*(7), pp. 525–532.

Thota, S., Prasad, B., & Kumar, J. (2010). Formation and magnetic behaviour of manganese oxide nanoparticles. *Materials Science & Engineering B*, *167*(3), pp. 153–160. doi:10.1016/j.mseb.2010.01.049

Tian, H., Yan, J., Rajulu, A. V., Xiang, A., & Luo, X. (2017). Fabrication and properties of polyvinyl alcohol/starch blend films: Effect of composition and humidity. *International Journal of Biological Macromolecules*, *96*, pp. 518–523. doi:10.1016/j.ijbiomac. 2016.12.067

Torres-giner, S., Gimenez, E. and Lagaron, J. M. (2008). Characterization of the morphology and thermal properties of Zein Prolamine nanostructures obtained by electrospinning. *Food Hydrocolloids*, 22, pp. 601–614. doi: 10.1016/j.foodhyd.2007.02.005.

Umar, A., Abaker, M., Faisal, M., Hwang, S.W., Baskoutas,S. and Al-Sayari, S.A. (2011). High-Yield Synthesis of Well-Crystalline -Fe_2O_3 Nanoparticles : Structural , Optical and Photocatalytic Properties. *Journal of Nanoscience and Nanotechnology*, 11, pp. 3474–3480. doi: 10.1166/jnn.2011.4148.

Vrana, N. E., Bullies, N., Kocak, H., Gulay, P., Justin, V., Malbouyres, M., Ruggiero, f., Damour, O. and Hasirci, V. (2007). EDC/NHS cross-linked collagen foams as scaffolds for artificial corneal stroma. *Journal of Biomaterials Science, Polymer Edition*, 18(12), pp. 1527–1545. doi: 10.1163/156856207794761961.

Wang, C. T. (2007). Photocatalytic activity of nanoparticle gold/iron oxide aerogels for azo dye degradation. *Journal of Non-Crystalline Solids*, 353(11–12), pp. 1126–1133. doi: 10.1016/j.jnoncrysol.2006.12.028.

Wang, L., & Ryan, A. J. (2011). Introduction to electrospinning. *Electrospinning for Tissue Regeneration*, pp. 3–33. doi:10.1016/B978-1-84569-741-9.50001-X

Wang, X., Ding, B., & Li, B. (2013). Biomimetic electrospun nanofibrous structures for tissue engineering. *Materials Today*, *16*(6), pp. 229–241. doi:10.1016/j.mattod.2013.06.005

Waqar, A., Abulibdeh, N. and Salam, A. (2019). Adsorption Studies of Textile Dye (Chrysoidine) from Aqueous Solutions Using Activated Sawdust. *International Journal of Chemical Engineering*, 2019, p. 8 pages. doi: https://doi.org/10.1155/2019/9728156.

Wen, H., Chen, Y., Yu, d., Li, X., Zhang, D. (2016). Electrospun zein nanoribbons for treatment of lead-contained wastewater. *Chemical Engineering Journal,* Elsevier B.V., 290, pp. 263–272. doi: 10.1016/j.cej.2016.01.055.

Wernsdorfer, W., Allaga-Alcalde, N., Hendrison, D.N and Christou, G. (2002). Exchange-biased quantum tunnelling in a supramolecular dimer of single-molecule magnets. *Nature*, 416(6879), pp. 406–409. doi: 10.1038/416406a.

Xu, W., Karst, D., Yang, W. and Yang, Y. (2008). Novel zein-based electrospun fibres with the water stability and strength necessary for various applications. *Polymer International.*, 57, pp. 1110–1117. doi: 10.1002/pi.

Yabuuchi, N. and Komaba, S. (2014). Recent research progress on iron- and manganese-based positive electrode materials for rechargeable sodium batteries. *Science and Technology of Advanced Materials*. IOP Publishing, 15(4), pp. 1-29. doi: 10.1088/1468-6996/15/4/043501.

Yao, C., Li, X. and Song, T. (2006). Electrospinning and Crosslinking of Zein Nanofibre Mats. *Journal of Applied Polymer Science*, 103(1), pp. 380-385. doi: 10.1002/app.24619

Yin, J., & Deng, B. (2015). Polymer-matrix nanocomposite membranes for water treatment. *Journal of Membrane Science*, *479*, pp. 256–275. doi:10.1016/j.memsci.2014.11.019

Zdraveva, E., Fang, J., Mijovic, B., Lin, T., Rayleigh, Lord, & Morton, W. J. (2017). *Electrospun nanofibers*. doi:10.1016/B978-0-08-100550-7.00011-5

Zeugolis, D. I. , Ekaputra, A.K., Tong, Y. W., Yang, L.L, Hutmacher, D.W., Sheppard, C., Raghunath, M. (2008). Electro-spinning of pure collagen nano-fibres - Just an expensive way to make gelatin. *Biomaterials*, 29(15), pp. 2293–2305. doi: 10.1016/j.biomaterials.2008.02.009.

Zhang, C., Yuan, X., Wu, L., Han, Y. Sheng, J.(2005). Study on morphology of electrospun poly(vinyl alcohol) mats. *European Polymer Journal*, 41(3), pp. 423–432. doi: 10.1016/j.eurpolymj.2004.10.027.

Zhang, T , Tang, R. , Hao Qiu, C. W. (2014). Journal of Magnetism and Magnetic Materials Solvothermal synthesis and characterization of monodisperse superparamagnetic iron oxide nanoparticles. *Journal of Magnetism and Magnetic Materials*, *379*, pp. 1–6. doi:10.1016/j.jmmm.2014.12.054

Zhang, X., Tang, K., & Zheng, X. (2016). Electrospinning and Crosslinking of COL / PVA Nanofiber-microsphere Containing Salicylic Acid for Drug Delivery. *Journal of Bionic Engineering*, *13*(1), pp. 43–149. doi:10.1016/S1672-6529(14)60168-2

Zhang X , Tang K, Z. X. (2015). Electrospinning and Rheological Behavior of Poly (vinyl alcohol)/ Collagen Blended Solutions. *Journal of Wuhan University of Technology-Mater. Sci. Ed*, *30*(4), pp. 840–841. doi:10.1007/s11595-015-1239-x

Zhang Y, Wu B, Xu H, Liu H, Wang M, He Y, P. B. (2016). Nanomaterials-enabled water and wastewater treatment. *NanoImpact*, *3–4*, pp. 22–39. doi:10.1016/j.impact.2016.09.004

Zhao, L., Shi, L., Zhang, Z., Chen, J., Shi, D., Yang, J., & Tang, Z. (2011). *Preparation and Application of Chitosan Nanoparticles and Nanofibers*. *28*(03), pp. 353–362.

Zhong, S., Teo, W. E., Zhu, X., Beuerman, R., Ramakrishna, S., & Yung, L. Y. L. (2005). Formation of collagen-glycosaminoglycan blended nanofibrous scaffolds and their biological properties. *Biomacromolecules*, *6*(6), pp. 2998–3004. doi:10.1021/bm050318p

Zouni, A. (2001). Crystal structure of photosystem II from Synechoccus elongatus at 3.8[thinsp]A resolution. *Nature*, 409(1988), pp. 739–743.

Züger, F. (n.d.). Novel approach to use insoluble collagen type I for electrospinning of nanofibers and their characterization. University of Basel, *September 2017*.

CHAPTER 2

RESEARCH METHODOLOGY

2.1. Chemical Reagents

All materials and reagents were purchased from Sigma Aldrich. These are zein powder (Mw 900 00), rat tail collagen solution, calf skin collagen (250 mg), PVA (MW 89-98 000 degree of hydrolysis 99%), hexamethylenediamine (HMDA) (98%), ammonia solution (25 wt%), $KMnO_4$ (99.0%), acetic acid, (99.7%) ethanol (99.8%), hydrated iron (III) and chloride, hydrochloric acid (30-33%), sodium hydroxide (99%) and acetone (99%).

2.2. Experimental Procedures

2.2.1. Preparation of zein polymer fibres

The preparation of zein polymer fibres was following work by Sellingand Lin. Zein (20 wt%, 25 wt%, 30 wt%) were prepared and dissolved in ethanol solution (70 wt%). The solutions were stirred at 70°C for two hours. The solution were electrospun varying the following parameters applied voltage (15, 20, 25 kV) and the spinneret to collector distance (10 cm) respectively (Selling *et al.* 2007; Lin *et al.* 2012).

2.2.2. Preparation of collagen polymer fibres

The preparation of collagen polymer fibres was following the work by Aras & Kazanci. Collagen solutions were prepared (Table 3.1) and the solutions were stirred at room temperature for two hours. The solution were electrospun varying the following parameters applied voltage (15, 20, 25 kV) and the spinneret to collector distance (10 cm) respectively (Lin *et al.* 2012; Kazanci 2014).

Table 2.1: Different preparation conditions of collagen solutions

Preparation		Solvent
1	Collagen (10-20 wt %)	0.1 M acetic acid/ (80:20) PBS 20 x buffer and ethanol solution/ 10 mL of sodium acetate/acetic acid buffer solution
2	Rat tail collagen solution	Solvents
3	10 wt% and 16 wt% Collagen	1:1 ethanol: PBS buffer solution
4	300 mg Collagen	25% Glacial acetic acid/ 75% TFE
5	350 mg Collagen	10% Trifluroethanol (TFE)
6	100 mg Collagen	(93/7 %) Glacial acetic acid /DMSO
7	2 g Collagen	25% Glacial acetic acid/ 75% TFE

2.2.3. Preparation of zein/PVA polymer blended fibres.

The preparation of zein/PVA polymer blended fibres was following the work of Zhang. Zein/ PVA blend nanofibres were prepared by electrospinning technique. PVA (12 wt%) was dissolved in distilled water which was stirred at 90°C for 30 min then ethanol was added to the solution to form 70 (v/v) % ethanol solution and allowed to stir for another 30min. Then 25 wt% of zein was weighed and dissolved in 70 (v/v) % ethanol /PVA/distilled water solution and stirred for two hours. The zein/ PVA solutions were used to prepare weight (w/w) ratios set on (**Table 2.2**) and electrospun at distance of 10 cm.

Table 2.2: Illustration of the weight (w/w) ratios of zein/PVA polymer blended fibres

Zein	12 wt % PVA
90	10
80	20
70	30
60	40
50	50

2.2.4. Synthesis of iron oxide nanoparticles by hydrothermal process

Iron oxide nanoparticles were synthesised using two solutions following the work of Umar. $FeCl_3 \cdot 6H_2O$ (1.46 g) and hexamethylenediamine (HMDA) (1.04 g) was added in 100 ml deionized water under vigorous stirring for 30 min. The HMDA was a reducing agent that controlled the size of iron oxide nanoparticles. The pH of the resultant solutions was then maintained at pH 7 using $NH_3 \cdot H_2O$ and stirred for two hours. Ammonium solution was used to control the pH value of the solution as well as resource to supply hydroxyl ions to the

solution. After two hours the resultant solutions were loaded into a stainless-steel autoclave, sealed and heated at different of 110 °C and 140 °C, respectively for four hours. After completing the reaction in desired time, the autoclave was allowed to cool at room-temperature and finally a brownish orange product was obtained which was washed with deionized water, ethanol and acetone sequentially and dried at room-temperature.

2.2.5. Synthesis of manganese oxide nanoparticles by co-precipitation method

$KMnO_4$ (0.126 g) was dispersed in 95 ml of NH_4OH solution in a 100 ml beaker. The solution was stirred with a magnetic stirrer bar for 15 minutes to dissolve $KMnO_4$. The stirring was stopped and the solution was transferred into centrifuge tubes and stored at room temperature for 24 hours in the dark. The produced precipitate was washed using distilled H_2O for five intervals and separated by centrifugation at 6000 rpm for 5 minutes. The precipitate was crushed into fine particles and calcined at 600 °C and at 800 °C using the furnace.

2.2.6. Incorporation of Fe_2O_3 and Mn_2O_3 nanoparticles on zein/PVA fibre blends

The blended solutions were prepared by weighing 12 wt% PVA and dissolved in distilled water which was stirred at 90°C for 30 min then ethanol was added to the solution to form 70 (v/v) % ethanol solution and allowed to stir for another 30min. Then 25 wt% zein was weighed and dissolved in 70 (v/v) % ethanol /PVA/distilled water solution and stirred for two hours. Three different concentrations ranging from (4.25, 4.75 and 5.25 wt %) of iron oxide (Fe_2O_3) and manganese oxide (Mn_2O_3) nanoparticles were separately added directly to the prepared solutions. The combined solution was stirred for 24 hours on a magnetic stirrer until the solution was homogeneous and ready for electrospinning.

2.3. Characterization techniques

2.3.1. Scanning electron microscopy (SEM)

The FE-SEM (Leo, Zesis) scanning electron microscopy operated at 1.00 keV electron potential was used to study the surface morphologies of the polymer fibres, polymer fibre blends and nanocomposite fibres, the samples were placed on the sample holders coated with a carbon tape and dried at room temperature.

2.3.2. Transmission electron microscopy (TEM)

Transition electron microscopy A JEOL JEM-2100 transmission electron microscope operating at 200 kV was used to obtain the size and shape of the synthesized iron oxide and manganese oxide nanoparticles.

2.3.3. Fourier transform infrared spectroscopy (FT-IR)

The chemical structures and chemical composition of polymer fibres, polymer fibre blends, nanoparticles and nanocomposite fibres were studied using Thermo scientific Nicolet iS50-FTIR spectrometer, universal ATR with the diamond detector, with a wavelength range 4000 cm^{-1} to 400 cm^{-1} to determine the interaction between the polymers with each other and the nanoparticles.

2.3.4. X-Ray diffraction (XRD)

The X-ray diffraction patterns were recorded by a Bruker D2 diffractometer at 40 kV and 50 mA. A secondary graphite monochromated Co K alpha radiation (l = 1.7902 A˚) was used to confirm the crystallinity of the prepared nanoparticles and the electrospun polymer fibres, polymer fibre blends and nanocomposite fibres as well as determining the size of the nanoparticles, and the measurements were taken at high angle 2θ in a range of 5˚–90˚ with a scan speed of 0.01° 2θ s^{-1}.

2.3.4. Ultraviolet Visible spectroscopy (UV-Vis)

Optical properties (most of which are in the ultraviolet, or visible range) of a material are determined by its interaction with electromagnetic (EM) radiation. The electromagnetic radiation compromises of transmission, absorption, emission, refection, refraction, diffraction, or scattering effects (Ghobadi, 2013; Zanatta, 2019). These optical properties are related to the characteristics of the electronic bands of the semiconductors or ultimately to their atomic structure and chemical bonding (Jubu *et al.*, 2020). The Tauc method is applicable only to materials in which a localization of energy states can be assumed–such as in amorphous materials and nanoparticles.Therefore it is vital to study the electronic band interaction of the prepared polymeric nanomaterials. The UV-Vis spectroscopy is the simplest, common and the cheapest most preferred method for bandgap determination. The band gap of the polymeric nanomaterials was determined using the Tauc method. The optical properties of polymer fibres, polymer fibre blends, nanoparticles and nanocomposite fibres were studied using Thermo

scientific Evolution 220 UV visible spectrophotometer which collects spectra in the wavelength range of 1100-190 nm using a spectral bandwidth of 1 nm (variable slit) to determine the absorption spectra of the prepared polymer fibre blends as well as the nanoparticles before and after incorporation into the polymer fibres.

2.3.5. Photoluminescence spectroscopy (PL)

Photoluminescence analysis was performed at room temperature using Jasco Spectrofluorimeter FP-8600 equipped with XE lamp at 150 W. The bandwidth excitation slit was at 5 nm, and the emission was used in the range of 200-1010 nm to measure the fluorescence behaviour of the manganese oxide and iron oxide nanoparticles before and after incorporation into the polymer fibres

2.3.6. Thermal gravimetric analyser (TGA)

The thermal stability of electrospun polymer fibres, polymer fibre blends, nanoparticles and nanocomposite fibres was studied using a PerkinElmer STA 600 Simultaneous Thermal Analyzer (Waltham, USA). The analysis was accomplished under a nitrogen atmosphere, 3.2 bar pressure, 20 mL/min flow rate and at a heating rate of 10°C/min starting from 30 °C to 900 °C.

2.4. Adsorption of chrysoidine dye

A stock solution (1000 ppm) was prepared by dissolving 1g of chrysoidine G in a 1000 mL of deionized water. Working solutions of contact time (15-120 min), different pH (2-12), initial concentration (20-100 mg/L) and adsorbent dosage (2- 18 mg) were prepared in batch mode and duplicate. All experiments were conducted on a CPXH Ultrasonic bath from Branson (USA) and the adsorbate was separated from the adsorbent by centrifugation. Since all the adsorption batch experiments were of similar design therefore the effect of pH will serve as an example to illustrate a typical experimental setup. For the effect of pH, a pH range was selected from pH 2 to pH 12. In a series of 100 mL glass bottles 2 mg of adsorbent was added, then 20 mL of 100 mg/L adsorbate was introduced to the adsorbent in a 100 mL glass bottle and the pH was adjusted either with 0.1 M HCl or 0.1 M NaOH. The mixture was placed in the ultrasonic bath for 120 min at room temperature, the adsorbate was separated from the adsorbent by centrifugation. Thereafter adsorption studies were analysed using UV-Vis spectrophotometer at a λ_{max} of 399 nm.

The equations used for removal efficiency and adsorption capacity are shown below

Percentage Removal

$$\% \text{ Removal} = \frac{(C_o - C_e)}{C_o} \text{ X } 100 \qquad \textbf{eq. (1)}$$

Where C_o is the initial concentration of chrysoidine G in solution (mg/L) and C_e is the equilibrium concentration (mg/L).

Adsorption Capacity

$$q_e = \frac{(C_o - C_e)V}{M} \qquad \textbf{eq. (2)}$$

Where C_o is the initial concentration of chrysoidine G in solution (mg/L), C_e is the equilibrium concentration (mg/L), qe is the equilibrium adsorption capability (mg/g), m is the mass of adsorbent (g), and V is the volume of solution (L).

Statistical Error Analysis

Error analysis was also established to compare the validity of kinetic and isotherm models using the following relation:

$$SSE = \sum_{i=1}^{N} \left(q_{ecal} - q_{exp} \right)^2 \qquad \textbf{eq. (3)}$$

where q_{cal} and q_{exp} are the calculated and experimental adsorption capacities of adsorbent nanofibres, respectively.

2.5. Adsorption Isotherms and Kinetic studies

The equilibrium performance between zein/PVA nanofibre blends, α-Fe_20_3/zein/PVA and α-Mn_2O_3/zein/PVA nanocomposites adsorbents and the chrysoidine G has been illustrated by employing the two most commonly used adsorption isotherms Langmuir and Freundlich (Purkait *et al*., 2010; Qureshi *et al.*, 2017) . Langmuir isotherm assumes that adsorption occurs on a monolayer coverage at a homogeneous surface (Tapadia & Sahin, 2015; Alagumuthu et al. 2012). The Langmuir isotherm can be expressed in a linear form as shown by in **Table 2.3**. Meanwhile Freundlich assumes that adsorption occurs at a heterogeneous surface through a

multilayer adsorption mechanism, and that the adsorbed amount increases with the concentration which can be expressed in a linear form as shown in **Equation 8** (Proctor &Toro-Vazquez, 2009; Al-Ghouti & Da'ana, 2020). In these equations, C_e and Q_e are the solute concentration (mg/L) and the adsorbed dosage. The Langmuir constants, KL, represent the monolayer adsorption capacity of the solute. For the Freundlich, K_f and n are the constants related to the adsorption capacity intensity, which for a good adsorbent, 1<n<10 (Fierro *et al*., 2008).

Table 2.3: Linear form of Langmuir isotherm equations (Chowdhury *et al.*, 2011; Sahin & Tapadia, 2015)

Isotherm	Linear form	Plot	Equation no.
Langmuir 1	$\frac{C_e}{q_e} = \frac{1}{KL\, q_m} + \frac{C_e}{q_m}$	$\frac{C_e}{q_e}\ vs\ C_e$	**eq. (4)**
Langmuir 2	$\frac{1}{q_e} = (\frac{1}{KL\, q_m})\frac{1}{C_e} + \frac{1}{q_m}$	$\frac{1}{q_e}\ vs\ \frac{1}{C_e}$	**eq. (5)**
Langmuir 3	$q_e = q_m - (\frac{1}{K_L})(\frac{q_e}{C_e})$	$q_e\ vs\ \frac{q_e}{c_e}$	**eq. (6)**
Langmuir 4	$\frac{q_e}{C_e} = K_L\, q_m - K_L q_e$	$\frac{q_e}{C_e}\ vs\ q_e$	**eq. (7)**

Freundlich isotherm

$$q_e = k_{f.} C_e^{\frac{1}{n}} \qquad \textbf{eq. (8)}$$

Kinetic modelling allows estimation of sorption rates and also leads to suitable rate expressions characteristic of possible reaction mechanisms. Pseudo first order kinetic model is used to describe the kinetics of liquid-solid phase adsorption systems which was established by Lagergren 1898. Pseudo second order kinetics describes systems in which adsorption/desorption process in relation to surface reaction that controls the overall adsorption process, this model was first proposed by Blanchard et al., 1984. Adsorption kinetics for both

the first and the second order were conducted to assess both the rate of chrysoidine G sorption and the equilibrium time required to obtain the sorption isotherm.

Pseudo first order:

$$Ln\,(q_e - q_t) = Lnq_e - k_1 t \qquad \textbf{eq. (9)}$$

Pseudo second order:

$$\frac{1}{q_e} = \frac{1}{K_2 q_e^2} + \frac{1}{q_e} t \qquad \textbf{eq. (10)}$$

Where qt (mg/g) is the amount of chrysoidine G adsorbed at time t (min); qe (mg/g) is the amount of chrysoidine adsorbed at equilibrium, k_1 (1/min) is the first order adsorption rate constant and k_2 (g/mg min) is the second order adsorption rate constant.

2.6. References

Al-Ghouti, M. A., & Da'ana, D. A. (2020). Guidelines for the use and interpretation of adsorption isotherm models: A review. *Journal of Hazardous Materials*, *393*, pp. 122383. doi:10.1016/j.jhazmat.2020.122383

Blanchard, G., Maunaye, M. and Martin, G. (1984). Removal of heavy metals from waters by means of natural zeolites. *Water Research,* 18(12), pp. 1501–1507.

Chowdhury, S., Misra, R., Kushwaha, P., & Das, P. (2011). Optimum sorption isotherm by linear and nonlinear methods for safranin onto alkali-treated rice husk. *Bioremediation Journal*, *15*(2), pp. 77–89. doi:10.1080/10889868.2011.570282

Fierro, V., Torne´-Ferna´ndez, V., , D. Montane´, A. C. (2008). Adsorption of phenol onto activated carbons having different textural and surface properties. *Microporous and Mesoporous Materials*, 111, pp. 276–284. doi: 10.1016/j.micromeso.2007.08.002.

Ghobadi, N. (2013). Band gap determination using absorption spectrum fitting procedure. *International Nano Letters*, *3*(2), pp. 2–5.

Jubu, P. R., Yam, F. K., Igba, V. M., & Beh, K. P. (2020). Tauc plot scale and extrapolation effect on bandgap estimation from UV – vis – NIR data – A case study of β -Ga_2O_3. *Journal of Solid State Chemistry*, *290*, pp. 121576. doi:10.1016/j.jssc.2020.121576

Kazanci, M. (2014). Solvent and temperature effects on folding of electrospun collagen nanofibers. *Materials Letters*. Elsevier, 130, pp. 223–226. doi: 10.1016/j.matlet.2014.05.114.

Lagergren S (1898). Zur Theorie der sogenannten Adsorption Geloester Stoffe. *Veternskapsakad Handl*, 24, pp. 1–39

Lin, J., Li, C., Zhao, YI., Hu , J., and Zhange, Li. (2012). Co-electrospun Nanofibrous Membranes of Collagen and Zein for Wound Healing. *ACS Appl. Mater. Interfaces*, 4, pp. 1050-1057. doi.org/10.1021/am201669z

Proctor, A., & Toro-Vazquez, J. F. (2009). The Freundlich Isotherm in Studying Adsorption in Oil Processing. In *Bleaching and Purifying Fats and Oils: Theory and Practice* , 2, pp. 201-219 7. doi:10.1016/B978-1-893997-91-2.50016-X

Purkait, M. K., Gusain, D. S., DasGupta, S., & De, S. (2004b). Adsorption behavior of chrysoidine dye on activated charcoal and its regeneration characteristics by using different surfactants. *Separation Science and Technology*, *39*(10), pp. 2419–2440. doi:10.1081/SS-120039347

Qureshi, U. A., Khatri, Z., Ahmed, F., Khatri,M. and Kim, I. (2017). Electrospun Zein Nano fibre as a Green and Recyclable Adsorbent for the Removal of Reactive Black 5 from the Aqueous Phase. *ACS Sustainable Chem. Eng.*, 5, pp. 4340-4351. doi: 10.1021/acssuschemeng.7b00402.

Sahin, R., & Tapadia, K. (2015). Comparison of linear and non-linear models for the adsorption of fluoride onto geo-material: Limonite. *Water Science and Technology*, *72*(12), pp. 2262–2269. doi:10.2166/wst.2015.449

Selling, G. W., Biswas, A., Patel, A., Walls, D.J., Dunlap, C., Wei, Y. (2007). Impact of Solvent on Electrospinning of Zein and Analysis of Resulting Fibres. *Macromolecular Chemistry and Physics*, 208, pp. 1002–1010. doi: 10.1002/macp.200700056

Zanatta, A. R. (2019). Revisiting the optical bandgap of semiconductors and the proposal of a unified methodology to its determination. *Scientific Reports*, *9*(1), pp. 11225. doi:10.1038/s41598-019-47670-y

Zhang, M, Liu Y., Yi., H., Luan, J., Zhang, Y., Cai, H., and Sun, D. (2014). Electrospun zein / PVA fibrous mats as three- dimensional surface for embryonic stem cell culture. *The Journal of The Textile Institute*, 105(3), pp. 246–255. doi: 10.1080/00405000.2013.835902.

CHAPTER 3

RESULTS AND DISCUSSION

Preview: This project focused on the fabrication of zein, collagen polymer fibres, zein/PVA fibre blends and their incorporation of iron and manganese oxide nanoparticles. All materials prepared were characterized by FTIR, UV Visible spectroscopy, PL spectroscopy, XRD, TGA, SEM and TEM for the metal oxide nanoparticles. It was difficult to electrospin collagen fibres as compared to zein polymer fibres and zein/PVA fibre blends incorporated with the metal oxide nanoparticles were optimised. Hence, no data is presented for the collagen aspect of the study as planned in the objectives. The incorporated polymer fibres blends were tested for the adsorption of the chrysoidine G dye. The adsorption was followed using the effect of contact time, pH, initial concentration and adsorbent dosage. The regeneration studies were conducted to evaluate the effectiveness of the adsorbent material from the economic and environmental point of view. Chapter 3 discussion is focused on the optical, structural changes or interactions, morphological features of zein polymer fibres, their blends and incorporation of iron and manganese oxide nanoparticles into the polymer fibre blends using UV Visible spectroscopy, PL spectroscopy, SEM , TEM for metal oxide nanoparticles, XRD and TGA.

3.1. Electrospun zein nanofibres

3.1.1. Effect of concentration on zein nanofibres.

Zein consists of several peptides of different molecular weight, solubility, charge and α-zein is the major fraction (85% of total zein) of these peptides, it is soluble in 50–95% alcohol solutions (Wang et al., 2005). However, a water-ethanol mixture has been shown to be the best solvent for zein (Parris & Dickey, 2001; Lawton, 2002; Guo et al., 2005; Kim et al., 2006). There are various parameters that have an influence in fibre formation and fibre morphology such as solution, processing and ambient parameters. Solution concentration plays a vital role in nanofibre diameter, hence at low viscosities the surface tension has an influence on the fibre morphology which may result in beads or fibres with beads. At higher concentration the production of fibres are hindered by the inability to control and maintain the flow of a polymer solution to the tip of the needle (Deitzel et al., 2001). The distance to the collector also has an effect on fibre production therefore minimum distance should be kept to allow the fibres

sufficient time to dry before reaching the collector in order to prevent beads from occurring (Buchkoa et al., 1999). In addition polymers with higher molecular weight results in higher viscosity and continuous uniform fibre formation. Electrospinning of zein above 20 wt% produces continuous fibre formation with less clogging at the tip of the collector. **Fig. 3-1** (a), (b), (c) and (d) show SEM images and average fibre distribution of the zein fibres electrospun at different concentrations of 20 wt%, 25 wt% and 30 wt% with a voltage of 15 kV and a distance of 10 cm. The results obtained illustrated no bead formation on the morphology of the fibres and during electrospinning the yellow zein solution changed from yellow colour to white zein nanofibre-based structures. At 20 wt% uniform ribbon like fibres were obtained with an average diameter of 478 ± 0.75 nm and as the concentration was increased to 25 wt% the morphology of the fibres became thicker and had an amorphous ribbon shape with an increase in fibre diameter to 819 ± 0.95 nm. Further increase of the concentration to 30 wt% the fibres became thicker and were tubular shaped with an average fibre diameter of 992 ± 1.04 nm. It was observed that as concentration was increased there was a gradual increase in the fibre diameter which had an influence in the morphology of the fibres. There was less clogging observed during electrospinning of 25 wt% and continuous uniform fibre formation compared to 20 wt% and 30 wt% zein solutions. Miyoshi et al. (2005) studied the preparation of ultrafine fibrous zein membranes via electrospinning. It was reported that ultrafine fibrous zein membranes were successfully produced by electrospinning zein/ethanol solutions above 21 wt% with an electric field of 15 kV. Therefore the results obtained in study with correlation to concentration effect on fibre morphology were similar to the study conducted.

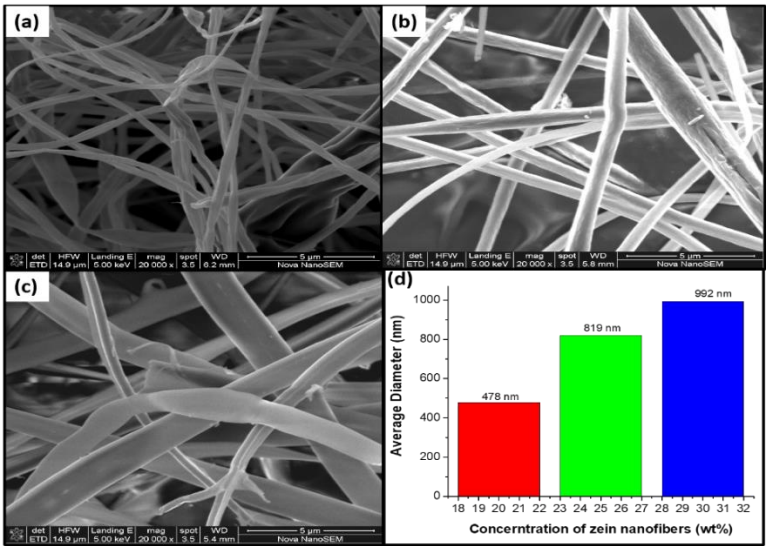

Fig. 3-1. SEM images and average fibre distribution of zein nanofibres at different zein concentration solutions (a) 20 wt%, (b) 25 wt%, (c) 30 wt% and (d) fibre size distribution.

3.1.2. Effect of applied voltage on zein nanofibres

Electrospinning occurs when the applied voltage is higher than the surface energy of a droplet of a polymer solution. Generally higher voltage causes greater stretching of the jet due to the increase in columbic force exerted by the charges and also increasing the voltage can lead to the reduction of fibre diameters due to increased stretching of the jet. Jacobs et al., (2011) and some researchers reported that applied voltage is one of the most important parameters in the electrospinning process due to its direct influence on the dynamics of the polymer solution flow. The changes in the applied voltage are reflected on the shape of the droplet suspending at the tip of the needle, its surface charge, velocity of the flowing polymer solution, and hence on the structural morphology of electrospun fibres. The SEM images of **Fig. 3-2** shows 25 wt% zein fibre size distribution at different voltages and illustrates that the increment in applied voltage has direct influence on fibre morphology. At 15 kV the morphology of the fibres had a tubular shape with an average diameter of 819 ± 0.95 nm and as the voltage was increased to 20 kV the average diameter of the fibres decreased to 699 ± 0.77 nm and the fibres became more interconnected, rougher and amorphous still maintaining the ribbon like shape. It was further observed that as the voltage increased to 25 kV the fibre morphology became more interconnected, thinner and had an average diameter of 625 ± 0.26 nm. Therefore the increment in voltage results in reduction of fibre diameter and also the rapid evaporation of ethanol solvent from the fibres enhanced uniform fibre production. Therefore 25 kV was regarded as the optimum voltage for polymer fibre fabrication because smooth interconnected fibres were produced at this voltage.

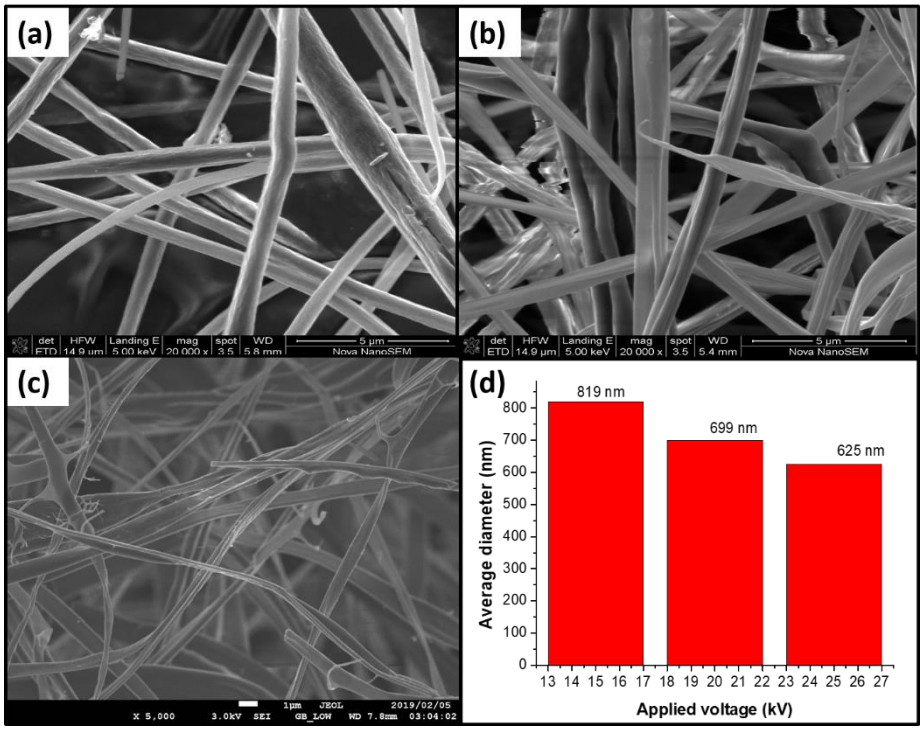

Fig. 3-2 SEM images and size distribution of 25 wt% zein nanofibres at different voltages (a) 15kV, (b) 20kV and (c) 25kV

3.1.3. XRD analysis of the zein polymer nanofibres

XRD was used for phase identification of zein crystallinity and the crystallinity index was calculated to denote the crystalline constituents of the amorphous regions of zein nanofibres. The XRD patterns in **Fig. 3-3** showed low intensity diffraction peak of zein nanofibres around 2θ value of 12.6º (110), 15.82 º (111), 18.74º (200) and 27.56 º (220), which were related to the average backbone distance within the α-helix structure of zein. The results indicated that the electrospun zein nanofibres retained its structural conformation (Senna *et al*., 2010). The three maximum peak were observed at 2θ value of 15.82 º (111), 18.74º (200) and 27.56 º (220). Oliveira *et al.* (2014) reported similar diffraction patterns with three broad peaks having maxima at 2θ = 14 º, 17 º and 25 º for electrospun zein/tannin bio-nanofibres. Miao & Yang, (2017) studied Poly(L-lysine) modified zein nanofibrous membranes as efficient scaffold for adhesion, proliferation, and differentiation of neural stem cells and reported the XRD of two diffraction peaks of 2θ =9.2º and 19.4º which are related to the α-helix and β-sheet structures of protein. Yao et al., (2006) reported that the difference between literature and experimental XRD parameters can be attributed to variations in the secondary and tertiary zein structure with the different solvents used during electrospinning process therefore ethanol and the medium

molecular weight of zein powder used in our study might have had an influence in the results obtained which was corresponding to other research studies, hence the crystallinity structure and orientation of zein polymer fibres was strongly influenced by the characteristics of the polymer in particular (molecular weight, tacticity, glass transition temperature etc.).

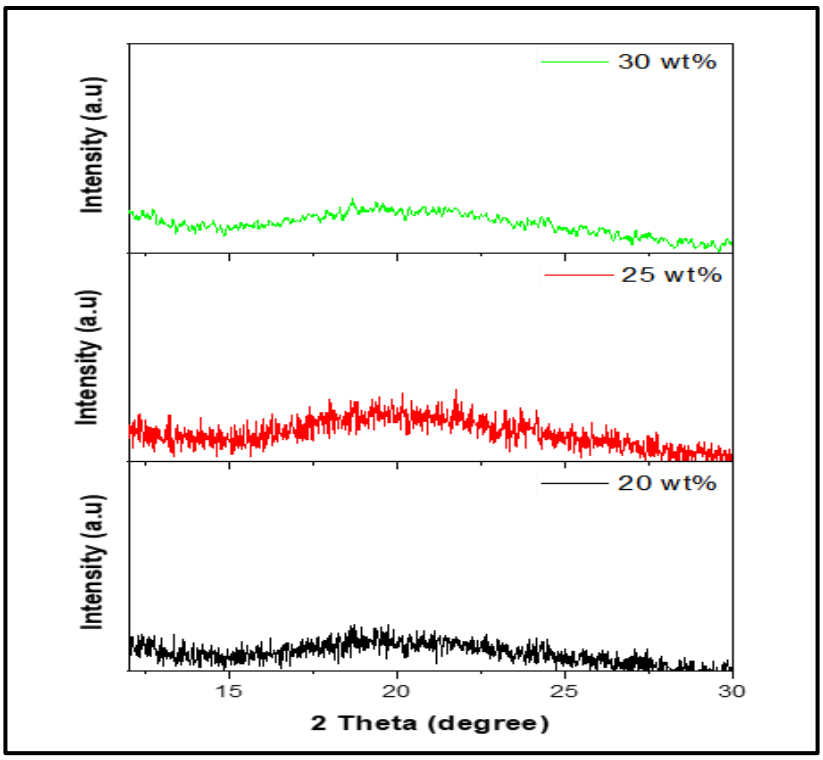

Fig. 3-3 XRD patterns of different concentrations of zein solutions (a) 20 wt %, (b) 25 wt% and (c) 30 wt%.

3.1.4. FTIR spectral analysis of zein nanofibres.

Zein proteins are classified according to their solubility and sequence homology into α, β, γ and δ zein. Zein is a highly hydrophobic protein as a consequence of apolar amino acids and it is also rich in α and β sequence homology which are soluble in alcohol solution. The β sheet are generally visible with a display of a shoulder peak around the region of 1620 cm^{-1}. **Fig. 3-4** show the FTIR of electrospun zein nanofibres that were fabricated at different concentration of 20 wt%, 25 wt% and 30 wt%. The zein nanofibres had a broad peak at 3294 cm^{-1} that is associated with amide I (due to NH_2 stretch vibrations). In addition the peak observed at 1660 cm^{-1} was due to the carbonyl stretching vibration. The carbonyl stretching vibration peak indicated that a high content of α–helices was present due to the absence of a secondary peak around 1620 cm^{-1}. At 1522 cm^{-1} a peak of amide II was observed which was

related to the NH bending. A peak of C-H bending was observed at 1437 cm^{-1} and further a peak at 1239 cm^{-1} was observed corresponding to the amide III (axial deformation vibration of the carbon-nitrogen stretching). Qureshi *et al.*, (2017) studied electrospun zein nanofibre as green and recyclable adsorbents. Qureshi and co-workers reported similar FTIR peaks of zein functional groups illustrating that there were no β–sheets present (1662, 1614 and 1631 cm^{-1}) therefore the results obtained indicates the predominate peaks of α-helices of zein nanofibres.

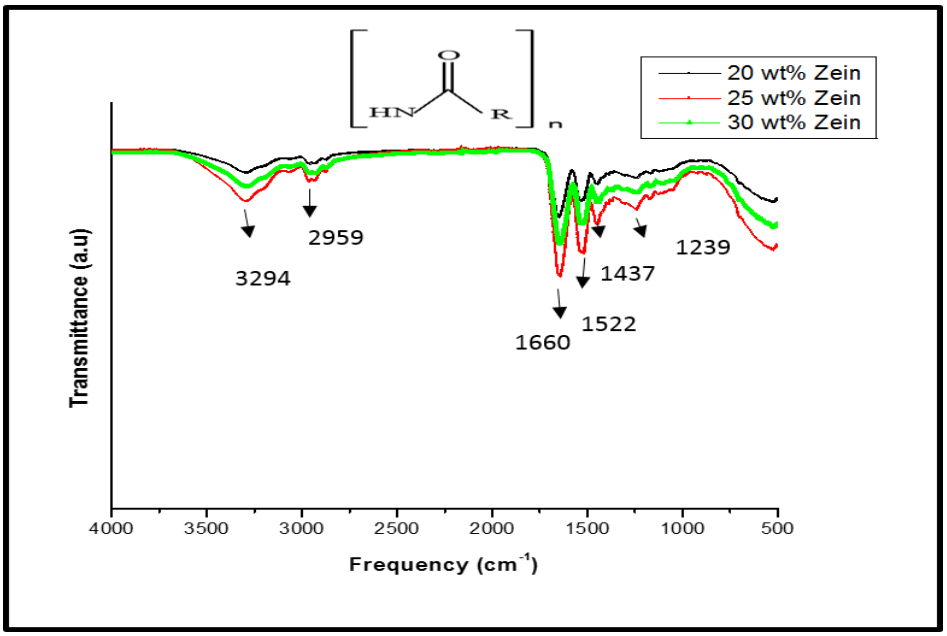

Fig. 3-4 FTIR spectra of zein nanofibres (a) 20 wt %,(c) 25 wt% and (d) 30 wt%.

3.1.5. Thermogravimetric analysis (TGA) of zein nanofibres.

The TGA results on **Fig. 3-5** show different electrospun zein nanofibre concentration 20 wt%, 25 wt% and 30 wt%. TGA results of 20 wt% and 25 wt% concentrations overlap each other. The zein nanofibres of 30 wt% was slightly below the 100 weight percent loss that might have been affected by the loading capacity during TGA analysis. The results obtained illustrated that the zein nanofibres (20 wt% and 25 wt%) had a weight loss of 2.29% below 100℃ which was associated with water loss. A major weight loss was of 66.93% was observed between 254.94℃ to 382.49 ℃, this was attributed by decomposition of amino and carbonyl groups of zein nanofibres. Another weight loss of 13.33% was observed between 258.94℃ to 382.49℃ was observed and it was attributed by complete degradation temperature of zein residues. At this particular major loss regime it was observed that the mass loss was negative. This was

attributed by instrumental error. The zein nanofibres (30 wt%) had a minor weight loss of 2.64% below 100℃. A major weight loss of 65.46% was observed around 245.89℃ to 357.49℃ this was attributed by the decomposition of the amino and carbonyl groups present in zein nanofibres. Another weight loss of 19.03% was observed around 357.49℃ to 575.54℃. At this particular regime there was a negative mass loss which was related to instrumental error. The negative mass losses due to instrumental error for all zein nanofibres could be associated to the following: (1) deteriorated TGA sensor that affected sensitivity after sample run, (2) error associated with baseline correction, (3) the crucible contained an adsorbed sample on the inner surface or uncleaned solvent before the run that resulted in the negative loss value (Olatunji et al., 2018). The TGA results deviated in negative mass losses but correlated in temperature regime losses with other research studies. Therefore results reported illustrated that there was less water present in the nanofibres, hence the decomposition regime temperatures observed correlated to other research studies previously reported in the literature of zein nanofibres (Torres-Giner et al., 2008; Kruger et al., 2009; Kayaci et al., 2013).

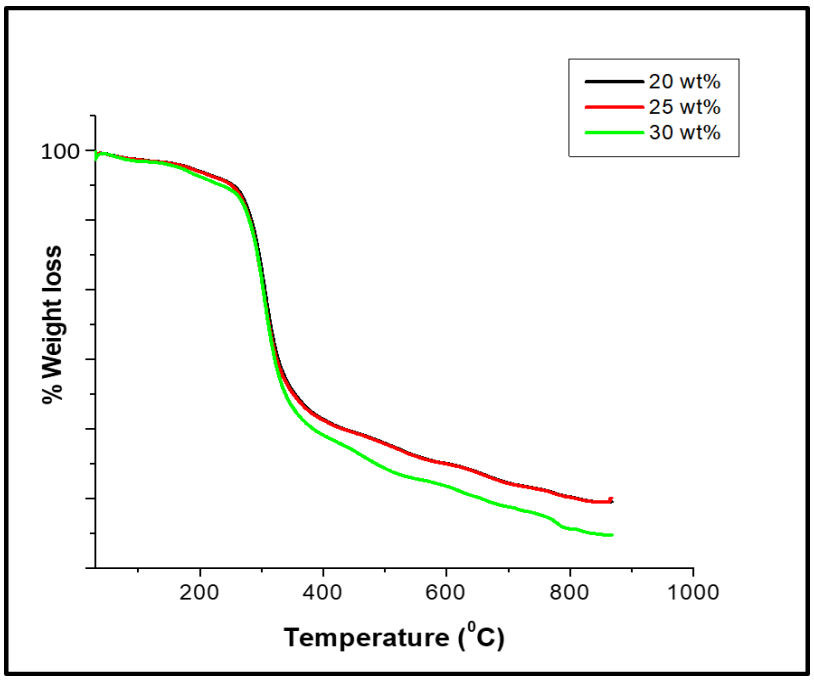

Fig. 3-5 TGA curve of zein nanofibres electrospun at 25 kV and distance: 10 cm

3.2. Optimization of collagen nanofibres.

3.2.1. Effect of concentration and applied voltage

Matthews *et al.* (2002) studied and reported that 0.8 w/v of type I collagen (calfskin) was readily soluble in HFIP. However, at this concentration the collagen did not exhibit any evidence of electrospinning and, regardless of the applied voltage; the polymer solution formed droplets and leaked from the syringe tip. Increasing the concentration of collagen 10-fold to 8.3 w/v resulted in a cloudy suspension and the formation of fibres during electrospinning. In this study the 20 w/v calfskin collagen was dissolved in 0.1M acetic acid, the solution was cloudy; it was dripping at the tip of the pasteur pipette hence resulted in electrospraying regardless of the applied voltage which was 15 kV to 25 kV. This illustrated that the molecular weight of collagen might have had an influence in the electrospraying. Then another optimisation preparation method was implemented by dissolving 10, 16 and 20 w/v calfskin collagen into 10 mL sodium acetate/ acetic acid buffer solution, the solution was cloudy and resulted in electrospraying. The obtained results from collagen preparations illustrated that the prepared concentrations are low for electrospinning process and more collagen is needed for preparations.

A 250 mg of collagen sample is insufficient for electrospinning preparations and the choice of solvent might have had an influence in electrospraying instead of electrospinning. Gopinath et al. (2014) conducted a study on the effect of aqueous ethanol on the triple helical structure of collagen and reported that the kinetic stability of the collagen triple helix in the presence of trifluroethanol was found to depend both on temperature and on the concentration of ethanol; higher temperatures accelerate the denaturation process whereas prolonged exposure at low temperature has no effect. Therefore a further method of a 10 wt % and 16 wt % rat tail collagen solution was prepared in 1:1 ethanol: PBS buffer solution. The solution was cloudy but still electrosprayed. The use of ethanol instead of trifluroethanol might have had an influence on the electrospraying, hence other research studies previously conducted (Torres-Giner et al., 2008; Khanum et al.2015) made extensive use of trifluroethanol (TFE) and 1, 1, 1, 3, 3, 3-hexafluoro-2-propanol (HFIP) as the choice of solvent for electrospinning collagen (Dong *et al.*, 2009). Further preparations of rat tail collagen solution was conducted and **Table 3.1** illustrate the findings of the different optimisation preparations and it indicated that electrospinning of collagen was unsuccessful due to the small quantity of the sample. The

prepared collagen solutions electrosprayed that suggested the molecular weight of collagen proportional to the polymer chain length was less entangled in the solvent solutions, therefore more collagen was required for potentially successful optimisation of the polymer. The above observation correlates with some findings obtained by Kazanci (2014). The production of collagen nanofibres on academic research or a larger scale production will be a disadvantage because collagen is expensive and a large quantity of the sample is essential hence all initiated optimization preparations for electrospinning process in our study was unsuccessful and though revealing the practical difficulties relating to industrial application. Therefore optimisation of collagen/PVA could not be implemented because optimisation of collagen alone had been unsuccessful.

Table 3.1: Findings of collagen optimisation preparations.

Preparation	**Solvent**	**Findings**
300 mg Collagen	25% Glacial acetic acid/ 75% TFE	Did not electrospun
350 mg Collagen	10% Trifluroethanol (TFE)	Electrosprayed beads only
100 mg Collagen	(93/7 %) Glacial acetic acid /DMSO	White jelly appearance no fibres formed just electrosprayed beads
2 g Collagen	25% Glacial acetic acid/ 75% TFE	Electrosprayed beads

3.3. Fabrication of zein/PVA polymer fibre blends

3.3.1. Effect of solution concentration of zein/PVA polymer fibre blends

In recent years blending polymers has been an alternative way of creating new polymers with well-established physiochemical properties. Zhang *et al.* (2014) conducted a study on electrospun zein/PVA fibrous mats as three-dimensional surface for embryonic stem cell culture and it was reported that morphology of the nanofibre blends improved through the compatibility of PVA that improved the hydrophilic performance of zein through hydrogen bonding and gradual increment of PVA concentration. Hence, the embryonic stem cells cultured on chosen electrospun zein/PVA mats in vitro proved that culture products were easily attached onto the mat and the mat could be used for induction of stem cell differentiation. **Fig. 3-6** of SEM images shows the concentration of the random electrospun zein/PVA weight ratio under the same processing condition (voltage, 25 kV and TCD 10 cm). The results illustrated

that the morphology of **Fig. 3-6** (a) had ribbon like shape this was due to high concentration of zein in the blend solution. **Fig. 3-6** (b) results showed that the fibre morphology improved and became well defined tubular like shape, although the average diameter gradually increased from 603 ± 0.34 nm to 725 ± 0.40 nm due to the increment of PVA concentration in the solution. The increment of PVA concentration resulted in a higher charge density on the surface of the ejected jet solution during electrospinning, therefore, more electric charges were carried by the electrospinning jet. As the charges carried by the jet increased, fibres were drawn faster to the collector and there was not enough time for rapid evaporation of the ethanol solvent. Therefore, the diameter of the final fibres also became substantially larger (Ghelich *et al*., 2015). The morphology of electrospun zein fibres alone in section **3.1.1** are observed to be ribbon-like, therefore addition of PVA content had a great effect on the large average diameter which illustrate that PVA improved the mechanical strength of zein.

Fig. 3-6 (c) and (d) showed that the morphology improved from tubular shape to being more interconnected as the PVA concentration gradually increased. The average fibre diameter significantly decreased from 636 ± 0.37 nm to 400 ± 0.32 nm. **Fig. 3-6** (e) showed that there was no change in the shape of the fibres but there was an increase in the average diameter to 470 nm this might be due to the fact that at high concentration the formation of continuous fibres were prohibited because of the inability to maintain the flow of the solution at the tip of the needle resulting in the formation of larger fibres (Deitzel *et al.*, 2001) compared to **Fig. 3-6** (d). Therefore, solution concentration has a significant effect on the average diameter of the polymer fibre blends hence varying solution concentration altered the morphology of the nanofibre blends formed.

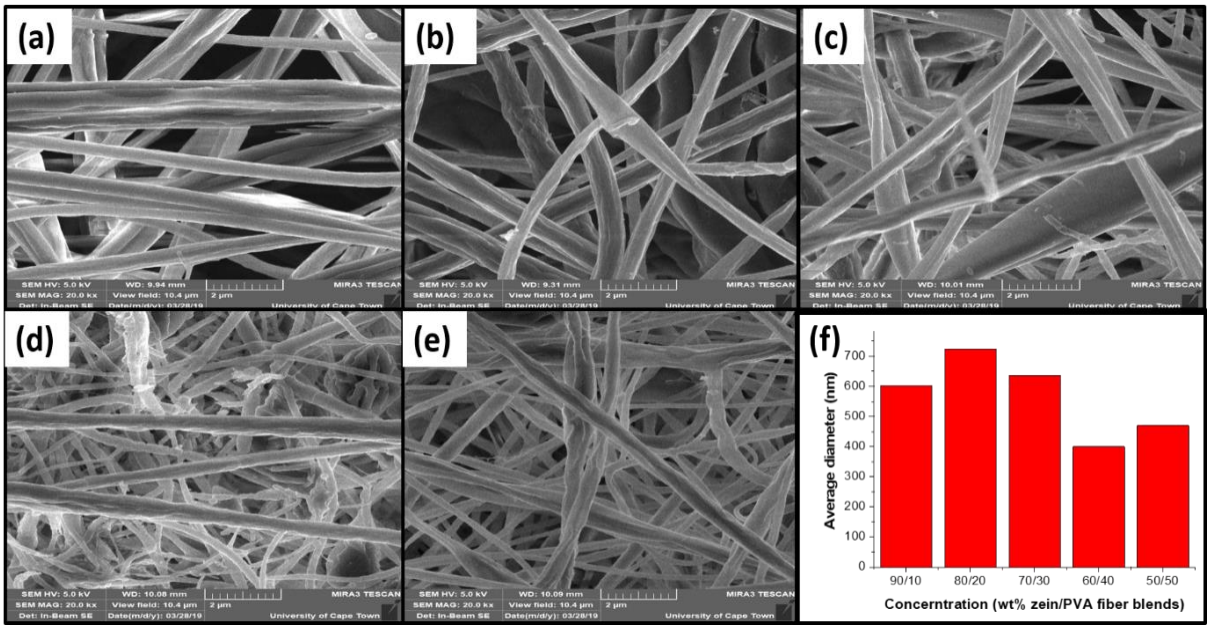

Fig. 3-6 Average diameter of the electrospun zein/PVA fibre blends prepared at different weight ratios (a) 90/10, (b) 80/20, (c) 70/30, (d) 60/40 and (e) 50/50 with voltage of 25 kV and distance of 10 cm.

3.3.2. Effect of applied voltage of zein/PVA polymer fibre blends

Applied voltage has an effect on the stretching and acceleration of the jet solution from the tip of needle to the collector, which has influence on the morphology of the fibres obtained. The SEM images in **Fig. 3-7** shows the fibre size distribution of 80/20 wt% zein/PVA fibre blend at different voltages. At 25 kV the fibre formation was ribbon like and interconnected with a fibre diameter of 725 ± 0.40 nm, as the voltage further increased to 27 kV the fibre morphology became tubular shaped with an average diameter of 758 ± 0.39 nm. The voltage was further increased to 30 kV it was observed that the morphology of the fibres were floppy, thinner, flatten and interconnected with an average diameter of 848 ± 0.37 nm. The observation of increase in voltage resulted in higher average fibre diameter this maybe attributed by the instability of the jet causing an increase in fibre density due to increasing voltage (Jacobs et al., 2010; More *et al.*, 2015). Some researchers have reported that the higher electric fields results in the acceleration and stretching of the jet due to the larger coulombic forces. The high electric field therefore promotes faster solvent evaporation to yield drier fibres. It has been shown that higher applied voltage results in the ejection of more fluid in a jet, leading to larger fibre diameters (Ramakrishna et al., 2005; Garg *et al.*, 2014). From the results obtained in this study 25 kV was considered the optimum voltage for electrospinning zein/PVA fibre blends due to

its well defined ribbon like solid shape with smaller average diameter compared to 27 kV and 30 kV of zein/PVA fibre blends.

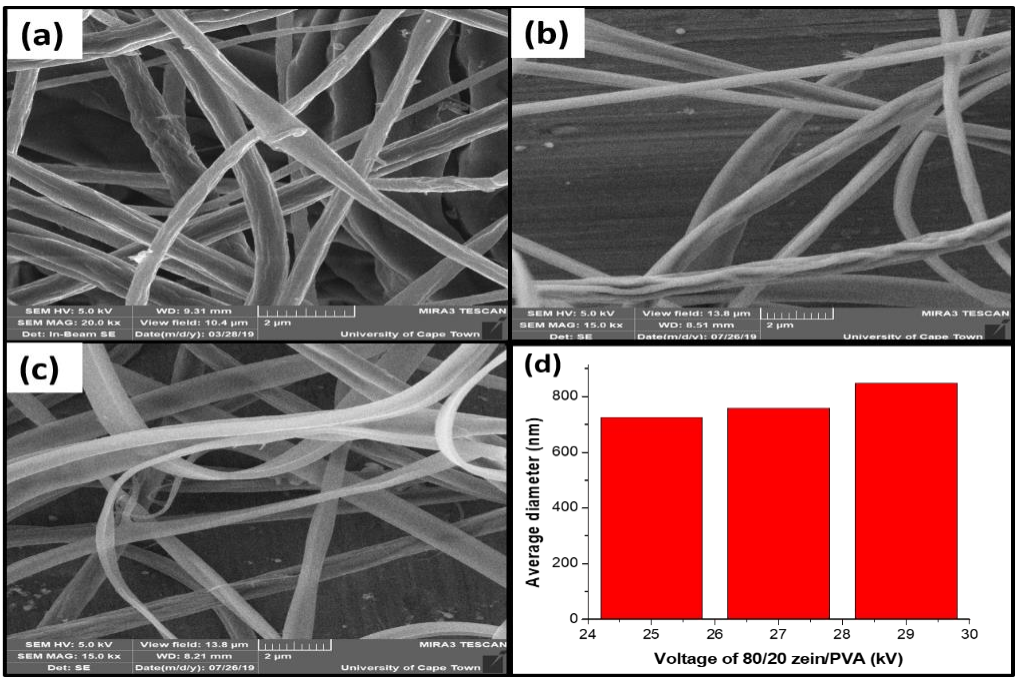

Fig. 3-7 Average diameter of zein/PVA fibre blend weight ratio of 80/20 at different voltages (a) 25 kV, (b) 27 kV and (c) 30 kV with distance of 10 cm.

3.3.3. Optical properties of zein/PVA blends.

Ultraviolet visible spectroscopy has been widely used in many applications, including extraction monitoring, polymer impregnation in the analysis of polymers, polymers fibre blends and monitoring the miscibility/immiscibility of polymer fibre blends .One of the controversial topics amongst researchers is the compatibility of polymer mixture system and it has been found to be closely related to the extent of polymer-polymer interaction therefore solid evidence has indicated that blends from polymers are not fully miscible due to weak interactions at the molecular level, on condition of the fraction of a certain composition and/or the preparation processing (Kun and Pukánszky, 2017). Zhang *et al.*, (2014) reported on the successful fabrication of zein/PVA fibrous mats as three dimensional surface for embryonic stem cell using electrospinning technique. The addition of PVA improved the hydrophobic properties of zein, mechanical strength and elongation of the membranes. In this study zein/PVA blend solutions were prepared from different weight blend ratios of 90/10, 80/20, 70/30, 60/40 and 50/50 in 70 wt% ethanol solution. **Fig. 3-8** (a) displayed peaks at 316 nm (90/10), 312 nm (80/20), 315 nm (70/30), 319 nm (60/40) and 324 nm (50/50) for the different blend ratios. This might be due to the assigned n→p* transitions in carbonyl groups of

carboxamide present in zein .Zein alone does not absorb radiation above 330 nm due to the polar ethanol solvent chosen and the carboxamide group present in zein. Hence the displayed peaks suggest that the polymers were immiscible. The carbonyl band is well pronounced on all fibre blends which illustrated that the polymer fibre blends contained chromophoric groups (C=O, C-N, C-C).

The greatest absorption changes are observed as the concentration of PVA was increased. This suggested that the kinetics and efficiency of the chromophore formation depended on the sample composition. The absorption peaks for the blend weight ratios were blue shifted. It was also observed that zein/PVA (80/20) peak at 312 nm was more pronounced with a shoulder like, and the shoulder like peak was less pronounce for the other fibre blend weight ratios. This may be caused by the two polymers being partially miscible at this particular blend weight ratio suggesting that there was change in the conformation of zein/PVA (80/20) fibre blend (Senna *et al*., 2010; Abdelghany *et al*., 2015). Tauc plot of the zein/PVA blend solutions **Fig. 3-8** (b) revealed band edges and band gap energies at 365 nm (3.39 eV), 411 nm (3.01 eV), 379 nm (3.27 eV), 382 nm (3.24 eV) and 373 nm (3.32 eV) respectively for the different blend weight ratios. It was observed that the band energy of 80/20 zein/PVA fibre blend had lower band energy and the highest band edge compared to other blend weight ratios. The lack of polar groups in zein prevents intermolecular interaction in zein/PVA fibre blends, leading to immiscibility and partial miscibility of the polymer fibre blends (Deshpande et al., 2013). Therefore as the concentration of PVA increased there was increase in the wavelength due to the increase in the conjugation length of the polymer chains.

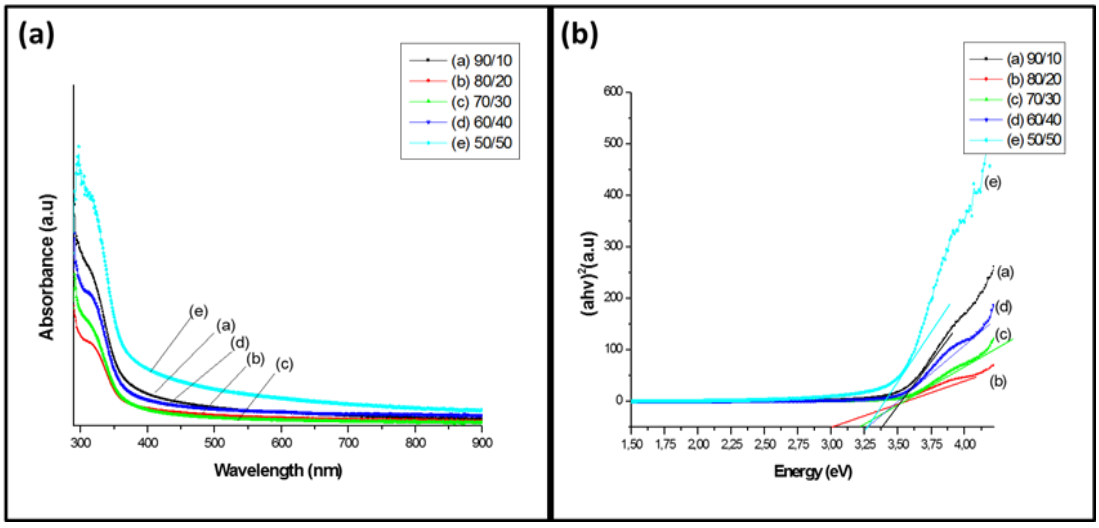

Fig. 3.8 (a) UV spectrum of zein/PVA nanofibre blends, and (b) Tauc plot for direct transitions.

3.3.4. XRD patterns of zein/PVA polymer fibre blends

The XRD patterns and crystallinity planes for zein/PVA blends **Fig. 3-9** showed peaks of the zein/PVA blends at $2\theta = 12.6^{o}$ (110) , 15.86^{o} (111) and 27.62° (220) and a broad amorphous peak for zein/PVA nanofibres at $2\theta = 18.78^{o}$ (200) for 90/10, 70/30, 60/40 and 50/50 blend weigh ratios. This illustrated that the two polymers at the specified zein/PVA fibre blends were immiscible. The intensity of these peaks did not show any change by addition of PVA concentration, displaying that the α-helix and β-sheet structures of zein were not distorted (Miao & Yang, 2017). There was no broad dominate peak observed for 80/20 blend weight ratio instead there was a stronger intermolecular hydrogen bonding interaction between zein and PVA due to the polar part of zein functional groups that attracted the polar groups of PVA (hydroxyl residues) (Senna *et al*., 2010; Aziz *et al*., 2017). The zein/PVA (80/20) blend ratio showed a decrease in intensity of the dominate peak at $2\theta = 18.70^{o}$ and a decrease of the peak at $2\theta = 15.78^{o}$, this evidently concludes that zein/PVA blends were influenced by the increment of PVA in the 80/20 blend ratio which ultimately favoured complete miscibility between the polymer composite which was influenced by the formation of intermolecular hydrogen bonding higher than intramolecular hydrogen bonding (Senna *et al*., 2010; Jiang *et al*., 2012). Senna et al. (2010) conducted a study on improving the compatibility of zein/poly (vinyl alcohol) blends by gamma irradiation and graft copolymerization of acrylic acid and reported similar XRD results for zein/PVA blend weight ratio. Therefore the results obtained corresponds to other research studies previously reported.

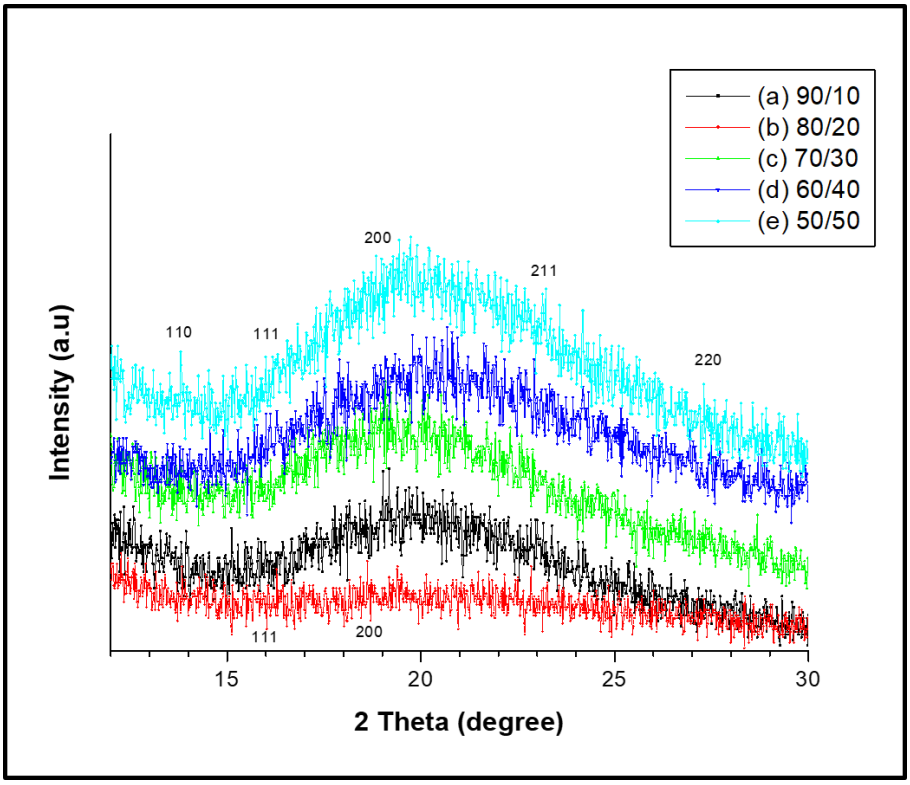

Fig. 3-9 XRD patterns of different weight ratio of zein/PVA fibre blends (a) 90/10, (b) 80/20, (c) 70/30, (d) 60/40 and (e) 50/50.

3.3.5. FTIR Spectra of zein/PVA polymer fibre blends

In the spectra of the electrospun zein/PVA blend weight ratios, the peak appeared at 3289 cm^{-1} (O–H stretching and N–H stretching), 2958 cm^{-1} (alkyl stretching), 1645 cm^{-1} (C-O stretching) the carbonyl peak remained unchanged this suggested that the C=O functional group did not participate in the intermolecular interactions. It should be taken into account that some functional groups from both polymers are involved in creating hydrogen bonds, whereas some of them remain unbound dependently on chain conformations and steric hindrances, the peaks which appeared at 1528 cm^{-1} were of amide II (N-H bending), and 1447 cm^{-1} (C–H bending) and 1239 cm^{-1} (C-N stretching). The peaks of electrospun mats indicated that chemical bonds in this sample were limited. The intensity of the characteristic bands of all zein/ PVA nanofibre blends decreased. In particular, the intensity and width of the O–H stretching vibration peak was also decreased as compared to pure PVA (Koysuren et al., 2012; Tillekeratne & Easteal, 2000). Zein/PVA (80/20) blend weight ratio had lower frequency compared to other blend weight ratios, this could be due to stronger hydrogen bonding level between the various groups formed (Senna et al., 2010), therefore the FTIR spectral analysis

proved the presence of PVA in the electrospun zein/PVA fibre blend weight ratio and that the two polymers were highly immiscible despite the amount of sample composition added some functional groups still did not participate in intermolecular interactions, hence the compatibility of the two polymers was induced via hydrogen bonding stabilization.

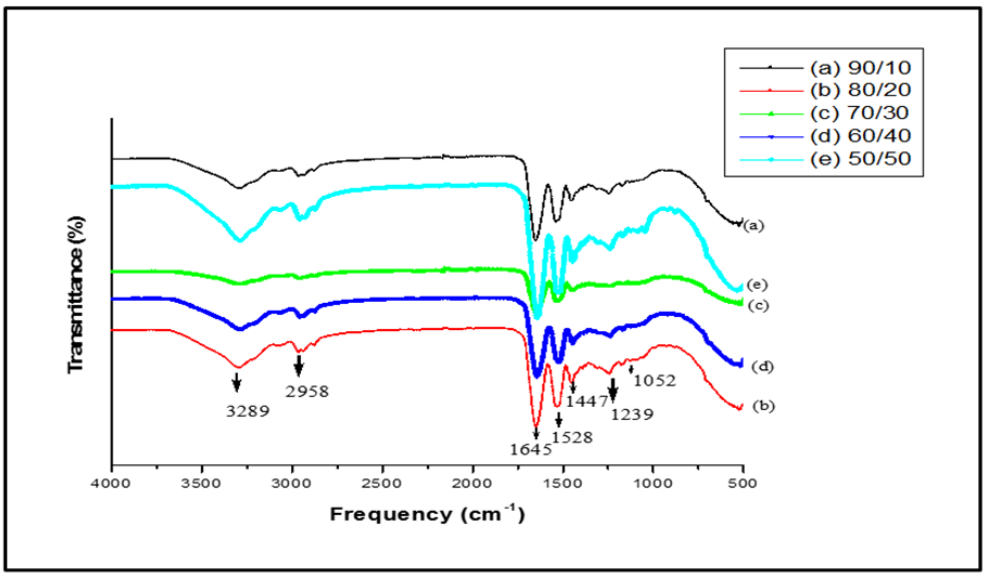

Fig. 3-10 FTIR spectra of zein/PVA nanofibre blends with different weight ratios (25 kV and distance: 10 cm).

3.3.6. Thermogravimetric Analysis (TGA) of zein/PVA polymer fibre blends

According to previous reported literature (Torres-Giner et al., 2008; Kruger et al., 2009) and results obtained from our current study it has been revealed that zein nanofibre thermal degradation occurs as two step decomposition stages around ~254℃ to 357℃ due to minor carbonyl and amino groups and a major loss was observed around ~357℃ to 578℃ which was due to remaining zein residues. Gilman et al. (1995) and other researchers in previous studies have revealed that PVA thermal degradation occurs in two step decomposition around 300 to 325℃ and 400 to 425℃. **Fig. 3-11** shows three decomposition stages for all different zein/PVA blend weight ratios . The first decomposition stages of zein/PVA fibre blends were due to water loss. The second decomposition stages were associated with the hydroxyl groups associated with PVA and amino functional groups of zein. The third decomposition stages were due to the remaining residues of zein/PVA (carbonyl, amino and methyl groups). **Fig. 3-11** (a) showed the first decomposition stage at (a) 5.95 % from 83.10℃ to 114℃. The second decomposition

stage was observed from 248.06℃ to 478.08℃ with 58.76% weight loss. The corresponding the DTA thermograms was obtained at 248.06℃. The third decomposition stage was observed from 478.08℃ to 565.5℃ with 30.10% weight loss. The corresponding DTA curve was obtained at 519.23℃. **Fig. 3-11**(b) the thermograms showed the first decomposition stage of 3.12% weight loss from 52.03℃ to 115℃. The second decomposition stage was observed from 254.46℃ to 4456.63℃. The corresponding DTA curve was obtained at 310.20℃. **Fig. 3-11** (c) showed first decomposition stage of 8.17% from 42.80℃ to 108.71℃. The second decomposition stage was observed from 266.89℃ to 400.97℃ with 48.12% weight loss. The third decomposition stage was observed from 400.97℃ to 559.34℃ with 38.58% weight loss. The corresponding DTA curve was observed at 522.81℃. **Fig. 3-11** (d) showed first decomposition stage of 5.01% from 44.31℃ to 100.24℃. The second decomposition stage was observed from 261.06℃ to 358.60℃ with 43.56%. The corresponding DTA curve was obtained at 307.38℃. The third decomposition stage was observed from 358.60℃ to 550.87℃ with 46.33%. The corresponding DTA curve was observed at 519.23℃. **Fig. 3-11** (e) showed first decomposition stage of 5.48% from 42.99℃ to 94.21℃. The second decomposition stage was observed from 252.39℃ to 388.92℃ with a weight loss of 53.10%. The corresponding DTA curve was obtained at 313.41℃. The third decomposition stage was observed from 388.92℃ to 549.55℃. The corresponding DTA curve was observed at 522.81℃.

It was observed that zein (80/20) blend weigh ratio decomposition stages occurred at a faster rate and the other blend weight ratio's decomposition stages were prolonged. Therefore this suggest that zein/PVA80/20) blend weight ratio was partially miscible and the other blend weight ratios were immiscible. The DTA results of the different zein/PVA fibre blends corresponds to the weight losses the thermograms. **Fig. 3-11** (a), (b) and (e) had the highest major decomposition stage of about 58.76% (90/10), 54.41% (80/20) and 53.10% (50/50) compared to other zein/PVA fibre blends. This observation illustrated that constant addition of PVA content had an impact in the compatibility of the two polymers. The blending of zein with hydrophilic polymer (PVA) could also reduce the glass transition of the resulting composite material (Senna et al., 2010). In this sense TGA results correlates with the SEM images **Fig. 3-6** which also showed that the morphology of zein/PVA improved with constant increment of PVA concentration in particular for zein/PVA (80/20) blend weight ratio. Therefore zein/PVA fibre blends are thermally stable.

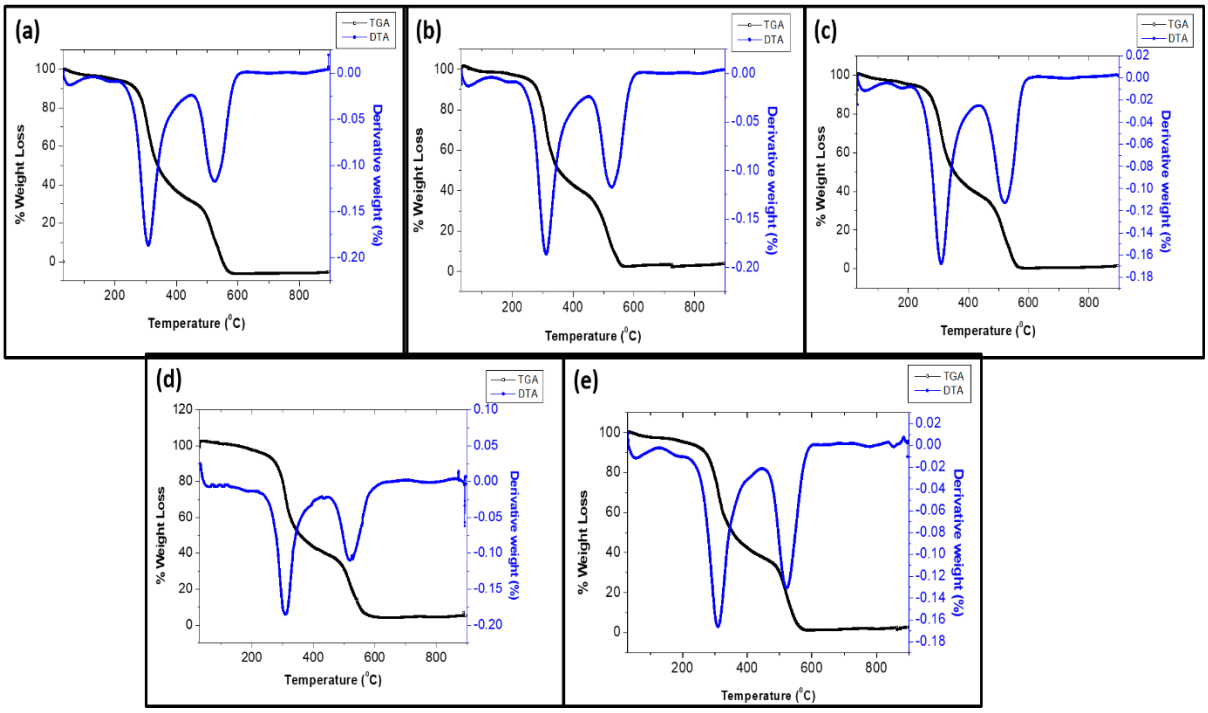

Fig. 3-11 TGA-DTA thermograms for different weight ratios of zein/PVA nanofibre blends (a) 90/10, (b) 80/20, (c) 70/30, (d) 60/40 and (c) 50/50 electrospun at 25 kV and distance: 10 cm.

3.4. Synthesis of Iron oxide (Fe_xO_y) nanoparticles

3.4.1. Effect of temperature on the preparation of iron oxide nanoparticles.

Capping agents can produce different morphologies, such as spheres and truncated hexagonal pyramid-shaped Fe_2O_3 nanocrystals. Wang et al. (2007) reported on the synthesis and magnetic properties of uniform hematite nanocubes using hydrothermal method. The results showed that hematite nanocubes could not be produced at lower temperatures below 100 ℃, as temperature increased the crystallinity of the nanocubes became well defined. Iron oxide nanoparticles were synthesized by hydrothermal method, the addition of HMDA worked as an addictive for controlling the shapes (aggregation) of the synthesized products. pH of the solution also plays a significant role in the size distribution and crystallinity of the nanoparticles therefore in this study the samples synthesized at pH 7 formed more stable aggregation state of the hematite nanoparticles (Demangeat *et al.*, 2018). It has been reported by other researchers that hematite formation using hydrothermal method is favored at high temperature or a neutral solution (Schwertmann *et al.*, 1999; Lin *et al.*, 2014). The particle size and size distribution of Fe_2O_3 nanoparticles were prepared at 110℃ and 140℃ as shown in **Fig. 3-12** (a) - (d). The shapes of the nanoparticles were not well defined nanocubes at 110℃ with particle size distribution of

20 to 80 nm. As the temperature was increased to 140℃ well defined nanocubes were produced with size distribution of 20-100 nm. This also indicates that increment in temperature has an influence on the crystallinity of hematite nanoparticles, due to faster nucleation than grain growth resulting in small particle size (~100 nm) which correlates to previous research studies (Denkbaş *et al.*, 2016)..

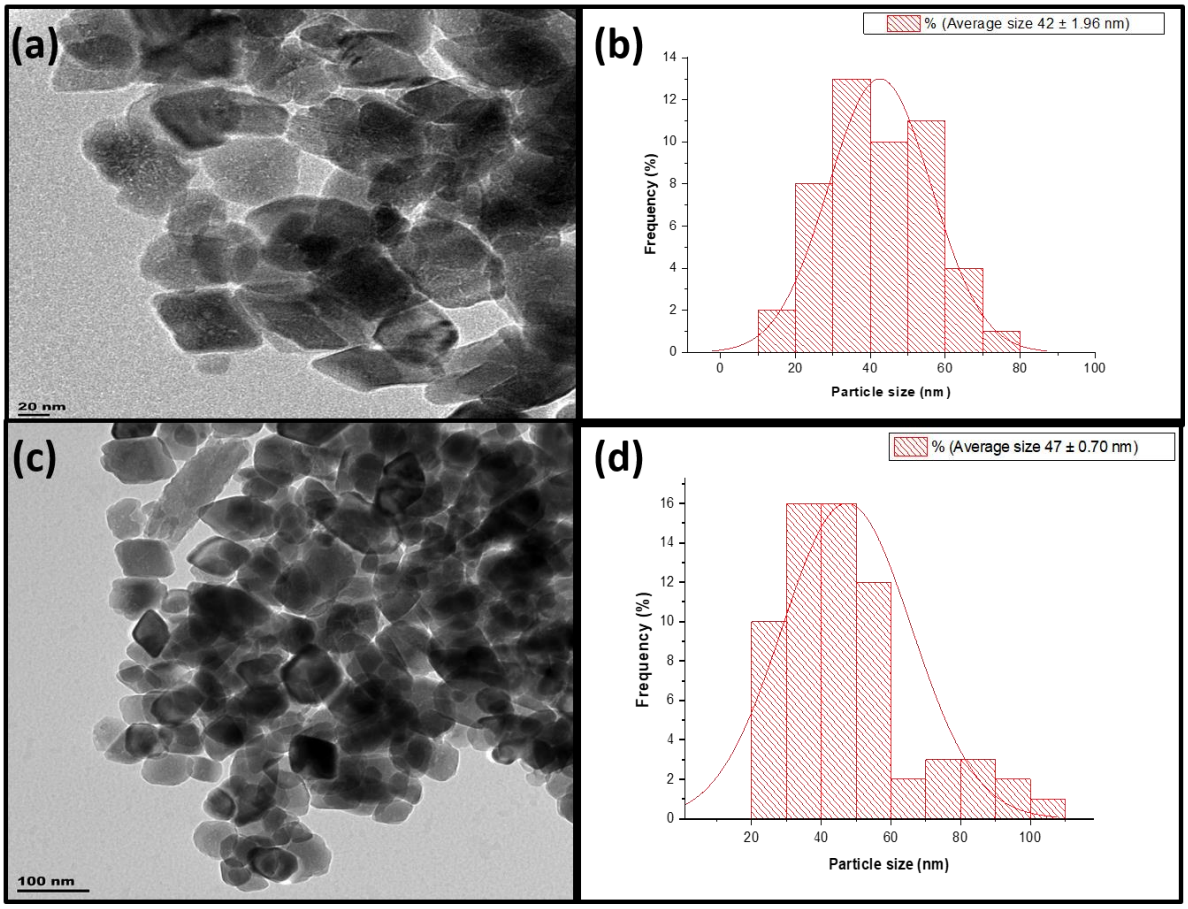

Fig. 3-12 TEM images and average size distribution of Fe_2O_3 nanoparticles prepared at different temperatures (a, b) 110℃ and (c, d) 140℃.

3.4.2. Optical properties of iron oxide nanoparticles

Iron oxide nanoparticles have been widely used as absorbents due to their broad region adsorption in ultraviolet region from electron transmission of Fe-O. The synthesized iron oxide nanoparticle optical properties were analysed using UV-visible spectroscopy and photoluminescence. A more detailed description of UV-visible spectroscopy and Tauc plot results can be obtained on **Appendix A**. **Fig. 3-13** (a) showed the photoluminescence of iron oxide nanoparticles had an excitation at 321 nm and 380 nm for α-Fe_2O_3 nanoparticles prepared at 110℃ and 140℃ and a peak was observed at 436 nm (2.20 eV) and 349 nm (2.25 eV). It

was observed that the PL intensity of α-Fe_2O_3 nanoparticles prepared at 110℃ decreased as the nanoparticles were larger compared to α-Fe_2O_3 nanoparticles prepared at 140℃ which was also confirmed by TEM image (**Fig. 3-12**). The photoluminescence results also displayed that as the temperature increased the maximum photoluminescence wavelength decreased accordingly (Gaob & Shenb, 1996) due to increase in particle size which was illustrated by the broad peak of α-Fe_2O_3 nanoparticles prepared at 140 ℃ and the emission intensity decreased with increasing excitation wavelength. Moloto *et al.* (2013) studied the optical properties of CdS on the reaction temperature and observed that temperature does have an effect the shapes of the nanoparticles due to the competition between the kinetic and thermodynamic growth regime, therefore in our study the effect of temperature displayed a critical role in the formation of the monodispersed α-Fe_2O_3 nanoparticles.

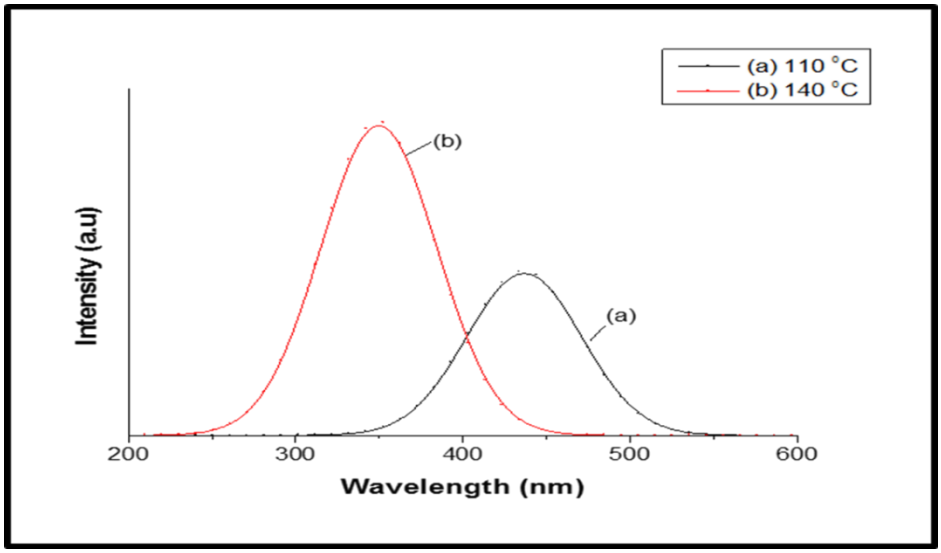

Fig. 3-13 (a) Photoluminescence spectra of Fe_2O_3 nanoparticles synthesized by hydrothermal process prepared at different temperatures (a) 110℃ and (b) 140℃.

3.4.3. XRD patterns of iron oxide nanoparticles.

The crystal structure of the nanoparticles was investigated by measuring the XRD. The patterns of α-Fe_2O_3 nanoparticles displayed peaks at 2θ degrees of 24.53, 33.37, 35.89, 41.25, 49.76, 54.18, 57.79, 62.69, 64.27 and 71.99º that are attributed to the (012), (104), (110), (113), (024), (116), (018), (214) and (300) crystalline planes of rhombohedral α-Fe_2O_3 structures (JCPDS 00-033-0664) . The average crystal size for 110 ˚C and 140 ˚C was estimated to be about 22.27 nm and 27.97 nm respectively. The peaks of α-Fe_2O_3 of 140℃ are more intense and narrower in comparison with the peaks of α-Fe_2O_3 at 110℃ indicating higher crystallinity due to faster nucleation. The mean size of α-Fe_2O_3 crystallites was calculated using the Scherrer equation:

$$COS\theta = \frac{K\lambda}{D} X \frac{1}{\beta_{hkl}}$$

where k = 0.99 is the shape factor λ is the x-ray wavelength ß is the full width at half maximum in radians and θ is the angle position of the maximum of diffraction peak. The XRD average crystalline size confirms the obtained TEM results of α-Fe_2O_3 nanoparticles which indicated that the particle size was improved with increasing temperature. This also suggest that the XRD intensities of the prepared α-Fe_2O_3 nanoparticles were different. The obtained results are similar to what was reported by Valášková et al. (2019) in α-Fe_2O_3 nanoparticles/vermiculite clay material, structural, optical and photocatalytic properties for α-Fe_2O_3 nanoparticles synthesized through chemical precipitation method at two different temperatures (500 ˚C and 700 ˚C).

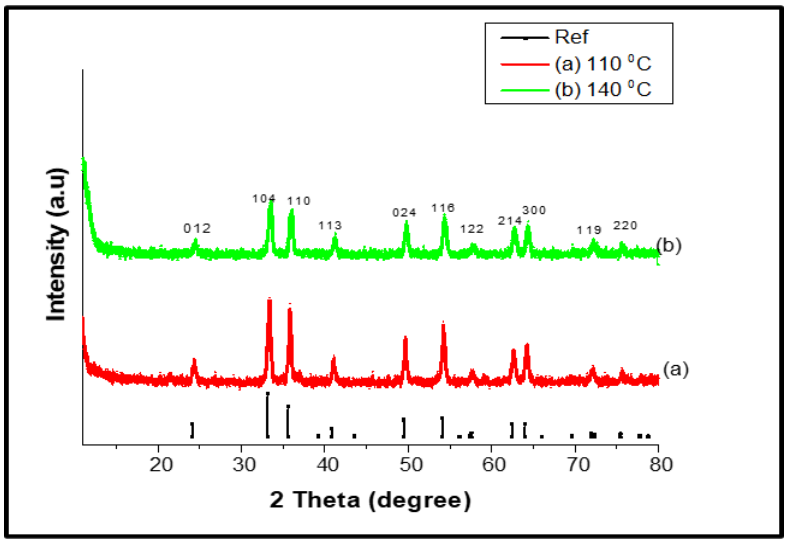

Fig. 3-14 XRD patterns of Fe_2O_3 nanoparticles prepared at different temperatures (a) 110℃ and (b) 140℃.

3.4.4. Thermogravimetric Analysis (TGA) of the prepared iron oxide nanoparticles

HMDA consist of unique properties that improves durability and mechanical strength of nanoparticles or nanocomposites for the construction of long-lasting antifouling nanoparticles or absorbent materials**.** According to literature HMDA monomer decomposition occurs around 230 to 480℃ (Zhang *et al.*, 2016). **Fig. 3-15** (a) and (b) depicts the thermal analyses (TGA, DTA) for synthesized hematite nanoparticles prepared at two different temperatures (110℃ and 140℃). As for α-Fe_2O_3 prepared at 110℃, there are five distinct weight loss steps in the

temperature ranges. α-Fe_2O_3 nanoparticles modified with HMDA showed a weight loss of approximately 2.33% from 64℃ to 100.85 ℃, which is attributed to the decomposition of HMDA physically adsorbed on the surface of α -Fe_2O_3 nanoparticles. The obvious weight loss at 284 to 489℃ is due to the decomposition of the modifier HMDA (methylene, amide groups) which chemically modified on the surface of α-Fe_2O_3 nanoparticles (Zhang *et al.*, 2016). The weight loss at 489 to 624℃ was due to further decomposition of HMDA of about 96.8% remains. At the temperature of 750 ℃ a residue of about 96.7% remains, possibly corresponding to the decomposition of α-Fe_2O_3. This indicated that the prepared surface-capped α-Fe_2O_3 nanoparticles contained about 3.38 per cent of surface-capping agent.

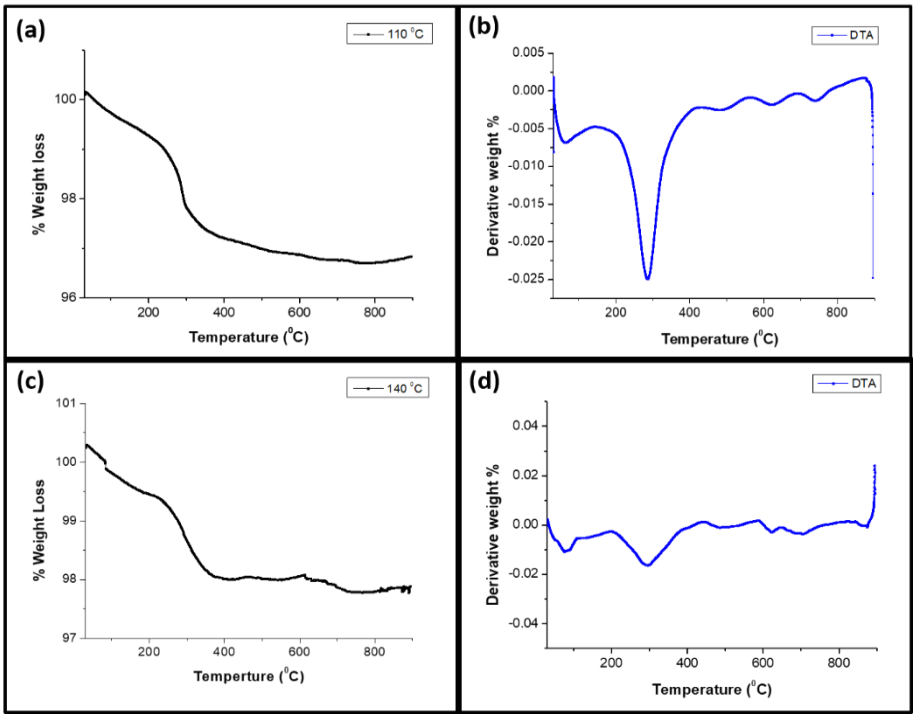

Fig. 3-15 TGA-DTA thermograms of α-Fe_2O_3 nanoparticles prepared at different temperatures (a-b) 110℃ and (c-d) 140℃.

The thermal analysis (DTA) studies that showed endotherms corresponding to the weight losses in TGA studies. **Fig. 3-15** (c) and (d) showed the thermal analysis (TGA, DTA) of α-Fe_2O_3 prepared at 140℃. There are 6 distinct weight loss steps in the temperature ranges. There was a weight loss of 2.2% for α-Fe_2O_3 nanoparticles from 85℃ to 98.82℃ due to water present. A major loss from 284℃ to 295℃ was due to the decomposition of HMDA. The weight loss from 295℃ to 500℃ was due to further removal of the chemically adsorbed water. Another weight loss at 500℃ to 705℃ was due to complete decomposition of HMDA on the surface of the iron oxide nanoparticles. The final residue weight loss at temperature of 880℃ was about

97.8% remains of α-Fe_2O_3 nanoparticles which decomposed to Fe_3O_4 respectively. DTA studies of α-Fe_2O_3 nanoparticles prepared at different temperatures confirmed endothermic peaks similar to those of TGA studies. This illustrated that there was no phase transition of synthesised nanoparticles instead temperature improved the morphology of the nanoparticles (Lassoued *et al.*, 2018). Darezereshki et al. (2011) studied the direct thermal decomposition synthesis and characterization of hematite (a-Fe_2O_3) nanoparticles and it was reported two endothermic peaks (88.61℃ and 232.6℃) and an exothermic peak (467.6℃) were found in the heating process due to transition of γ-Fe_2O_3 to α-Fe_2O_3, respectively. These results slightly deviate from our study hence we had no transition state of the prepared hematite nanoparticles instead there was decomposition of the capping agent which was HMDA. α-Fe_2O_3 nanoparticles calcined at 140℃ had greater thermal stability which was also influenced by the high crystallinity of the nanoparticles compared to α-Fe_2O_3 nanoparticles prepared at 110℃. Therefore iron oxide nanoparticles will be useful for incorporation with zein/PVA fibre blends in order to enhance the performance of the polymer fibre blends.

3.5. Synthesis of manganese oxide nanoparticles

3.5.1. Effect of temperature on the preparation of manganese oxide nanoparticles.

Manganese oxide can be found in diverse oxidation states such as MnO, MnO_2, Mn_2O_3, Mn_3O_4, and Mn_5O_8. These transition metal oxides have been previously investigated for their electronic, magnetic properties and applications for treatment of water. Manganese oxide nanoparticles were prepared in a single step precipitation method at room temperature without addition of any protective agent, respectively at pH 12 and were calcined at 600℃ and 800℃. **Fig. 3-16** shows the TEM images of manganese oxide nanoparticles prepared at different temperatures. The TEM image and particle size distribution for particles prepared at 600℃ as shown in **Fig. 3-16** (a) and (b) revealed that uniform monodispersed spherical shapes were formed with the particle size distribution of 100 to 300 nm as shown. **Fig. 3-16** (c) and (d) as the temperature was further increased to 800℃, the nanoparticle's shape changed from spherical to rod-spherical shapes with a decreased particles size. The particles were polydispersed and showed particle size distribution of sphere shapes and rod shapes in the range of 20 to 80 nm and 50 to 300 nm. At lower temperature of 600℃ the size of the nanoparticles was larger with conducive growth and as temperature increased from 600℃ to

800 ℃ there was a decline of the nanoparticle size and conducive nucleation occurred corresponding to previous studies (Fayaz *et al.*, 2010; Liu *et al.*, 2017). Therefore it is evident that temperature played a vital role in the formation of manganese oxide nanoparticles. In general, an increase in the temperature of calcination provides a high crystallinity hence manganese oxide nanoparticles were synthesised at higher temperatures. Although, according to literature low temperature and pH fastens the transformation of Mn oxidation state between various polymorphs (Portehault *et al*., 2009). In this study the manganese oxide nanoparticles transformation between polymorphs was successfully obtained at high temperature calcination temperature through co-precipitation method. This also concludes that high calcination temperature and pH also fastens the transformation of Mn oxidation states, produced high purity and yield of manganese oxide nanoparticles.

Manganese oxide nanoparticles were synthesised at higher temperatures compared to iron oxide nanoparticles because co-precipitation method at high calcination temperature was independent of longer aging time. In the case of iron oxide nanoparticles prepared via hydrothermal method the longer aging time favoured greater coalescence, allowing time to control the nanoparticle growth at lower temperature. The longer aging time of iron oxide nanoparticles had an effect on the smaller nanoparticle and crystallite sizes compared to manganese oxide nanoparticles. **Fig. 3-12 and Fig. 3-16** reveals that the different nanoparticle methods utilized to synthesize iron oxide nanoparticles and manganese oxide illustrated that a stable pH contributed to the aggregation of nanoparticles and temperature also had an effect on the morphology and particle sizes of the metal oxide nanoparticles.

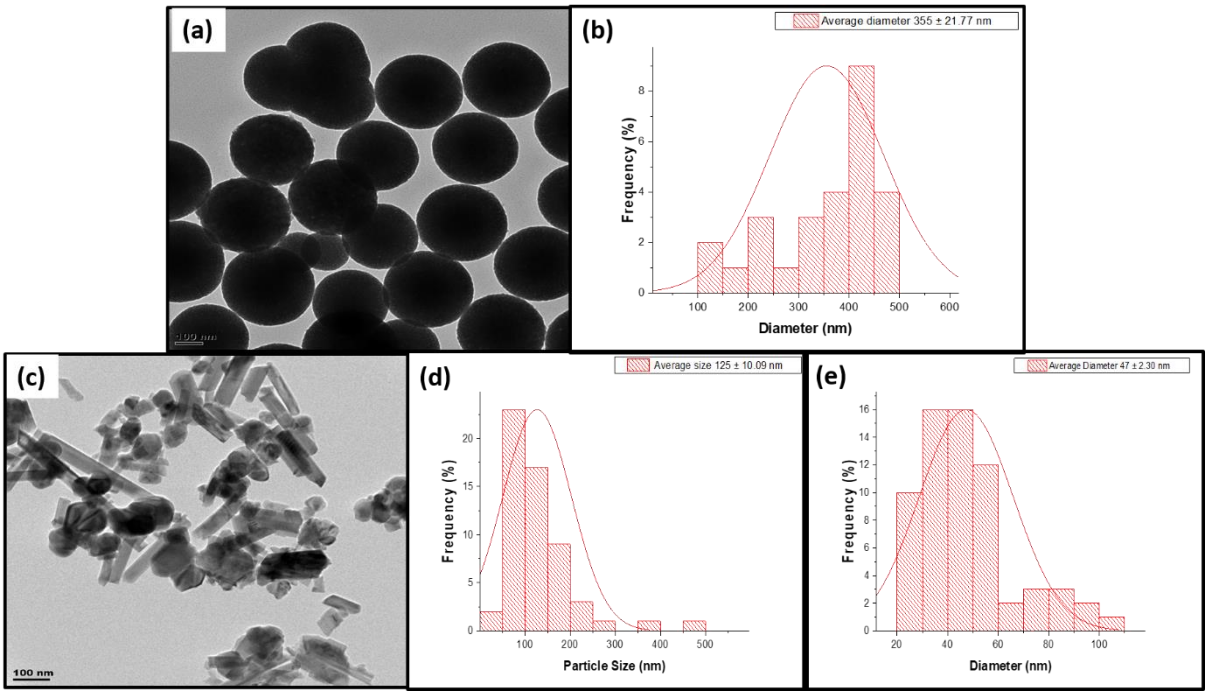

Fig. 3-16 TEM images and size distribution of manganese oxide nanoparticles prepared at different temperatures (a, b) 600℃ and (c, d, e) 800℃.

3.5.2. XRD Spectra of the prepared manganese oxide nanoparticles

The crystal structure of the monodisperse K-OMS-2/ Mn_2O_3 which contains potassium ions in the tunnels (K-OMS-2/Mn_2O_3) octahedral molecular sieve (OMS) nanoparticles was investigated by measuring the XRD. The MnO_2 nanoparticles calcined at 600℃ displayed a prominent peak at 36 º and not any other clear peak was displayed therefore it clearly indicates the nanospheres are amorphous (Maliyekkal et al., 2010). At increased calcination temperature of 800℃ more dominate sharp peaks displayed which illustrates that there was a change in crystalline size and the crystalline pattern correspond to the cryptomelane phase, characteristic of the OMS-2 (JCPDS No. 29-1020), as shown in **Fig. 3-17** (a) Additional peaks corresponding to orthorhombic crystalline phase of Mn_2O_3 (JCPDS No. 04-007-088) were observed for nanoparticles obtained after calcination at 800℃ (**Fig.** 3-**17**b). The average crystallite size was estimated using Debye-Scherer's formula:

$$COS\theta = \frac{K\lambda}{D} X \frac{1}{\beta_{hkl}}$$

where k = 0.99 is the shape factor λ is the x-ray wavelength ß is the full width at half maximum in radians and θ is the angle position of the maximum of diffraction peak. The average crystalline size was estimated for 600℃ and 800℃ to be estimated about 269.19 nm and 27.89

nm respectively this results confirms that of TEM which indicates the crystalline size was improved with increasing temperature.

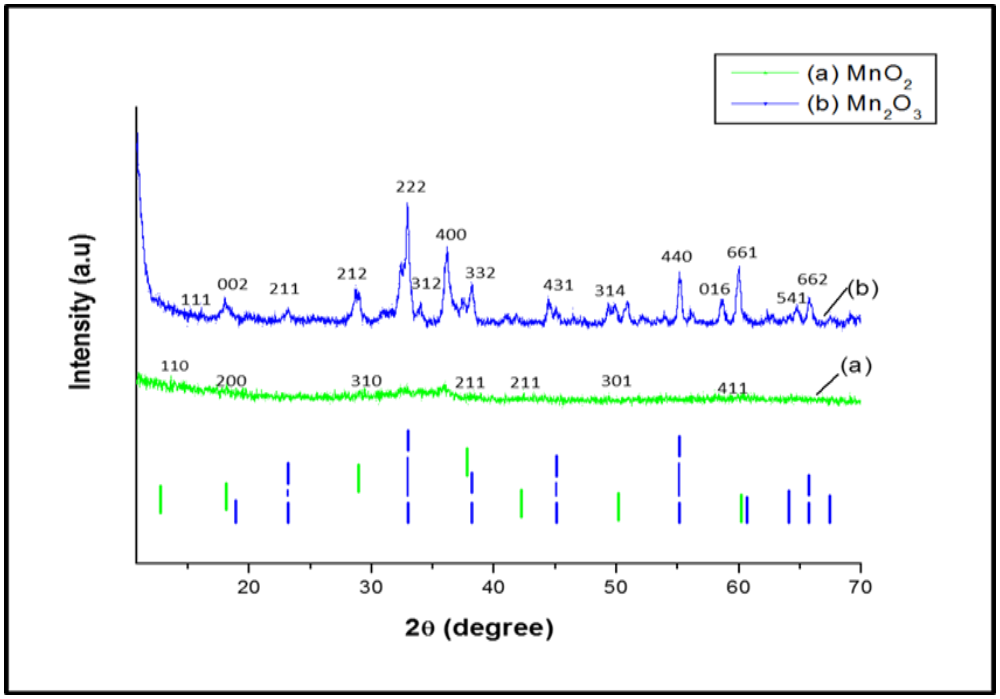

Fig. 3-17 XRD patterns of Mn_xO_y nanoparticles prepared at different temperatures (a) 600 ℃ MnO_2 and (b) 800 ℃ Mn_2O_3

3.5.3. Optical properties of manganese oxide nanoparticles

Manganese oxide nanoparticles were analysed using UV-visible spectroscopy and photoluminescence. **Fig. 3-18** (a) showed a dominate peak at 319.73 nm for nanoparticles calcined at 600 ℃ and as the temperature was increased to 800 ℃ **Fig. 3-18** (b) revealed a peak at 325.73 nm. The energy band gap, Eg was estimated as from the plot of $(\alpha h\nu)^2$ Vs hν as proposed by the Wood and Tauc and the results are represented in **Fig. 3-18** (c) and (d). The band edge and band gap energies was found to be 514 nm (2.41 eV) and 510 nm (2.43 eV) for MnO_2 and Mn_2O_3, respectively. The Tauc plot results illustrated that the increase in annealing temperature increased the band gap energy. The slight increase in the band gap energy of the manganese oxide nanoparticles might be due to the decrease in the particle size at higher annealing temperature, the band gap correlates to previous studies conducted (Kumar & Manisha, 2018). The PL results displayed a blue shift for MnO_2 nanoparticles calcined at 600 ℃ which showed a visible sharp peak at 421 nm and red shift was observed for Mn_2O_3 nanoparticles calcined at 800 ℃ that resulted in a broad peak at 454 nm, at 800 ℃ there was a

decrease of the maximum emission intensity this could be due to the change in morphology of the particles forming small crystals. According to previous literature manganese oxide nanoparticles are expected to occur within the 300 nm- 600 nm wavelength range, therefore the PL results correlate to previous studies conducted (Wang *et al.*, 2003; Yu, 2016).

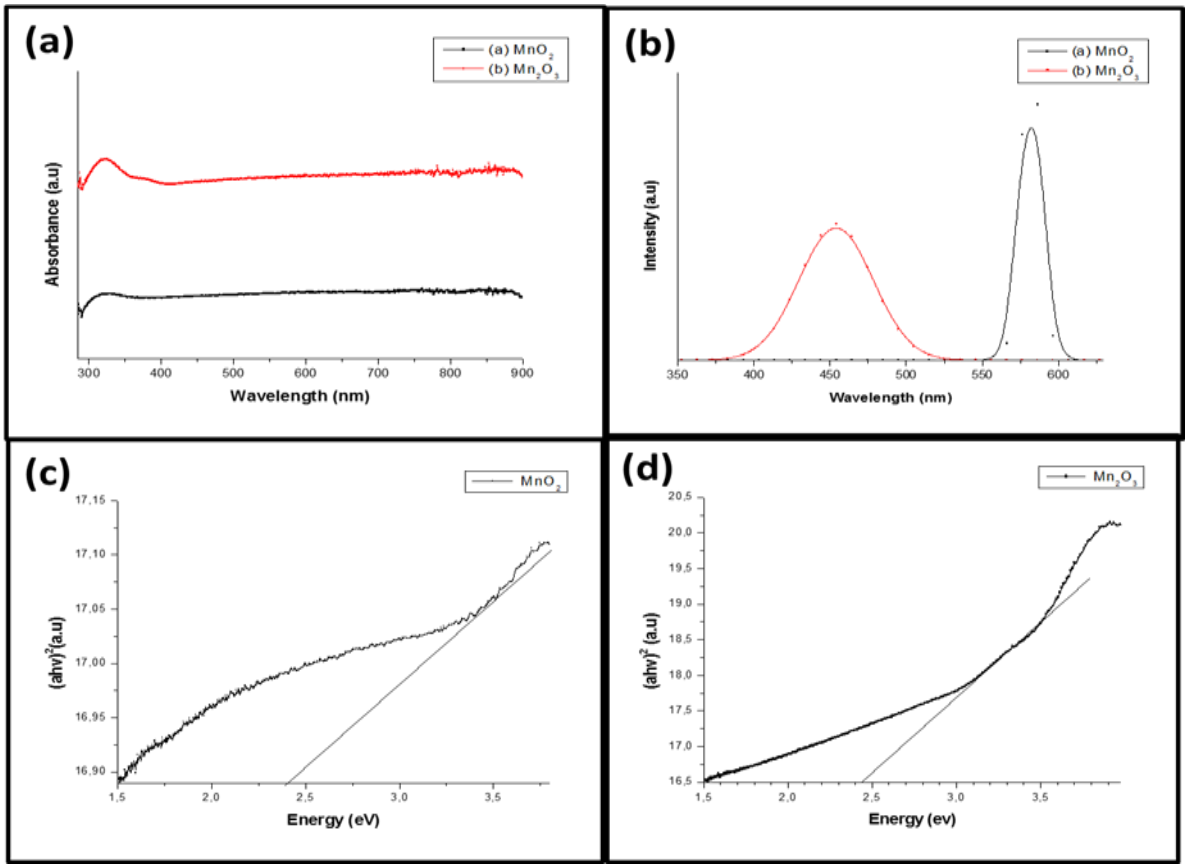

Fig. 3-18 (a) Absorption spectra, (b) Emission spectra of Mn_xO_y nanoparticles prepared at different temperatures (600℃ and 800℃). (c) and (d) is the Tauc Plot of MnO_2 and Mn_2O_3.

3.5.4. Thermogravimetric Analysis (TGA) of manganese oxide nanoparticles

The calcination temperature of the prepared manganese oxide nanoparticles did not completely volatiles ammonium hydroxide in the reaction media. Therefore, the TGA analysis were carried out to completely decompose the calcined manganese oxide nanoparticles .**Fig. 3-19** (a) and (b) indicated a weight loss of 2.59% for MnO_2 nanoparticles due to moisture which indicates that there was water present in the (K-OMS-2/MnO_2) nanoparticles. A weight loss of 0.21% was observed from 323.43℃ to 315.10℃ due dehydration of O_2 from ammonium hydroxide. A major loss of 1.26% was observed from 600℃ to 752℃ due to final decomposition of MnO_2

to Mn_2O_3. These results corresponds to the thermal analysis (DTA) studies that showed endotherms corresponding to the weight losses in TGA studies. These peaks can be associated to the thermal decomposition of MnO_2 (Kiyoshi & Masao, 1983). MnO_2 is thermally unstable at high temperatures. Therefore, the presence of K^+ ions in the reaction media act as pillaring cations to stabilize the layered framework. The highly oxidizing species produced during the thermal decomposition suppress the suboxide transition. **Fig. 3-19** (c) and (d) indicated a weight loss of 3.8% of K-OMS/Mn_2O_3 between 30 and 400℃ due to evaporation of water. Further dehydration of O_2 (lose of H_2O from ammonium hydroxide) starts at 400℃.

According to literature this observation is related to the intermediate phase metastable oxide (Mn_5O_8) that usually appears above 300 ℃ (Sanfélix, 2016). 3.9% weight loss was observed at a range of 400 to 600℃. The large peak for O_2 around 615℃ contributes to 2.2% loss in the range of 600-800℃. These results are similar to other studies previously conducted for thermal decomposition of Mn_2O_3 (Chen *et al.*, 2002; Rajendran, 2011). It is well- known that manganese oxide can exist in different structural forms, α, β, γ and δ types and unstable at high temperatures .The chosen calcination temperatures of 600 and 800℃ formed highly crystalline layered K-OMS nanoparticles without noticeable impurities of different manganese oxide phases under thermal decomposition (Kim et al., 1999) , therefore thermal decomposition states of MnO_2 and Mn_2O_3 only differ due to dehydration of the O_2 during phase transitions of the MnO_2 to Mn_2O_3 nanoparticles in **Fig. 3-19** (c). DTA of Mn_2O_3 nanoparticles showed endothermic peaks which correlates with TGA results. Mn_2O_3 showed strong thermal stability compared to MnO_2, therefore it will be useful for incorporation studies with polymer fibre blends to enhance the mechanical strength, optical properties and hydrophilicity of the polymer fibre blends.

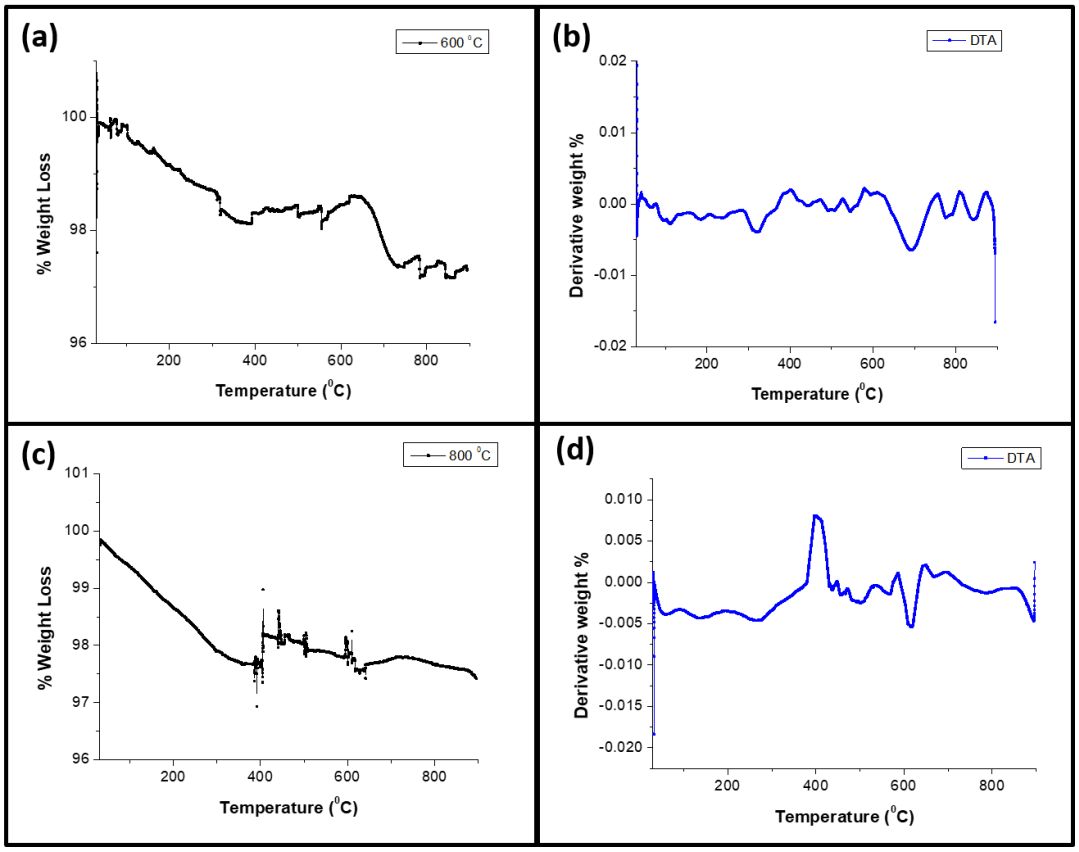

Fig. 3-19 Thermogravimetric analysis (TGA) and differential thermal analysis (DTA) plot for the calcined decomposition of (a), (b) 600℃ (K-OMS/MnO_2) and (c), (d) 800℃ (K-OMS/Mn_2O_3) nanoparticles.

3.6. Incorporation of Fe_2O_3 nanoparticles on zein/PVA fibre blends

3.6.1. Effect of Fe_2O_3 nanoparticles embedded onto zein/PVA fibre blends.

Metal oxide nanoparticle-polymer nanocomposites have attracted the interest of researchers. The addition of nanoparticles into polymers produces nanocomposites that are known to improve mechanical strength, resistance to wear and thermal stability of nanocomposites therefore very low addition of metal oxides nanoparticles enhance the functional properties of nanocomposites. Suhasini et al., (2018) studied the synthesis, thermal and magnetic behaviour of iron oxide-polymer nanocomposites. It was reported that Fe_2O_3 in the polymer composites was in the nanoscale and uniform dispersion was achieved. **Fig. 3-20** of SEM images shows the different concentration of α-Fe_2O_3 nanoparticles prepared at 140℃ which were embedded onto zein/PVA fibre blends under the same processing condition (voltage, 25 kV and TCD

10cm). **Fig. 3-20** (a) showed interconnected fibre morphology with an average diameter of 498 ± 0.62 nm which is thinner compared to 25 wt% zein/PVA fibre blends. The addition of α-Fe_2O_3 nanoparticles improved the fibre morphology it looked coarse and rough, there was an increase in the stretching fibres as a result of increased conductivity. **Fig. 3-20** (b) revealed that there was an increase in the average diameter of the α-Fe_2O_3 /zein/PVA nanocomposite from 498 ± 0.62 nm to 768 ± 0.66 nm due to increase in charge density. The charge density is because of concentration increment of the α-Fe_2O_3 nanoparticles which are visibly tiny on the surface of the polymer fibre blends and had a smooth thick surface. **Fig. 3-20** (c). The morphology revealed of the nanocomposite was thinner, relatively coarse and rough and it can clearly be seen that tiny nanoparticles were formed on the surface of the polymer fibre blends. The average diameter decreased significantly from 768 ± 0.66 nm to 729 ± 0.64 nm due to the increase in surface area and enhanced electrospinnabilty.

The results obtained illustrated that the 5.25 wt% α-Fe_2O_3 nanoparticles were effectively embedded on to zein/PVA fibre blends and corresponds to a similar study conducted by Wei et al. More *et al.* (2015) studied TOPO-capped silver selenide nanoparticles and their incorporation into polymer nanofibres using electrospinning technique. It was reported that Ag_2Se/PVA composite fibre electrospun at 17 kV displayed greater stretching of the solution due to the greater columbic forces in the jet as well as a stronger electric field, and these effects led to the reduction in the fibre diameter and also a rapid evaporation of solvent therefore the results obtained from our study of α-Fe_2O_3 /zein/PVA nanocomposites showed a similar trend.

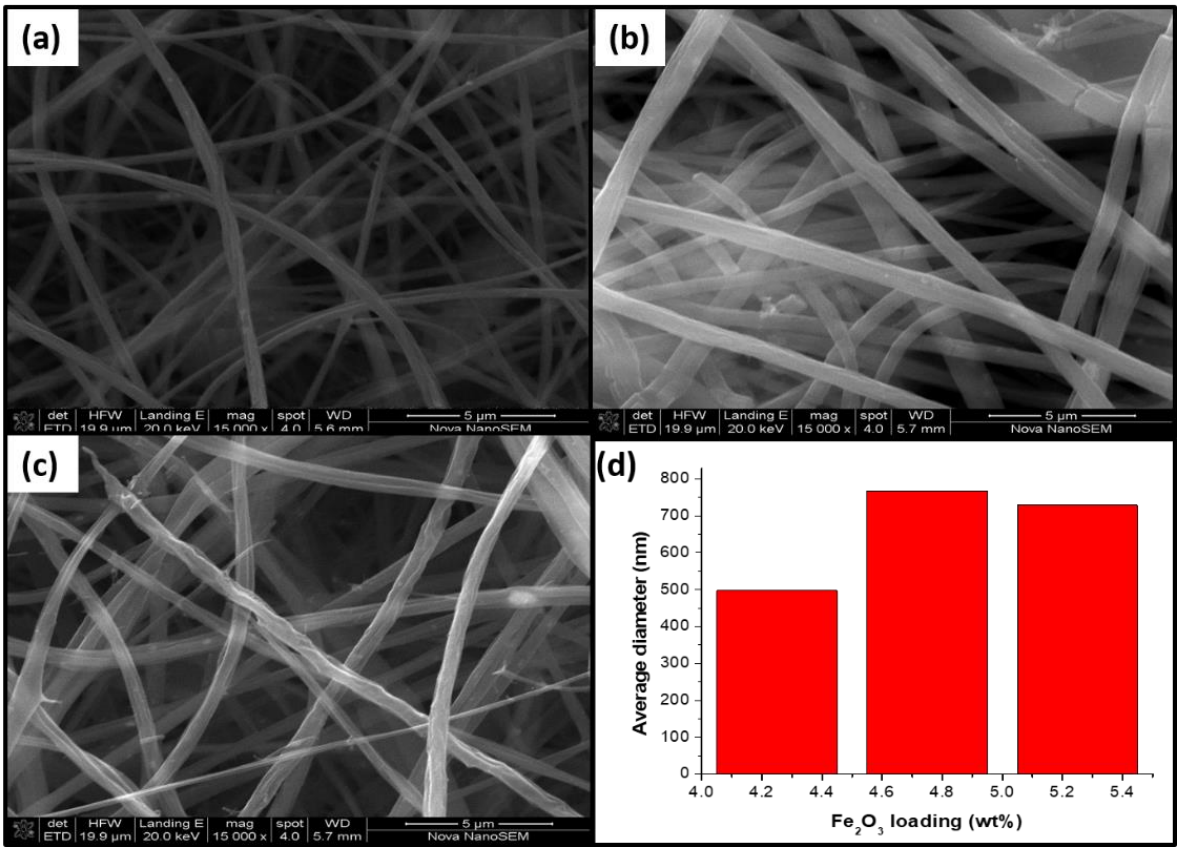

Fig. 3-20 SEM images and fibre size distribution of α-Fe_2O_3/zein/PVA nanocomposites with different loading of the nanoparticles (a) 4.25 wt% (b) 4.75 wt% (c) 5.25 wt%. voltage: 25kV and working distance: 10cm

3.6.2. Optical properties of Fe_2O_3 nanoparticles embedded onto zein/PVA fibre blends.

Metal oxide polymer nanocomposites exhibit good electrical and optical properties and it has long been an interest for researchers. UV-vis absorption of zein/PVA fibre blends embedded with different concentrations of α-Fe_2O_3 nanoparticles prepared at 140℃ was analysed. **Fig. 3-21** (a) and (c) displayed an excitonic peaks at ~326 nm for all α-Fe_2O_3/ zein/ PVA fibre blends which were blue shifted compared to α-Fe_2O_3 nanoparticles alone (**Fig. 3-13**b) The band edges and band gap for the different concentrations of embedded α-Fe_2O_3 nanoparticles into zein/PVA nanofibre blends were 319 nm (3.88 eV), 330 nm (3.75 eV), and 430 nm (2.88 eV) for 4.25 %, 4.75 % and 5.25 wt%. The band edge for 5.25 wt% decreased significantly due to improved morphology of the nanocomposite .**Fig. 3-21** (b) is the photoluminescent results which displayed a peak at (a) 425 nm (b) 417 nm and (c) 416 nm which were blue shifted for the different concentrations of α-Fe_2O_3/zein/PVA nanocomposite. The peak at 425 nm for 4.25

wt% α-Fe_2O_3/ zein/ PVA appeared to have lower intensity indicating that the crystal size of the nanoparticles was smaller compared to 4.75 wt% and 5.25 wt% nanocomposite. Singh et al., (2009) studied the optical properties of zinc oxide/polymer nanocomposite and reported the size of synthesized polymer /ZnO nanocomposite material increased with the increment of polymer weight ratio. Therefore the results obtained in our study illustrate that increase in the concentration of embedded α-Fe_2O_3 nanoparticles increases the intensity which has an effect on the morphology of the fibre blends and quantum confinement.

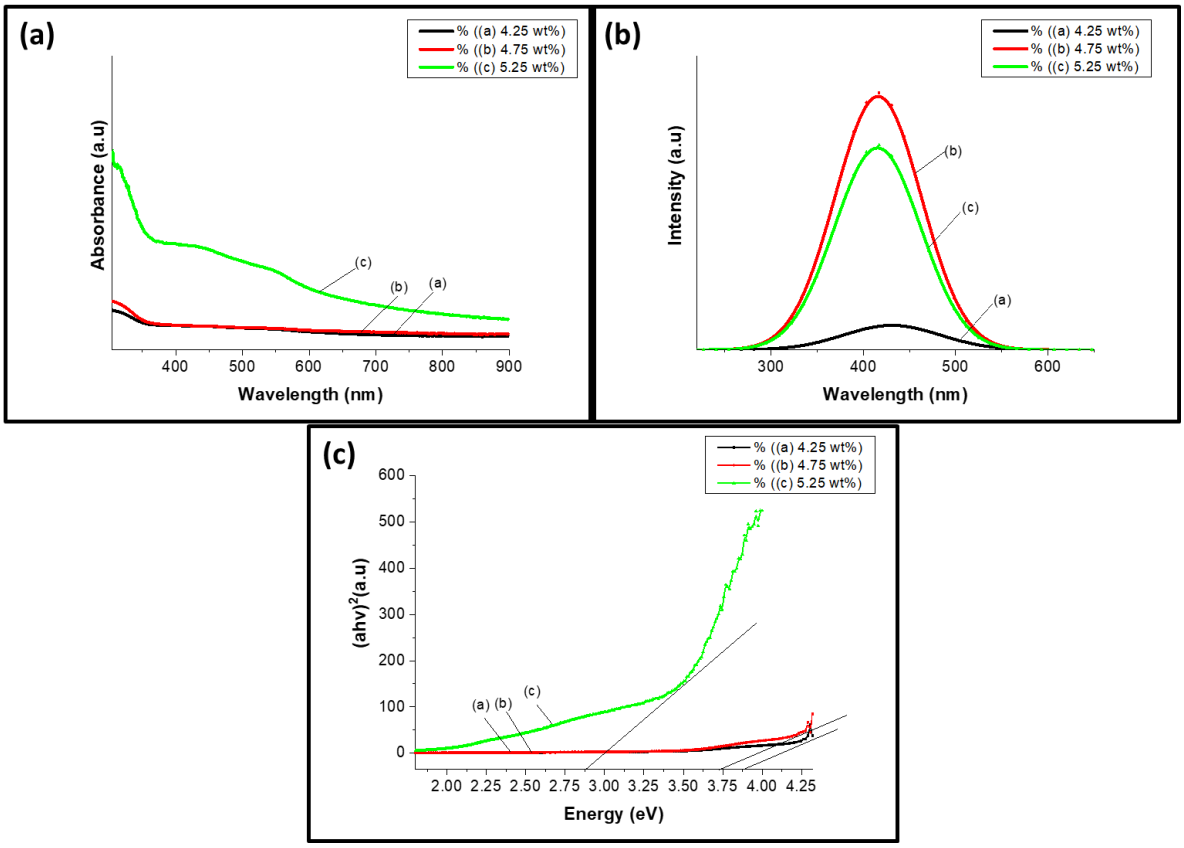

Fig. 3-21 (a) UV visible spectra of α-Fe_2O_3/zein/PVA nanocomposites (b) Photoluminescence spectra of α-Fe_2O_3 and (c) their corresponding Tauc plot for direct transitions.

3.6.3. XRD patterns of Fe_2O_3 nanoparticles embedded onto zein/PVA fibre blends

The crystallinity of α-Fe_2O_3/ zein/ PVA nanocomposite was performed using XRD analysis. **Fig. 3-22** (a) revealed a broad amorphous peak at 2θ = 19.5º and 20.4º which is the characteristic of zein/PVA fibre blend. The amorphous peak and peaks of the specimen holder suppress the crystal peaks of α-Fe_2O_3 nanoparticles hence there are no visible crystal peaks of α-Fe_2O_3 nanoparticles even at higher loading of 5.25 wt% due to the nanoparticles being below

the detection limit of XRD. It was observed that 4.75 wt% and 5.25 wt% α-Fe_2O_3 nanocomposite showed less amorphous peaks of the zein/PVA and the peaks of the specimen holder which are similar to **Fig. 3-22** (b) become less intense as the concentration loading of α-Fe_2O_3 nanoparticles increased. The α-Fe_2O_3/ zein/ PVA nanocomposite of 4.75 wt% showed the least amorphous phase compared to 5.25 wt% this might be due to constrained nature of the zein/PVA chains by α-Fe_2O_3 nanoparticles through the formation of hydrogen bonds of PVA and α-Fe_2O_3 nanoparticles. Therefore the crystallinity of the polymer fibre blends decreased with concentration increment of 4.25 wt% α-Fe_2O_3 nanoparticles. As the concentration further increased to 5.25 wt% the zein/PVA peak become more amorphous .This may be due to the phase separation between α-Fe_2O_3 and zein/PVA fibre blends, which increased the crystallinity of the polymer fibre blend and improved the morphology of the nanocomposite as shown in SEM images. From the results, it can be observed that, the crystalline nature of the zein/PVA is largely reduced with the incorporation of 5.25 wt % of α-Fe_2O_3 nanoparticles and the peaks became narrower hence, this composition exhibited more amorphous nature compared to 4.75 wt% which helped in improving the conductivity and mechanical strength of the polymer fibre blends. Generally, low crystallinity will enlarge the amorphous nature, which results in the enhancement of electrospinnabilty. This results are similar to a study conducted previously by Senthil et al.

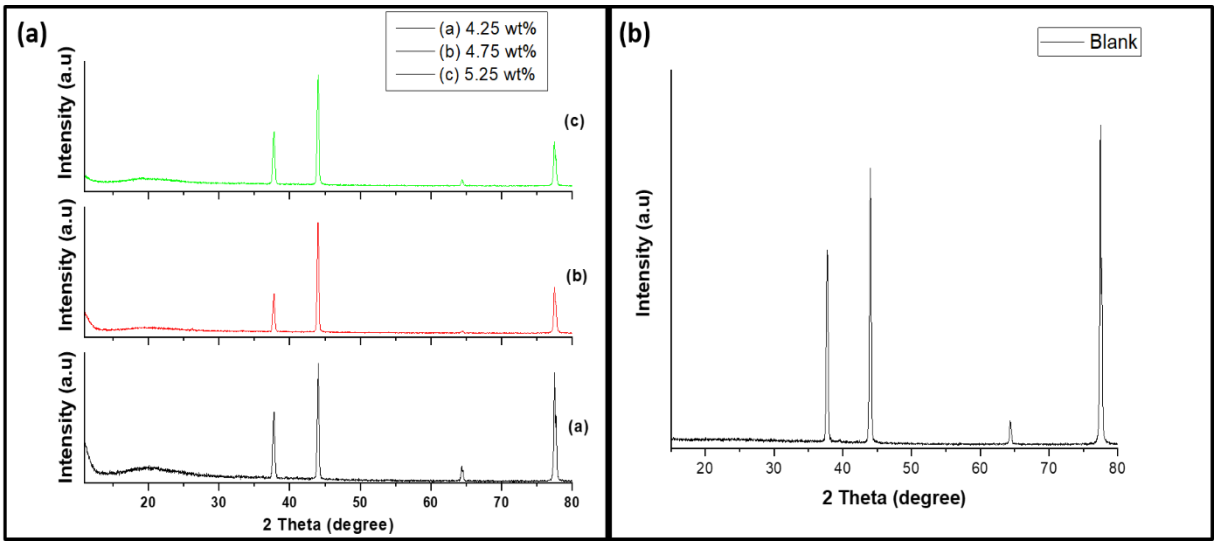

Fig. 3-22 XRD patterns of (a) $\boldsymbol{\alpha}$-Fe_2O_3/ zein /PVA blend solutions with different concentrations of α-Fe_2O_3 nanoparticles and (b) zero background holder.

3.6.4. FTIR Spectra of Fe_2O_3 nanoparticles embedded onto zein/PVA fibre blends

The α-Fe_2O_3/zein/PVA nanocomposites were characterized using FTIR spectroscopy to determine any changes in the structure's functionality of the nanocomposites due to any chemical interaction between the polymer fibre blend (zein/PVA) and α-Fe_2O_3 nanoparticles. **Fig. 3-23** showed the characteristic absorption band of hydrogen bond recorded as 3281, 3285, and 3294 cm^{-1} for 4.25 wt%, 4.75 wt% and 5.25 wt%. The C=O stretching frequency observed at 1644 cm^{-1} for 4.25 wt% and a peak of 1651cm^{-1} for 4.25 wt% and 5.25 wt%, were found, conforming to a stronger intermolecular interaction among amide groups in α-Fe_2O_3/ zein/ PVA .The amide II of zein fibres appeared at 1532, 1534 and 1535 cm^{-1} which indicates that loading iron oxide does not disrupt the - α -helical structure of zein

However, the amide I, amide II and hydrogen bond were broadened as the concentration of iron oxide increased for 4.75 wt% and 5.25 wt % which suggests that the interactions between the α-Fe_2O_3 nanoparticles and zein/PVA were physical, consisting of hydrogen bond and mostly hydrophobic interactions (Ghalei et al., 2018). The characteristic absorption peak of iron oxide cannot be seen in the FTIR spectra of α-Fe_2O_3/zein/PVA nanocomposite (Musi & Santana, 1999; Lassoued *et al.*, 2017). This might be due to the presence of low percentage content of nanoparticles in the polymer composites. Again, the nanoparticles were ingrained or embedded in the zein/PVA solution which could supress the absorption band of iron oxide resulting the missing of characteristic IR absorption of the nanoparticles in polymer composites. Therefore these results are similar to reports previously conducted by (Hoque et al., 2018; Suhasini et al., 2018).

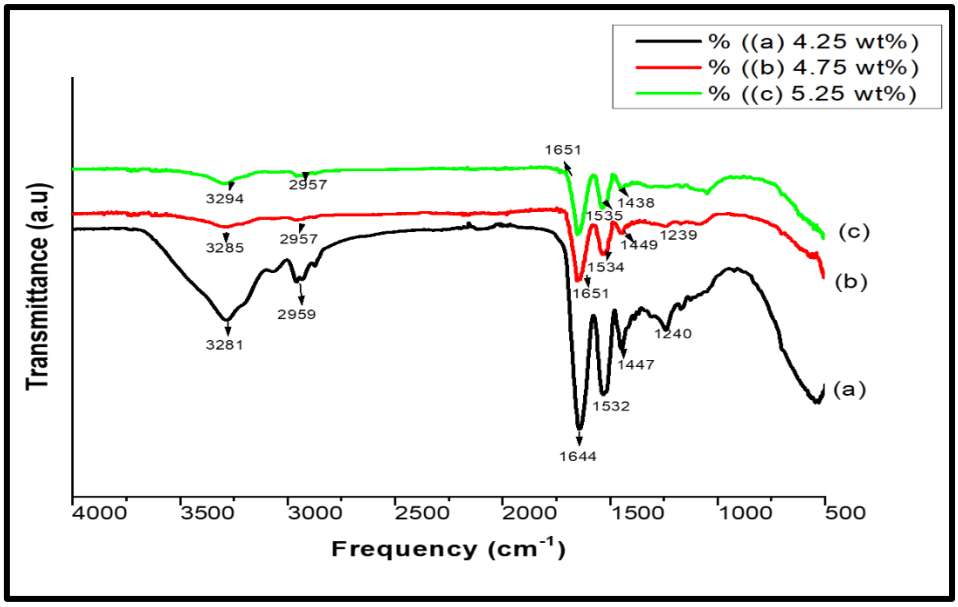

Fig. 3-23 FTIR spectra of α-Fe_2O_3 /zein/PVA fibre blends with different concentrations of α-Fe_2O_3 nanoparticles (a) 4.25 wt % , (b) 4.75 wt % and (c) 5.25 wt%.

3.6.5. Thermogravimetric Analysis (TGA)

The thermal analysis (TGA, DTA) of the α-Fe_2O_3/zein/PVA nanocomposite were carried out from 30℃ to 900℃. **Fig. 3-24** (a) depicts three weight loss for 4.25 wt% α-Fe_2O_3/zein/PVA nanocomposite, the first stage is about 15.5 % weight loss below 100℃ which is due to evaporation of moisture in the material. A sharp weight loss of 71.71% occurred between 250℃ and 506℃ which was due to decomposition of zein/PVA. Another weight loss was observed between 506℃ and 870℃ which was due to the final decomposition of α-Fe_2O_3 nanoparticles. The DTA results provided detailed information on the exact endothermic temperatures of α-Fe_2O_3/zein/PVA nanocomposites. **Fig. 3-24** (b) depicts a weight loss of about 1% below 100℃ for 4.75 wt% α-Fe_2O_3/zein/PVA nanocomposite. A major weight loss of 61.79% was observed between 278℃ and 506℃ which was due to the decomposition of zein/PVA with an excess of 4.95% residue of α-Fe_2O_3 nanoparticles towards final decomposition. According to literature (Lassoued et al., 2018) hematite prepared by hydrothermal method, the phase transition occurs at a temperature of approximately 697.27℃ to 870℃.

The results obtained from this current study corresponds to the SEM results **Fig. 3-20 (**b) illustrated that excess α-Fe_2O_3 nanoparticles attributed to the large average diameter as the nanoparticles were also visible on the surface of the morphology. Which also resulted in higher decomposition temperature of 4.75 wt% compared to 4.25 wt% and 5.25 wt% α-

Fe_2O_3/zein/PVA nanocomposites. **Fig. 3-24** (c) Depicts six distinct weight loss steps in the temperature ranges. There was a weight loss of 12.97% for α-Fe_2O_3 nanoparticles from 59℃ to 86.66℃ due to moisture. The second major decomposition stage of about 49.2% occurred between 262℃ to 448℃ due to decomposition of zein/PVA. The third minor weight loss was about 6.49% between 448℃ to 472℃ due to decomposition of HMDA (methylene, amide groups) on the surface of nanoparticles embedded on the nanofibre blends. Another major weight loss occurred at about 30.23% between 472℃ to 523℃ this was due to the final decomposition of the α-Fe_2O_3 nanoparticles embedded into the polymer blends and the last decomposition stage at 826℃ was due to final decomposition of the residue of α-Fe_2O_3/zein/PVA nanocomposite this results were similar to a study reported by Samanta et al. The TGA of 5.25 wt% **Fig. 3-24** (c) was observed to be more thermally stable and there is strong interaction between the α-Fe_2O_3 and zein/PVA fibre blends. The DTA results for all α-Fe_2O_3/zein/PVA nanocomposite corresponds to the endothermic peaks similar to those of TGA studies. After the final endothermic peaks of the different nanocomposites it was observed that the curves became parallel to the temperature axis. This indicated that the α-Fe_2O_3/zein/PVA nanocomposites were thermally stable. There was no signal associated with the thermal processes on DTA curves confirming that there was no phase transition of α-Fe_2O_3 nanoparticles embedded on zein/PVA fibre blends (Zhu *et al.*, 2010; Lassoued *et al.*, 2017). Zhang et al. (2019) studied a simple preparation of HDA-CuS nanoparticles and their tribological properties as a water-based lubrication additive. It was reported that HDA-CuS nanoparticles can significantly improve the thermal conductivity of distilled water and the TGA results reported was similar to our study.

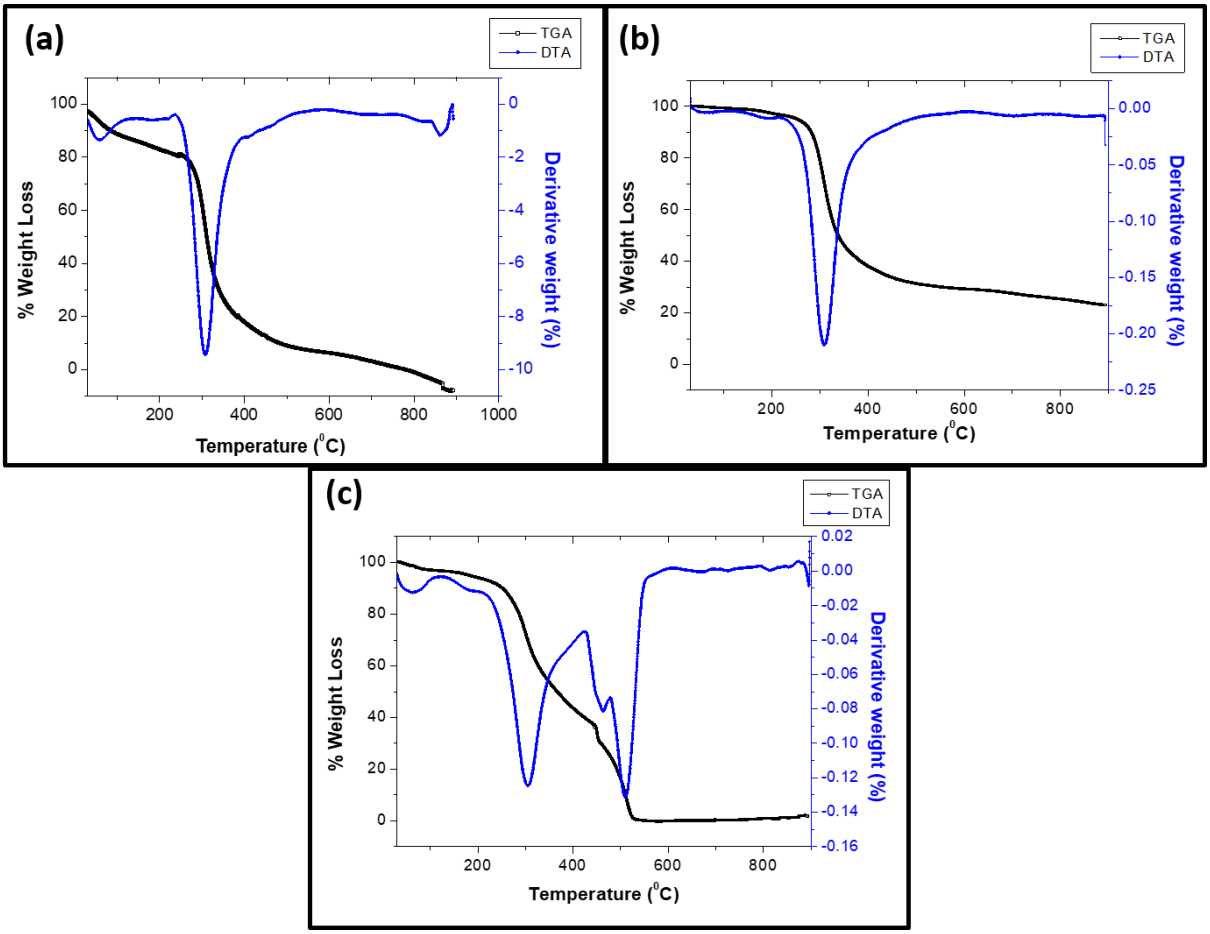

Fig. 3-24 TGA-DTA thermograms of α-Fe_2O_3 /zein/PVA fibre blends with different concentrations of α-Fe_2O_3 nanoparticles (a) 4.25 wt %. (b) 4.75 wt % and (c) 5.25 wt% electrospun at 25 kV and distance: 10 cm

3.7. Incorporation of Mn_2O_3 nanoparticles on zein/PVA fibre blends.

3.7.1. Effect of Mn_2O_3 nanoparticles embedded onto zein/PVA fibre blends

Manganese oxides have been a subject of interest in various fields including molecular adsorption due to their outstanding structural multiformity combined with novel chemical and physical properties (Maliyekkal *et al.*, 2010). The incorporation of manganese oxides into polymer fibres has been of interest in environmental remediation because of their low cost, less toxicity and wide availability**.** According to literature the addition of nanoparticles into polymeric solution increases the viscosity. Enhancement of viscosity is also proved to have an effect on polymeric nanofibre diameters (Reitzenstein *et al.*, 2016).

Fig. 3-25 of SEM images shows the different concentration of Mn_2O_3 nanoparticles embedded onto zein/PVA fibre blends under the same processing condition (voltage, 25 kV and TCD

10cm). **Fig. 3-25** (a) revealed that the addition of Mn_2O_3 nanoparticles reduced the average size fibre diameter resulting in narrow nanocomposite fibres with an average diameter of 793 ± 1.31 nm, the morphology appeared to be smooth with nanoparticles embedded onto zein/PVA polymer blend. **Fig. 3-25** (b) showed an increase in average fibre diameter of 1136 ± 1.32 nm and the morphology of the nanocomposite blend increased significantly this might be due to Mn_2O_3 nanoparticles not being fully dispersed or easy dispersed because of the amphiphilic nature of the zein/PVA fibre blends which corresponds to similar study conducted by Chen *et al*. **Fig. 3-25** (c) revealed that there was a decline in the averaged fibre diameter to 747 ± 1.29 nm this was due to increased concentration of the Mn_2O_3 nanoparticles which resulted in increase in surface area, conductivity and stronger interaction between the nanoparticles and the composite fibre blends although the exact mechanism of growth and corresponding kinetics of the formation of such structures is not clear (Chatterjeeet al., 2009; Rejania & Beena 2013).

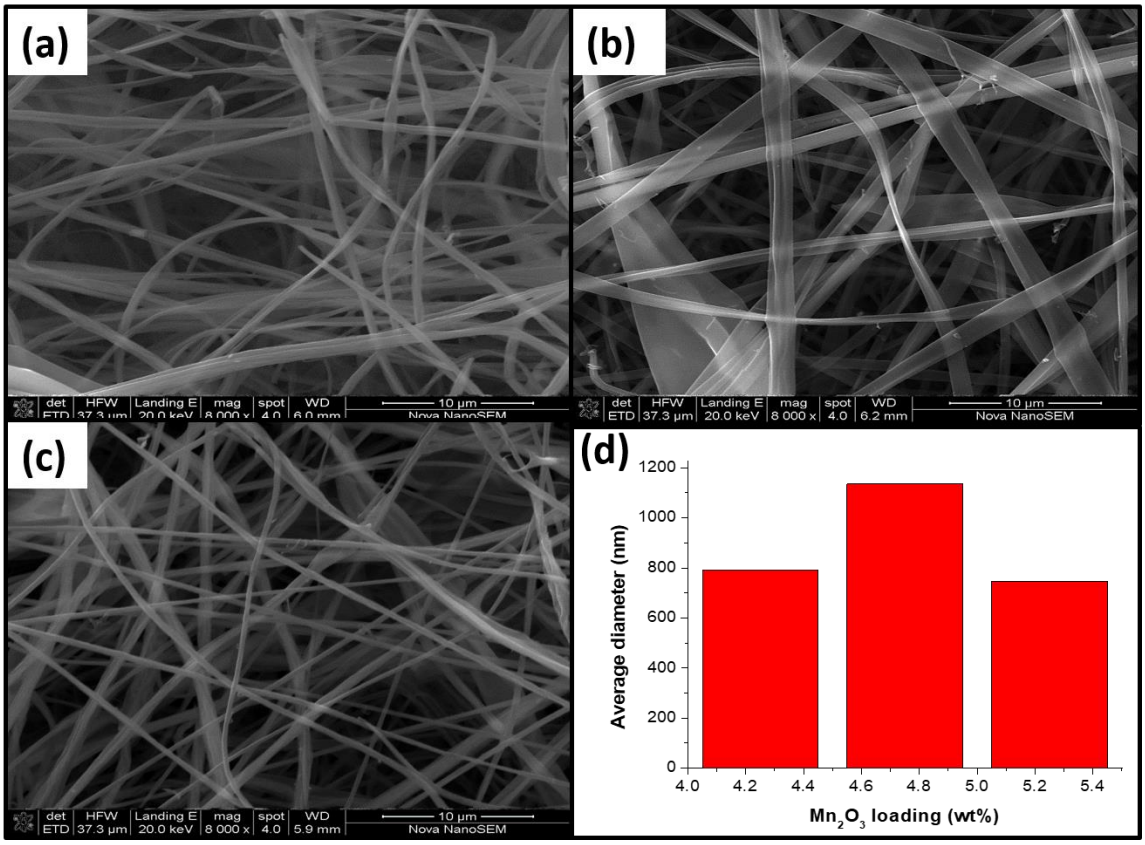

Fig. 3-25 SEM images and fibre size distribution of Mn_2O_3/zein/PVA nanocomposites with different loading of the nanoparticles (a) 4.25 wt% (b) 4.75 wt% (c) 5.25 wt%. Voltage: 25kV and working distance: 10cm

3.7.2. Optical properties of Mn_2O_3 nanoparticles on zein/PVA fibre blends

Metal oxide nanoparticles embedded onto polymer fibre blends show distinctive properties, different from the individual metal oxide nanoparticles. Moloto *et al.*, (2009) studied the morphological and optical properties of MnS / polyvinylcarbazole hybrid composites and reported that there was a strong interaction between the nanoparticles and the polymer while the absorption and photoluminescence spectra showed improved properties. The optical study of the prepared samples incorporated with Mn_2O_3 nanoparticles and calcined at 800 ºC was performed using the UV-visible optical spectroscopy obtained in the range of 200–900 nm. **Fig. 3-26** (a) and (c) displayed an excitonic peak at 320 nm that is blue shifted for 4.25 wt% Mn_2O_3/zein/PVA with a band edge of 332 nm (3.73 eV). This may be due to the lower concentration of the Mn_2O_3 nanoparticles present in the zein/PVA fibre blends.

The bulk of 4.75 wt% Mn_2O_3/zein/PVA with a band edge of 413 nm (3.64 eV) displayed an excitonic peak at 322 nm which was red shifted from the 4.25 wt% Mn_2O_3/zein/PVA. This may be due to quantization of energy levels causing an increase in the band gap energy. 5.25 wt% Mn_2O_3/zein/PVA nanocomposite fibre blends displayed an excitonic peak at 319 nm that was blue shifted and broader with a band edge of 311 nm and a sufficiently increased band gap of 3.98 eV. The broadness may be portraying the polydispersed nanoparticles. The high absorbance illustrates additional confirmation of decrease in particle size of nanoparticles at pH 12 and high concentration of Mn_2O_3 nanoparticles (Najjar & Abdel-gaber, 2018; Swaroop & Somashekarappa, 2015). **Fig. 3-26** (b) is the photoluminescent results which displayed peaks at 431 nm, 459 nm and 493 nm for the different concentrations of Mn_2O_3/zein/PVA nanocomposite fibre blends. A blue shift was observed for 4.25 wt% Mn_2O_3/zein/PVA this may be due to the quantum confinement effect and morphology of the nanocomposite. The 4.75 wt% and 5.25 wt% Mn_2O_3/zein/PVA nanocomposite fibres were also blue shifted illustrating that an increase in concentration of the nanoparticles can result in increase in the band gap energy, quantization of energy levels and the change in morphology of the nanocomposite fibres. Therefore 5.25 % is the optimum concentration on which is also in agreement with the SEM results due to smoother morphology, decreased fibre diameter compared to other concentrations of Mn_2O_3/zein/PVA nanocomposite fibres. Rejania & Beena, (2013) studied the structural and optical properties of polyindole-manganese oxide nanocomposite (Mn_2O_3/PI). It was reported that polyindole has direct band gap which

decreased with hybrid formation from 4.4eV PI to 3.3eV Mn_2O_3/PI. Therefore the deviation of other research studies previously conducted to this study may be related to factors such as the morphology, quantum confinement of the nanoparticles and band gap energies of the nanocomposite materials.

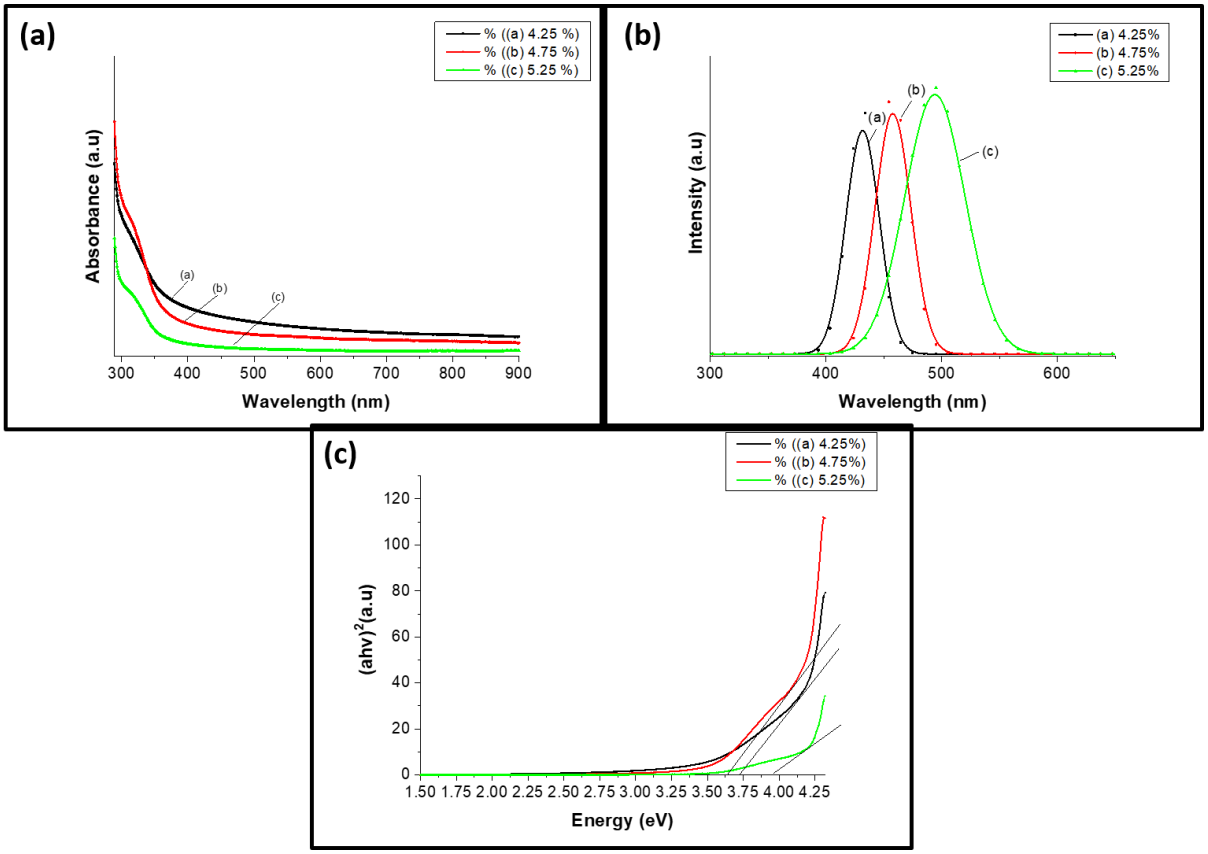

Fig. 3-26 (a) UV spectra of Mn_2O_3/zein/PVA nanocomposites, (b) Photoluminescence spectra of Mn_2O_3 and (c) Tauc plot for direct transitions.

3.7.3. XRD patterns of Mn_2O_3 nanoparticles embedded onto zein/PVA fibre blends

Fig. 3-27 (a) show the XRD pattern of Mn_2O_3/zein/PVA interface with a broad amorphous peak at $2\theta = 19.5^o$ and 20.4^o which is the characteristic of zein/PVA fibre blend. The amorphous peak and peaks of the specimen holder suppress the crystal peaks of Mn_2O_3 nanoparticles hence there are no visible crystal peaks of Mn_2O_3 nanoparticles even at higher loading of 5.25 wt%, It is revealed that 4.75 wt% and 5.25 wt% nanocomposites showed less amorphous peaks of zein/PVA fibre blends and the peaks of the specimen holder which are similar to **Fig. 3-27**

(b) become less intense as the concentration loading of Mn_2O_3 nanoparticles increased especially at 4.75 wt% Mn_2O_3 nanoparticles loading which suggest that the increment in concentration of the nanoparticles enhanced conductivity during electrospinning. Although the nanoparticles present in the nanocomposites attributed to small crystallite size, which is apparently below the detection limit of XRD. These results are similar to a study conducted previously by Maliyekkal et al.

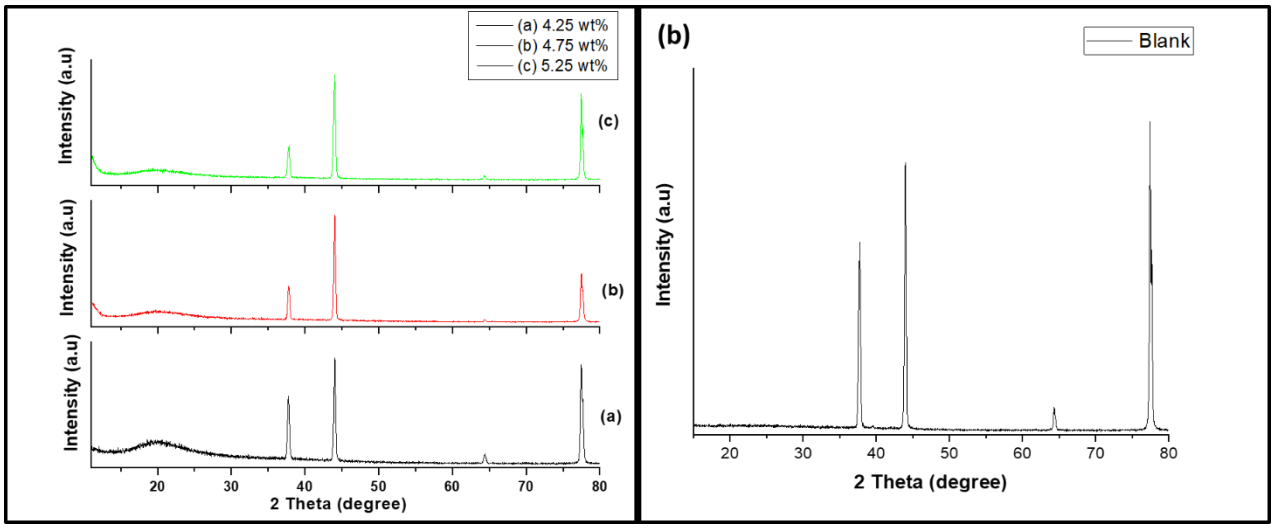

Fig. 3-27 XRD patterns of (a) Mn_2O_3/ zein /PVA blend solutions with different concentrations of Mn_2O_3 nanoparticles, (b) zero background holder.

3.7.4. FTIR Spectra of Mn_2O_3 nanoparticles on zein/PVA fibre blends

Fig. 3-28 shows the FTIR spectra of Mn_2O_3/zein/PVA. It showed the characteristic absorption band of hydrogen bond recorded as 3291, 3289, and 3288 cm^{-1} for 4.25 wt%, 4.75 wt% and 5.25 wt%. The C=O stretching frequency observed at 1644 cm^{-1} conformed strong intermolecular interaction among amide groups in α-Fe_2O_3/ zein/ PVA .The amide II of zein fibres appeared at 1532, 1536 and 1516 cm^{-1} which indicates that loading manganese oxide does not disrupt the - α -helical structure of zein. The characteristic strong absorption bands of manganese oxide at ~690, and ~ 570 cm^{-1} cannot be seen in the FTIR spectra of α-Mn_2O_3/zein/PVA nanocomposite (Nassar *et al.*, 2016). Kumar & Manisha (2018) studied the synthesis and characterization of Mn / polyaniline nanocomposites via in situ approach. It was reported that the FTIR spectra of the PANI/MnO_2 nanocomposite had a band in the regions over 400 cm^{-1}. The bands were assigned to Mn-O stretching vibrations and some bands were similar to those of PANI alone. Although the bands' characteristic of polymer backbone at 1,500 and 1,600 $cm^{-1}$are shifted to higher values after annealing indicating deprotonation. It

was therefore concluded that FTIR spectra confirmed the presence of both components in the nanocomposite. Therefore, these results deviate from results obtained by some research studies previously published. This might be due to the presence of low percentage content of nanoparticles in the polymer composites (Chen *et al.*, 2010).

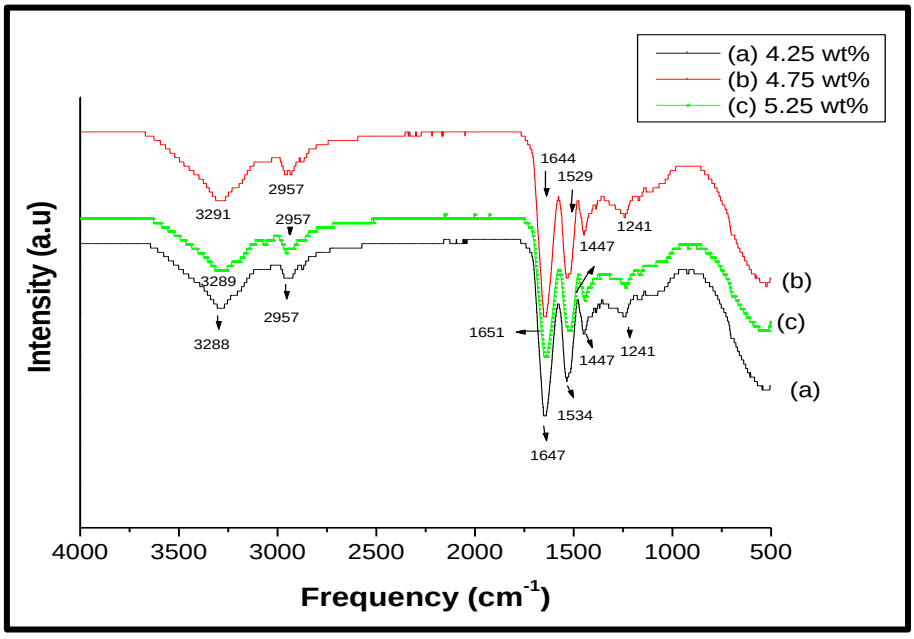

Fig. 3-28 FTIR spectra of α-Mn_2O_3 /zein/PVA fibre blends with different concentrations of α-Mn_2O_3 nanoparticles (a) 4.25 wt % , (b) 4.75 wt % and (c) 5.25 wt%

3.7.5. Thermogravimetric Analysis (TGA) of Mn_2O_3 nanoparticles on zein/PVA fibre blends

The thermal analysis (TGA, DTA) of the α-Mn_2O_3/zein/PVA nanocomposite were carried out from 30℃ to 900℃. **Fig. 3-29** (a) depicts three weight loss for 4.25 wt% α-Fe_2O_3/zein/PVA nanocomposite, the first stage is about 4.15 % below 100℃ which is due to evaporation of moisture in the material. A sharp weight loss of 59.18% occurred between 271℃ and 416℃ which was due to decomposition of zein/PVA. Another weight loss was observed between 416℃ and 592℃ which was due to the decomposition of α-Mn_2O_3 nanoparticles present in the nanofibre blends. **Fig. 3-29** (b) depicts three weight loss of about 4.54 % below 100℃ for 4.75 wt% α-Mn_2O_3/zein/PVA nanocomposite and sharp major weight loss of 62.76 % was observed between 244℃ and 308℃. The third thermal decomposition occurred between 464℃ and 563℃ this may be due to decomposition of zein/PVA fibre blend and the final decomposition observed at 563℃ to 700℃ may be due to complete decomposition of α-Mn_2O_3 nanoparticles.

Fig. 3-29 (c) depicts a weight loss of about 4.96 % below 100℃ for 4.75 wt% α-Mn_2O_3/zein/PVA nanocomposite and sharp major weight loss of 49.22 % was observed between 279℃ and 346℃. The third thermal decomposition occurred between 421℃ and 558℃ this may be due to decomposition of zein/PVA fibre blend and the final decomposition observed at 563℃ to 776℃ may be due to complete decomposition of α-Mn_2O_3 nanoparticles. 5.25 wt% was observed to be thermally stable due to the prolonged final decomposition stages this may be attributed by the increment content of α-Mn_2O_3 nanoparticles into zein/PVA fibre blends. The results obtained are similar to a study reported by Najjar & Abdel-gaber (2018).

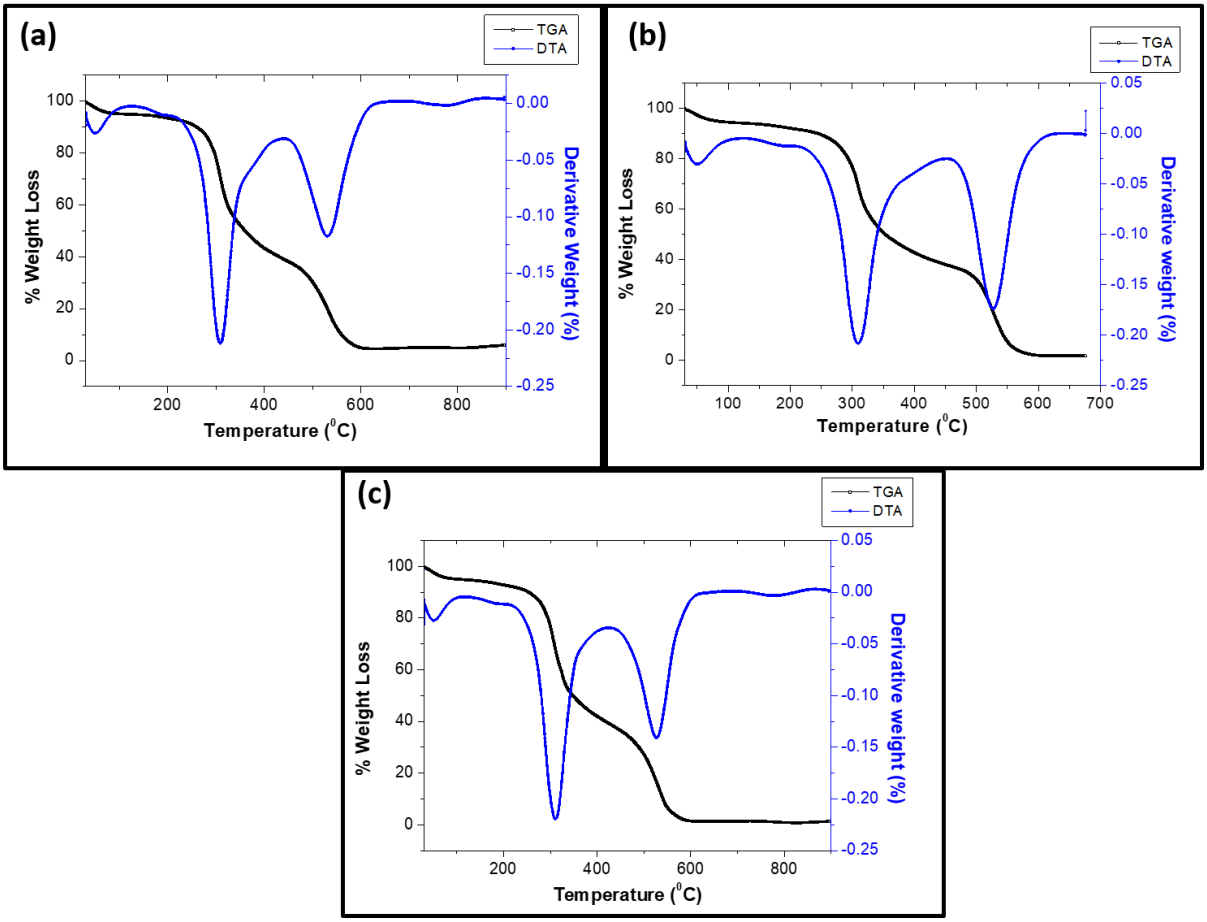

Fig. 3-29 TGA-DTA thermograms of α-Mn_2O_3 /zein/PVA fibre blends with different concentrations of α-Fe_2O_3 nanoparticles (a) 4.25 wt %. (b) 4.75 wt % and (c) 5.25 wt% electrospun at 25 kV and distance: 10 cm

3.7.6. Conclusions

Zein nanofibres were varied at three different concentrations (20 wt%, 25 wt% and 30 wt %) and voltages (15 kV, 20 kV and 25 kV) using the electrospinning technique. The SEM results

illustrated that the morphology of the nanofibres improved as solution concentration and voltage was increased. It was observed that increment of voltage had an impact on the reduction of the average diameter of the nanofibres which contributed to the uniformity of fibre morphology. Therefore, 25 wt % and 25 kV was regarded as the optimum conditions for zein nanofibre fabrication because smooth interconnected fibres were produced at that solution concentration and voltage. XRD confirmed the phase of zein crystallinity and FTIR successfully confirmed that functional groups present in zein nanofibres. The fabrication of collagen nanofibres was not successful due to insufficient sample that was expensive. Implementations of collagen preparations observations on **Table 3.1** indicates that collagen solutions electrosprayed.

Different blend weight ratios of zein/PVA were successfully prepared using the optimized conditions of zein nanofibres. The SEM illustrated that the fibre morphology of the different blend weight ratios improved and became uniform, which was attributed by the increase in PVA concentration. The effect of voltage played a significant role in the increment of average diameter, therefore, zein/PVA (80/20) was considered the blend weigh ratio with the highest fibre yield. The well-defined tubular like shape morphology of zein/PVA (80/20) fibre blend with high average diameter illustrated that there was higher charge density on the surface of the ejected jet solution during electrospinning. Therefore more electric charges were drawn to the electrospinning collect at a faster rate. Optical properties of zein/PVA fibre blends showed a peak at ~330 nm which was associated with the $n \rightarrow p^*$ transitions in carbonyl groups of carboxamide present in zein. That confirmed that all fibre blends contained chromophoric groups (C=O, C-N, C-C). The increment of PVA concentration also caused an increase in the conjugation length of the polymer chains that resulted in an increased wavelength. The XRD results showed that zein/PVA (80/20) fibre blend did not show any amorphous peak at $2\theta = 18.78^{o}$, that confirmed that the two polymers were partially miscible. The FTIR spectral analysis proved the presence of PVA in the electrospun zein/PVA fibre blend weight ratio. TGA confirmed that all zein/PVA fibre blends were thermally stable although the blend weight ratio decomposition stages of zein/PVA (80/20) occurred at a faster rate and the other blend weight ratio's decomposition stages were prolonged. Therefore the TGA and DTA results correlated to the SEM results obtained, which illustrated that the addition of PVA concentration had a significant impact on the thermal stability of the zein/PVA fibre blends.

Iron oxide nanoparticles were successfully synthesized by hydrothermal method and HMDA was used as the capping agent to assist in aggregation of the nanoparticles. The iron oxide nanoparticles were synthesized at different temperatures of 110℃ and 140℃. Manganese oxide nanoparticles were synthesized using co-precipitation method without addition of any capping agent. The manganese oxide nanoparticles were also prepared at different temperatures of 600℃ and 800℃. TEM results showed that iron oxide nanoparticles (α-Fe_2O_3) prepared at 140 ℃ were well defined nanocubes and also manganese oxide nanoparticles (α-Mn_2O_3) prepared at 800℃ showed rod-spherical shapes. Both iron and manganese oxide nanoparticles illustrated that the effect of temperature had an influence on the optical properties, morphology and size of the iron and manganese oxide nanoparticles.

The α-Fe_2O_3 and α-Mn_2O_3 nanoparticles were successfully incorporated into zein/PVA (80/20) fibre blends solutions. The SEM results of the different concentrations (4.25 wt%, 4.75 wt% and 5.25 wt%) embedded onto zein/PVA fibre blends showed that concentration played a vital role in the enhancement of the nanocomposite morphologies. XRD results illustrated that the intensity of the amorphous peak associated with zein/PVA fibre was influenced by the increment of the nanoparticle concentration although, the nanoparticles present in the nanocomposites attributed to small crystallite size, which was below the detection limit of XRD. The FTIR spectra of the nanocomposite fibres and composite fibre blends gave almost similar features. TGA curves showed an increase in the thermal stability of the zein/PVA fibres upon addition of the α-Fe_2O_3 and α-Mn_2O_3 nanoparticles. Therefore TGA results showed that the 5.25 wt% nanocomposites of α-Fe_2O_3/zein/PVA and α-Mn_2O_3 /zein/PVA were more thermally stable.

3.7.7. References

Abdelghany, A. M., Abdelrazek, E. M., & Elshahawy, A. (2015). FTIR and UV / Vis . Spectroscopy : A Key for Miscibility Investigation of PVC / PMMA Polymer Blend. *Middle East Journal of Applied Sciences*, 5(05), pp. 36–44

Abdelmajid Lassoued, Brahim Dkhil, Abdellatif Gadri, S. A. (2017). Control of the shape and size of iron oxide (α-Fe_2O_3) nanoparticles. *Results in Physics*, 7, pp. 3007-3015 doi:10.1016/j.rinp.2017.07.066

Aziz, S.B., Gh. Abdullah , O., Sarkawt , A., Hussein, S. A. and, & Ahmed, H. M. (2017). Effect of PVA Blending on Structural and Ion Transport Properties of CS : AgNt-Based Polymer.

Polymers, 9(622), pp. 1–17. doi:10.3390/polym9110622

Chatterjee, U., Jewrajka, S. K., & Guha, S. (2009). Dispersion of Functionalized Silver Nanoparticles in Polymer Matrices : Stability , Characterization , and Physical Properties. *Polymer Composites*, 30(6), pp. 827–834. doi:10.1002/pc.20655

Chen, L., Sun, L., Luan, F., Liang, Y., Li, Y., & Liu, X. (2010). Synthesis and pseudocapacitive studies of composite films of polyaniline and manganese oxide nanoparticles. *Journal of Power Sources*, 195(11), pp. 3742–3747. doi:10.1016/j.jpowsour.2009.12.036

Chen, X., Shen, Y., Suib, S. L., & Young, C. L. O. (2002). Characterization of Manganese Oxide Octahedral Molecular Sieve (M - OMS-2) Materials with Different Metal Cation Dopants. *Chemistry of Materials*, 14(2), pp. 940–948. doi:10.1021/cm000868o CCC:

Christopher J. Buchkoa, Loui C. Chen, Yu Shena, D. C. M. (1999). Processing and microstructural characterization of porous biocompatible protein polymer thin films. *Polymer*, 40, pp. 7397–7407.

Darezereshki, E. (2011). One-step synthesis of hematite (α -Fe_2O_3) nano-particles by direct thermal-decomposition of maghemite. *Materials Letters*, 65(4), pp. 642–645. doi:10.1016/j.matlet.2010.11.030

Deitzel, J. M., Kleinmeyer, J., Harris, D., & Tan, N. C. B. (2001). The effect of processing variables on the morphology of electrospun nanofibers and textiles. *Polymer*, 42, pp. 261–272.

Denkbaş, E. B., Çelik, E., Erdal, E., Kavaz, D., Akbal, Ö., Kara, G., & Bayram, C. (2016). Magnetically based nanocarriers in drug delivery. *Applications of Nanobiomaterials*. pp. 285-331. doi:10.1016/B978-0-323-42866-8.00009-5

Demangeat, E., Pédrot, M., Dia, A. , Bouhnik-le-Coz, M. , Grasset, F., Hanna, K., Kamagate, M.. and Cabello-Hurtado,F. (2018). Colloidal and chemical stabilities of iron oxide nanoparticles in aqueous solutions: the interplay of structural, chemical and environmental drivers. *Environmental Science: Nano*, 5, pp. 992–1001. doi:10.1039/C7EN01159H

Deshpande, V. D., Pawar, P., & Gokarna, V. (2013). Compatibility in Immiscible Poly (Vinyl Chloride)/ Poly (Styrene) Blends. *International Journal of Material Science (IJMSCI)*, 3(4), pp. 152–162. doi:10.14355/ijmsci.2013.0304.04

Dong, B., Arnoult, O., Smith, M. E., & Wnek, G. E. (2009). Electrospinning of collagen

nanofiber scaffolds from benign solvents. *Macromolecular Rapid Communications*, 30(7), pp. 539–542. doi:10.1002/marc.200800634

Fayaz, A. M., Balaji, K., Girilal, M., Yadav, R., Kalaichelvan, P. T., & Venketesan, R. (2010). Biogenic synthesis of silver nanoparticles and their synergistic effect with antibiotics : a study against gram-positive and gram-negative bacteria. *Nanomedicine: Nanotechnology, Biology, and Medicine*, 6(1), pp. 103–109. doi:10.1016/j.nano.2009.04.006

Gaob, M., & Shenb, J. (1996). Luminescence of coated a-Fe_2O_3. *Journal of Luminescence*, 67(67), pp. 345–348. doi:0022-2213995000167

Garg, K., Bowlin, G. L., Garg, K., & Bowlin, G. L. (2014). Electrospinning jets and nanofibrous structures. *Biomicrofluidics*, 5, 013403(2011), pp. 1–20. doi:10.1063/1.3567097

Ghalei, S., Asadi, H., & Ghalei, B. (2018). Zein nanoparticle-embedded electrospun PVA nanofibers as wound dressing for topical delivery of anti-inflammatory diclofenac. *Applied Polymer Science*, 135(33), pp. 1–11. doi:10.1002/app.46643

Ghelich, R., Rad, M. K., & Youzbashi, A. A. (2015). Study on Morphology and Size Distribution of Electrospun NiO-GDC Composite Nanofibers Effect of Polymer Concentration Solution. *Journal of Engineered Fibers and Fabrics*, 10(1), pp. 12–19.

Gilman, J. W., Vanderhart, D. L., & Kashiwagi, T. (1995). Thermal Decomposition Chemistry of Poly (vinyl alcohol). *ACS Symposium Series*, 599, pp. 161–185. doi:10.1021/bk-1995-0599.ch011

Gopinath, A., Murali, S., & Reddy, M. (2014). Effect of aqueous ethanol on the triple helical structure of collagen. *Eur Biophys J*, 43, pp. 643–652. doi:10.1007/s00249-014-0994-5

Hoque,M .A, Ahmed, M.R. , Rahman, G.T. , Rahman, M.T. , Islam, M.A. , Mubarak A., Khan, M. K. H. (2018). Fabrication and comparative study of magnetic Fe and α-Fe_2O_3 nanoparticles dispersed hybrid polymer (PVA+Chitosan) novel nanocomposite film. *Results in Physics*, 10, pp. 434–443. doi:10.1016/j.rinp.2018.06.010

Jacobs, V., Anandjiwala, R. D., & Maaza, M. (2010). The Influence of Electrospinning Parameters on the Structural Morphology and Diameter of Electrospun Nanofibers. *Applied Polymer Science*, 115, pp. 3130–3136. doi:10.1002/app.31396

Jiang, Y., Mo, H., & Yu, D. (2012). Electrospun drug-loaded core – sheath PVP / zein

nanofibers for biphasic drug release. *International Journal of Pharmaceutics*, 438(1–2), pp. 232–239. doi:10.1016/j.ijpharm.2012.08.053

Kai Wei, Hae-Rim Kim, B.-S. K. and I.-S. K. (2011). Electrospun Metallic Nanofibers Fabricated by Electrospinning and Metallization. *InTech*, pp. 117–134.

Kazanci, M. (2014). Solvent and temperature effects on folding of electrospun collagen nanofi bers. *Materials Letters*, 130, pp. 223–226. doi:10.1016/j.matlet.2014.05.114

Kim, S. H., Kim, S. J., & Oh, S. M. (1999). Preparation of Layered MnO_2 via Thermal Decomposition of KMnO 4 and Its Electrochemical Characterizations. *Chem. Mater*, 11(6), pp. 557–563.

Kiyoshi Terayama and Masao Ikeda. (1983). Study on Thermal Decomposition of MnO_2 and Mn_2O_3.pdf. *Transactions of the Japan Institute of Metals*, 11(1983),pp. 754–758.

Koysuren, O., Karaman, M., & Dinc, H. (2012). Preparation and Characterization of Polyvinyl Borate / Polyvinyl Alcohol (PVB / PVA) Blend Nanofibers. *Journal of Applied Polymer Science*, 124, pp. 2736–2741. doi:10.1002/app.35035

Kruger, K., Gordon, W. Æ., & Cooke, P. H. (2009). Compatible Blends of Zein and Polyvinylpyrrolidone. *J Polym Environ*, 17, pp. 115–122. doi:10.1007/s10924-009-0128-9

Kumar, M. (2018). Synthesis and Characterization of Mn / Polyaniline Nanocomposites via in situ approach. *International Journal of Advance Reseacrh in Science and Engineering*, 7(3), pp. 781–790.

Kun, D., & Pukánszky, B. (2017). Polymer/lignin blends: interactions, properties, applications. In *European Polymer Journal*, 9, pp. 618-641. doi:10.1016/j.eurpolymj.2017.04.035

Lassoued, A., Dkhil, B., Gadri, A., & Ammar, S. (2017). Control of the shape and size of iron oxide (α-Fe_2O_3) nanoparticles synthesized through the chemical precipitation method. *Results in Physics*, 7, pp. 3007–3015. doi:10.1016/j.rinp.2017.07.066

Lassoued, A., Lassoued, M. S., Dkhil, B., Ammar, S., & Gadri, A. (2018). Synthesis, photoluminescence and Magnetic properties of iron oxide (α-Fe_2O_3) nanoparticles through precipitation or hydrothermal methods. *Physica E: Low-Dimensional Systems and Nanostructures*, 101, pp. 212–219. doi:10.1016/j.physe.2018.04.009

Lin, M., Tng, L., Lim, T., Choo, M., Zhang, J., Tan, H. R., & Bai, S. (2014). Hydrothermal

synthesis of octadecahedral hematite (α-Fe_2O_3) nanoparticles:An Epitaxial Growth from Goethite (α-FeOOH). *Journal of Physical Chemistry C*, 118(20), pp. 10903–10910. doi:10.1021/jp502087h

Liu, N., Su, Y., Wang, Z., Wang, Z., Xia, J., & Chen, Y. (2017). Electrostatic Interaction-Assisted Construction of 3D Networks of Manganese Dioxide Nanosheets for Flexible High-Performance Solid-State Asymmetric Supercapacitors. *ACS Nano*, 11, pp. 7879−7888. doi:10.1021/acsnano.7b02344

Maliyekkal, S. M., Lisha, K. P., & Pradeep, T. (2010). A novel cellulose-manganese oxide hybrid material by in situ soft chemical synthesis and its application for the removal of Pb(II) from water. *Journal of Hazardous Materials*, 181(1–3), pp. 986–995. doi:10.1016/j.jhazmat.2010.05.112

Marta Valášková , Jonáš Tokarský , Jiˇrí Pavlovský, T. P. and K. K. (2019). α-Fe_2O_3 Nanoparticles/Vermiculite Clay Material: Structural, Optical and Photocatalytic Properties, *Materials*, 12(11), pp. 1–16. doi:10.3390/ma12111880

Matthews, J. A., Wnek, G. E., Simpson, D. G., & Bowlin, G. L. (2002). Electrospinning of Collagen Nanofibers. *Biomacromolecules*, 3, pp. 232–238. doi:10.1021/bm015533u

Miao, Y., & Yang, R. (2017). Poly(L-lysine) modified zein nanofibrous membranes as efficient scaffold for adhesion, proliferation, and differentiation of neural stem cells. *RSC Adv.*, 7, pp. 17711–17719. doi:10.1039/C7RA00189D

Miyoshi, T., Toyohara, K., & Minematsu, H. (2005). Preparation of ultrafine fibrous zein membranes via electrospinning. *Polym Int*, 54, pp. 1187–1190. doi:10.1002/pi.1829

Moloto, N., Moloto, M. J., Kalenga, M., Govindraju, S., & Airo, M. (2013). Synthesis and characterization of MnS and MnSe nanoparticles: Morphology, optical and magnetic properties. *Optical Materials*, 36(1), pp. 31–35. doi:10.1016/j.optmat.2013.06.023

Moloto, Nosipho, Coville, N. J., Sinha, S., & Moloto, M. J. (2009). Morphological and optical properties of MnS / polyvinylcarbazole hybrid composites. *Physica B: Physics of Condensed Matter*, 404(22), pp. 4461–4465. doi:10.1016/j.physb.2009.09.040

More, D. S., Moloto, M. J., Moloto, N., & Matabola, K. P. (2015). TOPO-capped silver selenide nanoparticles and their incorporation into polymer nanofibers using electrospinning

technique. *Materials Research Bulletin*, 65, pp. 14–22. doi:10.1016/j.materresbull.2015.01.030

Musi, S., & Santana, G. P. (1999). *Fe Mössbauer , FT-IR and TEM Observations of Oxide Phases Precipitated from Concentrated*. 72(3), pp. 87–102.

Najjar, R., & Abdel-gaber, R. A. A. M. (2018). Physical Properties of Mn 2 O 3 Nanoparticles Synthesized by Co-precipitation Method at Different pH Values. *Journal of Superconductivity and Novel Magnetism*, 32(4), pp. 885–892. doi:10.1007/s10948-018-4765-x

Nassar, M. Y., Amin, A. S., Ahmed, I. S., & Abdallah, S. (2016). Sphere-like Mn_2O_3 nanoparticles : Facile hydrothermal synthesis and adsorption properties. *Journal of the Taiwan Institute of Chemical Engineer*, *64*, pp. 79–88. doi:10.1016/j.jtice.2016.03.041

Olatunji, O. O., Akinlabi, S. A., Mashinini, M. P., Fatoba, S. O., & Ajayi, O. O. (2018). Thermo-gravimetric characterization of biomass properties: A review. *IOP Conference Series: Materials Science and Engineering*, 423(1). pp. 012175. doi:10.1088/1757-899X/423/1/012175

Oliveira, C. L. S. De, Almeida, N., Elvis, J., Henrique, L., Mattoso, C., Akira, F., Guimarães, A., Souza, A. De, Henrique, G., & Tonoli, D. (2014). Electrospinning of zein / tannin bio-nanofibers. *Industrial Crops & Products*, 52, 298–304. doi:10.1016/j.indcrop.2013.10.047

Portehault, D., Cassaignon, S., & Jolivet, J. (2009). Structural and morphological control of manganese oxide nanoparticles upon soft aqueous precipitation through MnO_4^- / Mn^{2+} reaction. *Journal of Materials Chemistry*, 19, pp. 2407–2416. doi:10.1039/b816348k

Qureshi, U. A., Khatri, Z., Ahmed, F., Khatri, M., & Kim, I. (2017). Electrospun Zein Nano fi ber as a Green and Recyclable Adsorbent for the Removal of Reactive Black 5 from the Aqueous Phase. *ACS Sustainable Chem. Eng*, 5, pp. 4340–4351. doi:10.1021/acssuschemeng.7b00402

Rajendran, S. G. V. (2011). Synthesis of CeO 2 or a – Mn 2 O 3 nanoparticles via sol – gel process and their optical properties. *J Sol-Gel Sci Technol*, 58, pp. 62–69. doi:10.1007/s10971-010-2356-9

Reitzenstein, N. H. Von, Bi, X., Yang, Y., Hristovski, K., & Westerhoff, P. (2016). Morphology , structure , and properties of metal oxide / polymer nanocomposite electrospun mats. *Applied Polymer Science*, 133(33), pp. 1–9. doi:10.1002/app.43811

Rejania P., Benna, B. (2013). Structural and Nanocomposite Optical Properties of Polyindole-Manganese Oxide Nanocomposite. *2*(3), pp. 244–248.

Sanfélix, S. G. (2016). *Manganese Oxide Nanoparticles : Synthesis and Magnetic Properties Erasmus Exchange* , Masters Theisis, Philipps Universitait Marburg .

Schwertmann, U., Friedl, J., & Stanjek, H. (1999). From Fe(III) ions to ferrihydrite and then to hematite. *Journal of Colloid and Interface Science*, 209(1), pp. 215–223. doi:10.1006/jcis.1998.5899

Senna. M, Salmieri. S,‡ Abdel-Wahab EL-Naggar, S. A., AND Monique Lacroix, Afrany, A. G. S., & Acroix, Mo. L. (2010). Improving the Compatibility of Zein / Poly (vinyl alcohol) Blends by Gamma Irradiation and Graft Copolymerization of Acrylic Acid. *Journal of Agricultural and Food Chemistry*, 58, pp. 4470–4476. doi:10.1021/jf904088y

Senthil, R. A., Theerthagiri, J., & Madhavan, J. (2015). Hematite Fe_2O_3 nanoparticles incorporated polyvinyl alcohol based polymer electrolytes for dye-sensitized solar cells. *Materials Science Forum*, 832, pp. 72–83. https://doi.org/10.4028/www.scientific.net/MSF.832.72

Singh, S. C., Swarnkar, R. K., & Gopal, R. (2009). Optical properties of Zinc Oxide/Polymer Nanocomposite. *NSTI-Nanotech*, 1, pp. 45–48.

Suhasini, A., Kumar, K. P. V., & Maiyalagan, T. (2018). Synthesis , thermal and magnetic behavior of iron oxide-polymer nanocomposites. *Science and Engineering of Composite Materials*, 25(1), pp. 189–195. doi:10.1515/secm-2015-0531

Swaroop K. and H.M. Somashekarappa. (2015). Effect of pH values on surface Morphology and Particle size variation in ZnO Nanoparticles Synthesised by co-precipitation Method Effect of pH values on surface Morphology and Particle size variation in ZnO Nanoparticles Synthesised by co-precipitation Me. *Research Journal of Recent Sciences*, 4((ISC-2014)), pp. 197–201.

Tillekeratne, M., & Easteal, A. J. (2000). Modification of zein films by incorporation of poly (ethylene glycol) s. *Polym Int*, 49, pp. 127–134.

Torres-giner, S., Gimenez, E., & Lagaron, J. M. (2008). Characterization of the morphology and thermal properties of Zein Prolamine nanostructures obtained by electrospinning. *Food*

Hydrocolloids 22, 22, pp. 601–614. doi:10.1016/j.foodhyd.2007.02.005

Wang, L., Omomo, Y., Sakai, N., Fukuda, K., Nakai, I., Ebina, Y., Takada, K., & Watanabe, M. (2003). Fabrication and Characterization of Multilayer Ultrathin Films of Exfoliated MnO2 Nanosheets and Polycations. *Chem. Mater*, 15, pp. 2873–2878. doi:10.1021/cm034191r

Wang, S., Min, Y., & Yu, S. (2007). Synthesis and Magnetic Properties of Uniform Hematite Nanocubes. *J. Phys. Chem. C*, 111(9), pp. 3551–3554. doi:10.1021/jp068647e

Yang, F., Xiong, S., Xia, Z., Liu, F., Han, C., & Zhang, D. (2012). Two-step synthesis of silver selenide semiconductor with a linear magnetoresistance effect. *Semiconductor Science and Technology*, 27(12), pp 125017. doi:10.1088/0268-1242/27/12/125017

Yao, C., Li, X., & Song, T. (2006). Electrospinning and Crosslinking of Zein Nanofiber Mats. *Journal of Applied Polymer Science*, 103(1), pp. 380–385. doi:10.1002/app.24619

Yu, P. W. (2016). Development of nanostructured materials based on manganese oxides and produced by an electrochemical method for water electrolysis. PhD Thesis, *Université Pierre et Marie Curie Chimie, Ed 388*.

Zhang, L., Xu, J., Tang, Y., & Hou, J. (2016). A novel long-lasting antifouling membrane modified with bifunctional capsaicin-mimic moieties via in situ polymerization for efficient water purificatio. *Journal of Materials Chemistry A: Materials for Energy and Sustainability*, 00,pp. 1–11. doi:10.1039/C6TA03205B

Zhang, M., Liu, Y., Yi, H., Luan, J., Zhang, Y., Cai, H., & Sun, D. (2014). The Journal of The Textile Institute Electrospun zein / PVA fibrous mats as three- dimensional surface for embryonic stem cell culture. *The Journal of The Textile Institute*, 105(3), pp. 246–255. doi:10.1080/00405000.2013.835902

Zhu, H. Y., Jiang, R., Xiao, L., & Li, W. (2010). A novel magnetically separable γ-Fe_2O_3/crosslinked chitosan adsorbent: Preparation, characterization and adsorption application for removal of hazardous azo dye. *Journal of Hazardous Materials*, 179(1–3), pp. 251–257. doi:10.1016/j.jhazmat.2010.02.087

CHAPTER 4

ADSORPTION STUDIES

Chrysoidine dye is an industrial azo dye that is cationic which is often characterized by the presence of the azo-group [N=N]. it is utilised to produce most clothing dyes and artificial industrial compounds (Michaels & Lewis 1986; Chung & Stevens 1993; Doh-Ura *et al.* 2007). Chrysoidine dye is also recognised as a cancer-causing agent that results in acute and persistent harm to mammals if it is consumed orally or administered to the skin (Reyns *et al.* 2010) (Bagheri *et al.*, 2015). Water-soluble azo dyes exhibit considerable resistance to biodegradation due to their complex structures, as well as high thermal and photo-stability. The presence of azo dyes into the environment especially in water streams and wastewater is a major concern as it is considered toxic, mutagenic and carcinogenic (Bagheri *et al.*, 2015; Hao *et al.*, 2019). Therefore, chrysoidine dye removal in an economical way is of high importance for the achievement of safe, clean media and ecosystems.

Adsorption is amongst various techniques that have been previously used to eliminate dye from wastewater. Comparing to other wastewater treatments, such as fugal decolorization, microbial degradation, flocculation, membrane separation, ion exchange, oxidation (Crini, 2006). Adsorption methods been extensively utilized because of its extraordinary effectiveness and capability making it a suitable method for large-scale applicability; it is less costly than other separation methods (Chakraborty *et al.* 2003;Lin *et al.* 2012). Adsorption has created opportunities for polymers and polymer nanocomposites enabled in wastewater treatment (Zhang et al., 2016). The adsorption of zein/PVA and its nanocomposite polymer fibre blends has been studied because the metal oxides (α-Fe_2O_3/ α-Mn_2O_3) enhanced the polymer properties. The higher affinity of the nanoparticles on the polymer fibre blends in water compared to the hydrophobic polymer alone enhanced the large surface area, increased the pore size and improved hydrophobicity (Arsuaga *et al.*, 2013). The results obtained in **chapter 4** illustrate that the chosen polymer and polymer nanocomposites had smooth morphology, significant presence of metal oxides (α-Fe_2O_3/ α-Mn_2O_3) embedded onto zein/PVA polymer blends, improved crystallinity and thermal stability. Therefore these properties were sufficient for the nanoadsorbents to remove chrysoidine dye from wastewater. Hence different adsorption

parameters such as effect of contact time, pH, initial concentration and adsorbent dosage, adsorption isotherms and kinetics were studied and the findings were reported below. **Table 4.1** shows the optimum electrospun materials chosen for the adsorption of chrysoidine G.

Table 4.1 Optimum electrospun polymer and nanocomposite fibre blends.

Polymer/ nanocomposite fibre blends	**Metal oxide nanoparticle concentrations**	**Blended solution ratio**
zein/PVA	0 wt%	80/20
α- Fe_2O_3/zein/PVA	5.25 wt%	80/20
α-Mn_2O_3/zein/PVA	5.25 wt%	80/20

4.1. Effect of contact time on the selected polymeric fibre materials

The study of the contact time is an important parameter since it can reflect the adsorption kinetics of an adsorbent for a given concentration of the adsorbate (Wang *et al.*, 2007). The influence of contact time on the adsorption capacity of zein/PVA, iron oxide nanoparticles and manganese oxide nanoparticles embedded onto zein/PVA polymer fibre blends are depicted in **Fig. 4-1.** It was observed that the adsorption efficiency of polymer composite and polymer nanocomposites for chrysoidine G dye increased with increasing adsorption time until equilibrium was reached.

Zein/PVA (composite) and α-Mn_2O_3/zein/PVA (nanocomposite) gave higher adsorption efficiency of 56.16 ± 4.5% and 54.75± 1.6% compared to α-Fe_2O_3/zein/PVA nanocomposite which had a lower adsorption efficiency of 53.81 ± 1.1%, this can be explained by the additional adsorbing sites that are provided by the oxygen atom of manganese oxide nanoparticles (K-OMS-2), the larger surface area and the numerous binding sites of zein/PVA nanofibre blends (Hakro *et al.*, 2018). The high calcination temperature of the prepared (K-OMS-2) nanoparticles embedded onto zein/PVA influenced the crystal size of the α-Mn_2O_3 nanoparticles (27.89 nm) could have also contributed into the high adsorption efficiency of the nanocomposite (Moriyama et al., 2014). It is observed that the adsorption efficiency of zein/PVA (composite) and α-Mn_2O_3/zein/PVA declines once saturation was reached at 30 min. This was due to saturation of adsorption sites and desorption of chrysoidine G (Wang et al., 2020). It was observed that α-Fe_2O_3/zein/PVA nanocomposite prolong to reach saturation this is due to active sites on the adsorbent functional groups until plateau was reached (Hao *et al.*,

2019). The adsorbents that were embedded with nanoparticles enhanced uniform particle dispersion which increased the surface area. The adsorbents also continued to show adsorption efficiency higher than 48% at constant equilibrium as compared to zein/PVA alone. This was due to the hydroxyl groups from PVA surrounding the nanoparticles (Guo *et al.*, 2010), that are responsible for the strong interaction between the metal oxide nanoparticles (α-Fe_2O_3/ α-Mn_2O_3) and the composite fibre blends (zein/PVA). According to literature the relation between the nature of the polymer composites, nanocomposites and adsorption rate is generally complicated by many possible interactions on the surface (Arslan & Yig, 2007). Generally, the electrostatic interaction, surface binding and chemical reaction may be identified as the major adsorption mechanisms (Arslan & Yig, 2007). The results obtained from this study also indicates that chrysoidine G dye was removed in the first 30 minutes until equilibrium was reached, the rapid rate within 30 minutes was due to the availability of active sites on the adsorbents for the chrysoidine G ions in the solution. Therefore 120 minutes was set to be sufficient time for adsorption experiments due to the active binding sites that already occupied the dye molecules.

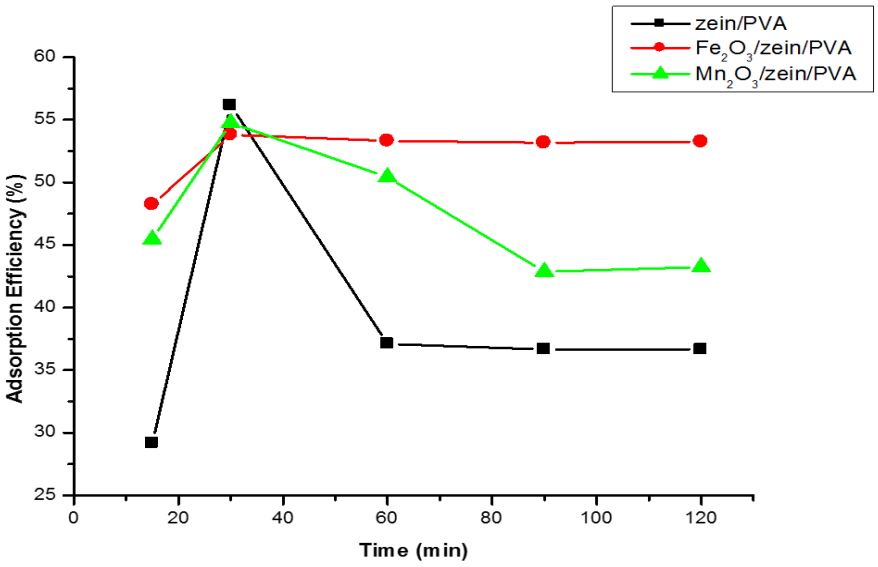

Fig. 4-1 Effect of contact time on the removal of Chrysoidine G by zein/PVA, α-Fe_2O_3/zein/PVA and α-Mn_2O_3/zein/PVA nanocomposites (conditions-concentration of dye: 100 mg.L^{-1}; adsorbent dosage: 0.002 g/L; pH 8 of working solution and 25℃ temperature).

4.2. Adsorption Kinetics on the selected polymeric fibre materials

Adsorption kinetics models deals with changes in chemical properties in time and is concerned especially with rates of changes. Typically adsorption equilibria are not reached instantaneously due to the fact that the mass transfer from the solution to the adsorption sites within the adsorbent particles is constrained by the mass transfer resistance which determines the time required to reach equilibrium (Worch, 2012). Therefore the progress of adsorption is referred to as adsorption kinetics. The adsorption kinetic models were applied to interpret the experimental data to determine the controlling mechanism of chrysoidine G adsorptions from aqueous solution. Here, pseudo-first-order (PFO) and pseudo-second-order model (PSO) were used to test the experimental data. The effect of time was studied (**Fig.4-1**) for chrysoidine G adsorption which showed that the efficiency increased with increasing contact time. All data were fitted to both the pseudo-first (**Equation 9 on page 50**) and pseudo-second order (**Equation 10 on page 50**) equations. **Fig. 4-2** illustrates the pseudo first order and second order graphs of zein/PVA**,** α -Fe_2O_3/zein/PVA and Mn_2O_3/zein/PVA nanoadsorbent. **Table 4.2** gives information about the kinetic parameters the nanoadsorbents followed. It was observed from the fitted data that the adsorption of chrysoidine G that the experimental adsorption capacities of the three nanoadsorbents had a similar trend with the adsorption capacity of the pseudo first-order model. However, all nanoadsorbents had a very poor correlation coefficient (r^2) for pseudo first order.

The α-Mn_2O_3/zein/PVA and α -Fe_2O_3/zein/PVA nanoadsorbent materials had high K_2 values and higher experimental adsorption capacities compared to zein/PVA nanofibre blends this was contributed by the embedded nanoparticles which increased the surface area of the adsorbents (Vincent *et al.*, 2014). The was no similar trend observed with the experimental adsorption capacities of the nanoadsorbents with the adsorption capacity of pseudo second order although all three materials possessed a high correlation coefficient (r^2) for pseudo second order. Although the α -Mn_2O_3/zein/PVA nanoadsorbent possessed low correlation coefficient and high statistical standard error, resulting in poor pseudo second order fit compared to the other two nanoadsorbent materials. All three adsorbent materials obeyed the pseudo second order rate. The pseudo second order reaction occurred through chemisorption mechanism, which indicated that the adsorbate and the adsorbent interacted with each other through some form of chemical reactions (Hao *et al.*, 2019). Therefore these results correspond to previous studies conducted (Purkait *et al.*, 2004 ;Wen *et al.*, 2016).

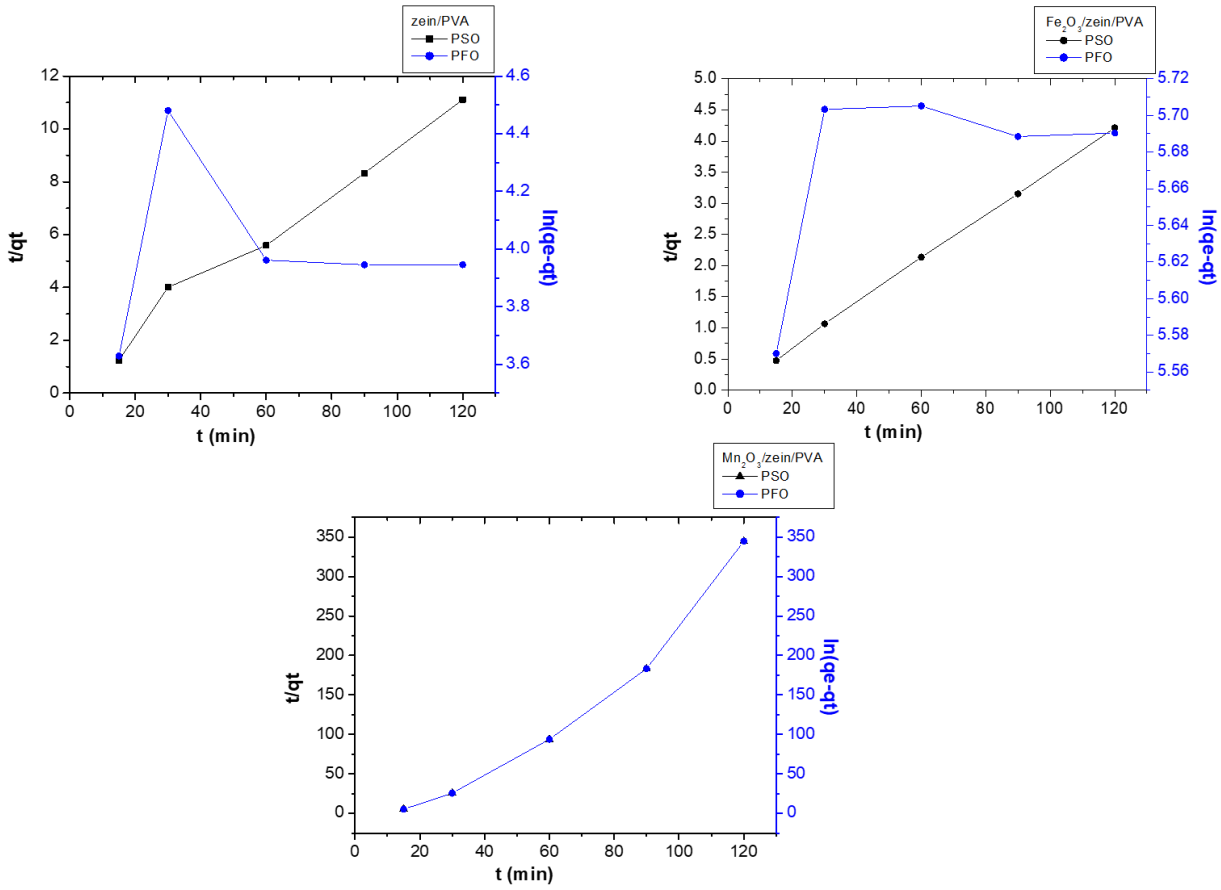

Fig. 4.2 PFO and PSO plots for the adsorption of chrysoidine G onto zein/PVA**,** α -Fe_2O_3/zein/PVA and Mn_2O_3/zein/PVA nanoadsorbents.

Table 4.2: Kinetic parameters of pseudo-first and pseudo-second orders for chrysoidine G by zein/PVA, α -Fe_2O_3/zein/PVA and α -Mn_2O_3/zein/PVA.

		zein/PVA	Fe_2O_3/zein/PVA	Mn_2O_3/zein/PVA
Pseudo first order	q_e (mg/g)	95.75	328	423.5
	q_m (mg/g)	55.36	277.67	354.54
	K_1 (min^{-1})	0.0003	0.0007	0.0012
	R^2	0.0023	0.3075	0.1965
	SSE	0.35	0.055	0.12
Pseudo second order	q_e (mg/g)	95.75	328	423.5
	q_m (mg/g)	11.36	28.33	0.01
	K_2 (g/mg/min)	0.02	0.07	0.1464
	R^2	0.9804	0.9998	0.9522
	SSE	0.61	0.032	34.93

4.3. Effect of pH on the selected polymeric fibre materials

The pH of a solution is an important parameter when assessing the adsorption of chrysoidine G dye onto suspended adsorbents. Initial pH of adsorption has a vital role in adsorption of sorbate (chrysoidine G) as it affects surface morphology of the sorbent (polymeric fibre materials) and binding nature of the sorbate (Batool *et al.*, 2018). Proteins such as zein are sensitive to pH changes of aqueous solutions therefore incorporation with synthetic polymers such as PVA was necessary to improve the performance of the adsorbent for the removal of azo dyes in aqueous media or water (Qureshi *et al.*, 2017). The embedment of nanoparticles is also considered critical in the enhancement and functionalization of the composed adsorbent (Zhua *et al.*, 2010). The presence of versatile functional groups including O-H, –C=O and amide groups permits simple and efficient loading of nanoparticles onto the surface of zein/PVA fibre blends. Therefore this combination synergically improves the adsorption capacity and applicability for the rapid removal of dyes (Bagheri *et al.*, 2015). According to literature zein exhibits zero zeta (ζ) potential at pH 6, therefore zeta potential of the nanoadsorbent materials was not conducted in this study (Xu *et al.*, 2013; Qureshi *et al.*, 2017).

The adsorption of chrysoidine G dye onto zein/PVA nanofibre blends, α-Fe_2O_3/zein/PVA and α-Mn_2O_3/zein/PVA nanocomposite fibre blends was studied at different pH to determine the optimum pH for maximum adsorption as shown in **Fig. 4-3**. It was found that the maximum adsorption of chrysoidine G occurred at pH 6.0 due to the magnitudes of electrostatic charges imparted by the ionized dye molecules which are primarily controlled by the pH of the medium (Matheswaran & Karunanithi, 2007). The maximum pH 6.0 of zein/PVA may also be due to the fact that zein/PVA has strong affinity towards cations owing to the electrostatic interaction between the positively charged ions of metal oxide nanoparticles and the lone pairs of zein/PVA. Therefore, the presence of the positively charged nitrogen atoms on zein/PVA is responsible for the adsorption of chrysoidine dye. The hydroxyl groups on zein/PVA also have interfacial interaction with the metal oxides nanoparticles which improved hydrophilicity and adsorption efficiency at acidic pH. The basic pH restricted the uptake of chrysoidine G onto the three adsorbents as the basic pH would have deprotonated both amino and carboxyl groups, thereby increasing the net negative charge on adsorbents (Qureshi *et al.*, 2017). As a result, electrostatic repulsion between dye molecular ions and adsorbents would have occurred within the pH range of 8−12. The α-Mn_2O_3/zein/PVA nanocomposite had the highest adsorption efficiency for the removal of the dye at pH 6.0 this was influenced by the phase stability of α-Mn_2O_3 nanoparticles embedded onto zein/PVA fibre blend compared to those of α-Fe_20_3

/zein/PVA nanocomposite and the zein/PVA fibre blend alone. The high calcination temperature of the prepared α-Mn_2O_3 nanoparticles embedded onto zein/PVA fibre blend might have contributed to the high adsorption efficiency of α-Mn_2O_3/zein/PVA nanocomposite.

It was also observed that as the pH increased the adsorption efficiency decreased. This was due to the competition of binding sites by hydroxyl ions from NaOH which was used for adjusting the pH. Therefore pH 6.0 was considered as the optimum pH for the adsorption of chrysoidine G and therefore rest of the studies were carried out at this pH. Bagheri et al. (2015) reported on the adsorption of chrysoidine using CuS-NP-AC. It was reported that the maximum percentage of the removal of chrysoidine G occurred at pH 6.0. It was further reported that the increase of pH from 2.0 to 6.0 improved the removal percentage from 84 to 90%. Wen et al. (2016) conducted a study on electrospun zein nanoribbons for treatment of lead-contained wastewater and observed that when the pH value of the initial solution changed from 7.0 to 5.0, 3.0, and 1.0. The adsorption efficiency correspondingly decreased from 86.7% to 57.1%, 46.3%, and 32.6% .Therefore the maximum pH trend of chrysoidine adsorption and zein nanofibres as the adsorbent material previously conducted by other research studies correspond to the obtained acidic pH results of this study.

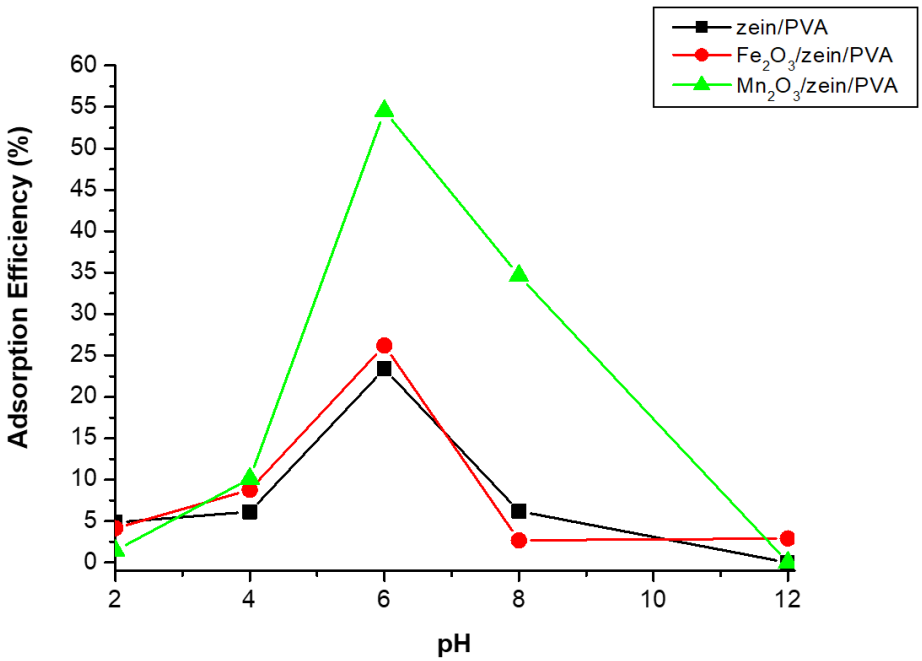

Fig. 4-3 Effect of pH on chrysoidine G uptake by zein/PVA nanofibre blends, α-Fe_20_3 /zein/PVA and α-Mn_2O_3/zein/PVA nanocomposites (conditions-concentration of dye: 100 $mg.L^{-1}$; adsorbent dosage: 0.002 g/L; contact time 120 min and 25℃ temperature).

4.4. Effect of initial concentration on the selected polymeric fibre materials

Adsorption is greatly influenced by the concentration of the analyte. The initial concentration of the adsorbate is important to study as it affects the adsorption phenomenon. The adsorption of chrysoidine G on the adsorbent surface of zein/PVA, α-Fe_2O_3/zein/PVA and α-Mn_2O_3/zein/PVA was studied at different initial concentration ranging from 20-100 mg/L at constant temperature, nanofibre mass and optimum conditions of time and pH. In **Fig. 4-4** it was observed that the maximum adsorption capacities of the nanoadsorbents were 159, 25 mg/g (zein/PVA), 366, 5 mg/g (α-Fe_2O_3/zein/PVA) and 349, 5 mg/g (α-Mn_2O_3/zein/PVA). It was observed that the level of adsorption for chrysoidine G on zein/PVA fibre blends slowly decreased from 70 mg/L to 100 mg/L when the initial concentration was further increased to 100 mg/L. This behavior may be attributed to the finite number of identical sites on zein/PVA fibre blends that were in the possession of adsorbed chrysoidine G molecules, consequently leading to the reduction in adsorption efficiency (Babitha & Korrapati, 2015; Qureshi et al., 2017). Zein/PVA had lower adsorption capacity at lower concentrations this might be due to unsaturation of active sites (Liu, 2015). However, zein/PVA fibre blends had the highest adsorption efficiency of 71% compared to α-Fe_2O_3/zein/PVA and α-Mn_2O_3/zein/PVA nanoadsorbent. It was also observed that the adsorption efficiency of α-Fe_2O_3/zein/PVA increased with increasing concentration and lower adsorption efficiency of 43% compared to zein/PVA. It was noticed that the adsorption capacity followed the same trend, although α-Fe_2O_3/zein/PVA had higher adsorption capacity at 80 ppm compared to α-Mn_2O_3/zein/PVA and zein/PVA. This was attributed by the mass transfer interactions between chrysoidine G and α-Fe_2O_3/zein/PVA nanoadsorbent. This meant that higher concentrations resulted in an increase in concentration gradient. That led to a higher probability of collision among chrysoidine G ions and the active sites on α-Fe_2O_3/zein/PVA adsorbent thereby increasing the adsorption capacity (Tanhaei et al., 2015; Bagheri et al., 2015). Therefore saturation was reached due to exhaustion of all the active sites. It was further observed that the adsorption efficiency of chrysoidine G onto α-Mn_2O_3/zein/PVA nanoadsorbent decreased from 20 mg/L to 40 mg/L and a further decrease was observed from 80 mg/L to 100 mg/L. This was due to the fact that the number of chrysoidine G dye molecules had higher affinity than the number of surface sites available on the α-Mn_2O_3/zein/PVA nanoadsorbent (Nassar et al., 2016). After a lapse of time plateau is reached due to saturation (Wang et al., 2020) and due to complete occupation of repulsive forces between chrysoidine G adsorbed on the surface of α-

Mn_2O_3/zein/PVA (Hakro et al., 2018; Wang et al., 2012). The α-Mn_2O_3/zein/PVA nanoadsorbent had a higher adsorption capacity at high concentration of 60 ppm compared to zein/PVA and a low adsorption efficiency of 42% compared to zein/PVA and α-Fe_2O_3/zein/PVA. This was attributed by the maximum concentration of chrysoidine G ions that are fully occupied onto the surface of α-Mn_2O_3/zein/PVA nanoadsorbent that also contained unsaturated active sites that contributed to the difference in the saturation of the different nanoadsorbent material (Liu, 2015). The α-Fe_2O_3/zein/PVA and α-Mn_2O_3/zein/PVA nanoadsorbents had higher adsorption capacities than zein/PVA this might be due to the high electrostatic attraction between the chrysoidine dye molecules and the nanocomposite surface due to embedded nanoparticles present on zein/PVA (Iram et al., 2010; Nassar et al., 2016). According to literature (Zhu et al., 2010) nanoparticles embedded onto polymeric materials expand adsorption capacity due increased surface area that enhances electrostatic interaction. Therefore the presence of metal oxides embedded onto polymer composite had an influence into the adsorption efficiency and adsorption capacity of the nanoadsorbent.

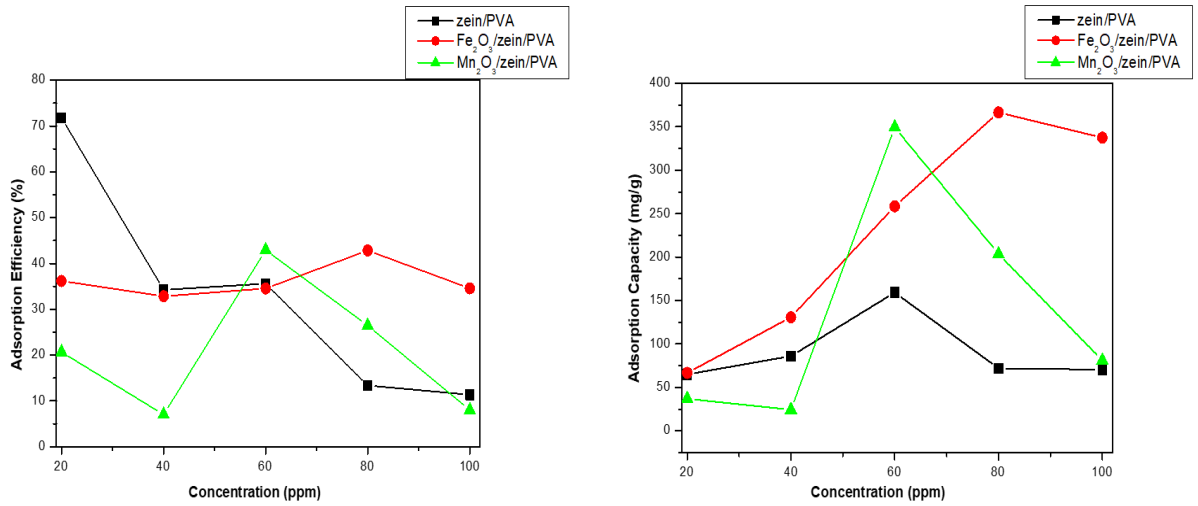

Fig. 4-4 Effect of initial chrysoidine G concentration on zein/PVA nanofibre blends, α-Fe_2O_3 /zein/PVA and α-Mn_2O_3/zein/PVA nanocomposites (adsorbent dosage: 0.002 g/L; contact time 120 min; pH 6 and 25℃ temperature).

4.5. Adsorption Isotherms on the selected polymeric fibre materials

The purpose of the adsorption isotherms is to correlate the adsorbate concentration in the solution and the adsorbed dosage of the dye at the adsorbate–adsorbent interface. There are several well-known adsorption models widely applied to study mechanisms for most heterogeneous adsorbent materials, which include Langmuir adsorption isotherms, Freundlich

adsorption isotherms, and Temkin adsorption isotherms (Zhou *et al.*, 1998; Ayawei *et al.*, 2017). Temkin adsorption, Dubinin-Radushkevich and other isotherms are temperature dependent whilst temperature was not explored in this study. Among these models, the Langmuir and Freundlich adsorption isotherms have the greatest general utility for azo-dye removal application. In the present study, the adsorption of chrysoidine G onto the three adsorbents was studied using Langmuir (**Fig. 4-5**) and Freundlich isotherms (**Fig. 4-6**). **Table 4.3** gives information about the type of isotherm and parameters the nanoadsorbents follow that is essential in order to understand the mechanisms between the adsorbate and adsorbents. It was found that 1/n value of Freundlich isotherm was greater than zero ($0 < 1/n<1$) indicating that the adsorption was favourable. The n value was also greater than 1 indicating that the surface of three nanoadsorbents was also more likely to be heterogeneous and adsorption was great at higher concentration of chrysoidine G. Although the low correlation coefficients (r^2) of the Freundlich model indicated that this model was unfavourable for the three adsorbents (Igwe & Abia, 2007). Hence the correlation coefficients (r^2) for the present chrysoidine G-nanoadsorbents system is explained better by the Langmuir isotherm. All three nanoadsorbents showed a best fit for different Langmuir isotherms equations.

Fig. 4-5 illustrates the Langmuir best fit for zein/PVA (**Equation 4 on page 49),** α-Fe_2O_3 /zein/PVA (**Equation 5 on page 49**) and α-Mn_2O_3/zein/PVA (**Equation 6 on page 49**). The adsorption capacity followed an order of α-Fe_2O_3 /zein/PVA >zein/PVA > α-Mn_2O_3/zein/PVA for chrysoidine G which indicated that there was stronger carbonyl, hydroxyl and amino groups interaction on α-Fe_2O_3 /zein/PVA with chrysoidine G which enhanced the adsorption performance compared to the other adsorbents. Therefore, these results confirm that an increase in adsorption capacity explains the interaction between the surfaces of adsorbents and chrysoidine G is taking place at a monolayer due to chemisorption (Zhu et al., 2010). The α-Fe_2O_3 /zein/PVA nanoadsorbent had higher correlation coefficients for both Langmuir (R^2 = 0.9824) and Freundlich (R^2 = 0.9485) isotherm models compared to the other two nanoadsorbents indicating that α-Fe_2O_3 /zein/PVA was a homogeneous and heterogeneous adsorbent although due to Langmuir isotherm having a correlation coefficient close to unity, the material was best fitted by Langmuir. Therefore, α-Fe_2O_3 /zein/PVA was an effective adsorbent for the uptake of chrysoidine G. In addition, the statistical standard error term was lower in the Langmuir isotherm model, indicating less error in fitting. The pseudo second order correlation coefficients of all three nanoadsorbent materials were higher than the Langmuir

correlation coefficients. The obtained results also agreed with the experimental adsorption capacities being higher than the calculated equilibrium adsorption capacities of the adsorbent materials. Zhua et al. (2010) conducted a study on a novel magnetically separable γ-Fe_2O_3/crosslinked chitosan adsorbent for removal of hazardous azo dye. It was reported that γ-Fe_2O_3/crosslinked chitosan had higher adsorption capacity and correlation coefficient (R^2 = 0.998) compared to chitosan alone (R^2 = 0.991). Therefore results obtained from this study corresponds to research studies previously conducted on the adsorption of chrysoidine using different adsorbent materials (Matheswaran & Karunanithi, 2007; Waqar et al., 2019).

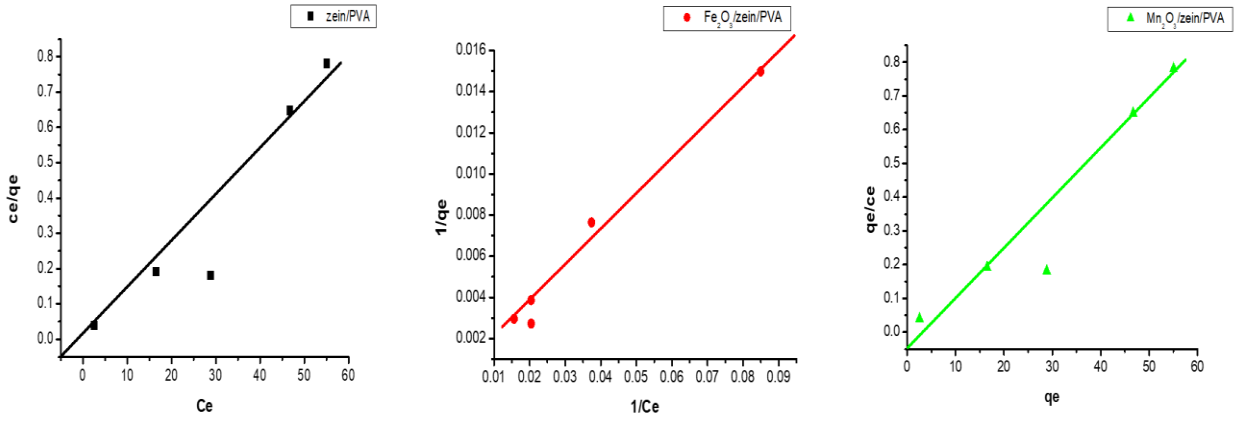

Fig. 4-5 Langmuir isotherm plots for zein/PVA nanofibre blends, α-Fe_2O_3 /zein/PVA and α-Mn_2O_3/zein/PVA nanocomposites (adsorbent dosage: 0.002 g/L; contact time 120 min; pH 6 and 25℃ temperature).

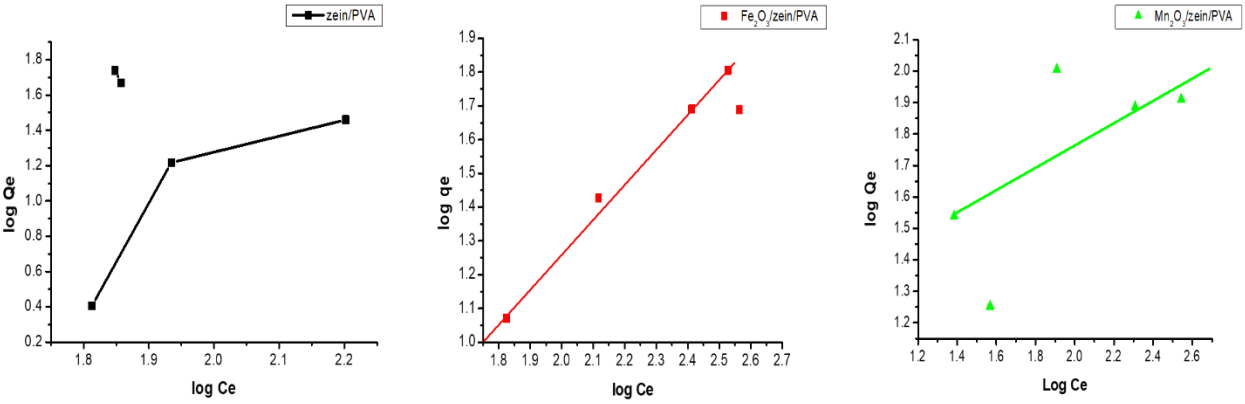

Fig. 4-6 Freundlich isotherm plots for zein/PVA nanofibre blends, α-Fe_2O_3 /zein/PVA and α-Mn_2O_3/zein/PVA nanocomposites (adsorbent dosage: 0.002 g/L; contact time 120 min; pH 6 and 25℃ temperature).

Table 4.3: Parameters of different isotherms of adsorption of chrysoidine G.

Modelling (Linear)	**Parameters**	**zein/PVA**	**Fe_2O_3/zein/PVA**	**Mn_2O_3/zein/PVA**
Langmuir 1	q_e (mg/g)	159.25	366.50	349.50
	q_m (mg/g)	68.98	-500	-192.31
	K_L (L/mg)	0.2255	-0.0017	0.0130
	R^2	0.9102	0.0214	0.0815
	SSE	0.1125	0,0310	0,6020
Langmuir 2	q_m (mg/g)	89.29	151.46	142.85
	K_L (L/mg)	1.12	0.0056	0.0197
	R^2	0.2001	0.9824	0.2652
	SSE	0,0037	0.0007	0,0202
Langmuir 3	qm (mg/g)	12.968	4.7842	24.88
	KL (L/mg)	-17.54	250	0.0187
	R^2	0.049	0.2612	0.8660
	SSE	44,1150	128,91	1.1678
Langmuir 4	qm (mg/g)	113.06	-2.1295	46.246
	KL (L/mg)	-0.8603	64.569	-0.0624
	R^2	0.049	0.2612	0.866
	SSE	11,3513	1,020	1,1679
Freundlich	K_f (mg/g)	2.20	3.62	6.50
	n	1.1757	1.092	2.1459
	1/n	0.8505	0.9157	0.4660
	R^2	0.0621	0.9485	0.5192
	SSE	0.1765	0.0821	0.3896

Table 4.4: Comparison adsorption capacities and operational parameters of chrysoidine onto various adsorbents.

Adsorbent	time (min)	pH	adsorption capacity (mg/g) or (**µg/g**)	Dosage (g/L)	References
zein/PVA	30	6	68.98	0.002	This study
α-Fe_2O_3/zein/PVA	30	6	151.64	0.002	This study
α-Mn_2O_3/zein/PVA	30	6	24.88	0.002	This study
γ-Fe_2O_3/crosslinked chitosan adsorbent	150	6.6	20.12	1.0	(Zhu *et al.*, 2010)
GO	30	7	680.3	5.0	(Hao *et al.*, 2019)
Fe_3O_4	30	7	63.94	5.0	(Hao *et al.*, 2019)
GO–Fe_3O_4	30	7	359.71	5.0	(Hao *et al.*, 2019)
Bottom ash	180	3	18.08	0.5	(Mittal *et al.*, 2010)
De-oiled soy	180	3	8.33	0.5	(Mittal *et al.*, 2010)
Copper sulfide nanoparticles loaded on activated carbon	360 s	6	89.3	0.03	(Bagheri *et al.*, 2015)

The adsorption capacities of various materials are displayed in **Table 4.4**. A direct comparison is practically impossible due to different adsorbent materials. The diverse adsorbent preparation methods and optimum experimental conditions used. The adsorption capacities values reported in **Table 4.4** in this study were promising and higher than some in literature. Zein/PVA possessed a higher adsorption capacity of 68.98 mg/g although a direct comparison with literature is impossible. The γ-Fe_2O_3/crosslinked chitosan adsorbent had a comparable q_m value from literature it was 20.12 mg/g and in this study the maximum adsorption capacity of α-Fe_2O_3/zein/PVA nanocomposite was 151.64 mg/g although a direct comparison is limited due to different iron oxide phases and polymers. The α-Mn_2O_3/zein/PVA nanocomposite also possessed high adsorption capacity of 24.88 mg/g which is impossible to compare directly with literature. The nanoadsorbent materials utilized in this study and in previous reported studies as indicated in the **Table 4.4** obtained maximum adsorption under acidic conditions.

4.6. Conclusions

The batch adsorption studies on the effect of contact time, pH and initial concentration were investigated. It was observed that the adsorption efficiency of zein/PVA fibre blends and polymer nanocomposites for chrysoidine G dye increased with increasing adsorption time until equilibrium was reached. The dye adsorption equilibrium was attained at 30 minutes for all three nanoadsorbent materials. The kinetic processes indicated that all three nanoadsorbents followed the pseudo second-order kinetics implying a chemisorption type process for all materials. The pH that was favourable for chrysoidine G adsorption was obtained at pH 6. This illustrated that acidic pH facilitated complete removal of chrysoidine G dye because an acidic pH tended to protonate the amine, carbonyl and hydroxyl groups present in the composite fibres and nanocomposites, promoting electrostatic interactions between the nanoadsorbents and the dye. The maximum adsorption capacities of the nanoadsorbents were 159, 25 mg/g (zein/PVA), 366, 5 mg/g (α-Fe_2O_3/zein/PVA) and 349, 5 mg/g (α-Mn_2O_3/zein/PVA). It was observed that the nanocomposites had higher adsorption capacities compared to the composite fibres. This was attributed by the presence of nanoparticles with different functional groups and charges on the composite surface which led to improved electrostatic forces. The isotherm models such as Langmuir and Freundlich were evaluated. It was shown that the equilibrium data were best described by the Langmuir model due to higher correlation coefficient values and the maximum adsorption capacities suggesting that adsorption of chrysoidine G occurred on a homogeneous surface by monolayer adsorption. The obtained results indicated that the α-Fe_2O_3/zein/PVA nanoadsorbent can be used as a suitable and efficient adsorbent in the removal of Chrysoidine G from wastewater

4.7. References

Al-Ghouti, M. A., & Da'ana, D. A. (2020). Guidelines for the use and interpretation of adsorption isotherm models: A review. *Journal of Hazardous Materials, 393,* pp. 122383. doi:10.1016/j.jhazmat.2020.122383

Blanchard, G., Maunaye, M. and Martin, G. (1984). Removal of heavy metals from waters by means of natural zeolites. *Water Research,* 18(12), pp. 1501–1507.

Chowdhury, S., Misra, R., Kushwaha, P., & Das, P. (2011). Optimum sorption isotherm by

linear and nonlinear methods for safranin onto alkali-treated rice husk. *Bioremediation Journal*, *15*(2), pp. 77–89. doi:10.1080/10889868.2011.570282

Fierro, V., Torne´-Ferna´ndez, V., , D. Montane´, A. C. (2008). Adsorption of phenol onto activated carbons having different textural and surface properties. *Microporous and Mesoporous Materials*, 111, pp. 276–284. doi: 10.1016/j.micromeso.2007.08.002.

Ghobadi, N. (2013). Band gap determination using absorption spectrum fitting procedure. *International Nano Letters*, *3*(2), pp. 2–5.

Jubu, P. R., Yam, F. K., Igba, V. M., & Beh, K. P. (2020). Tauc plot scale and extrapolation effect on bandgap estimation from UV – vis – NIR data – A case study of β -Ga_2O_3. *Journal of Solid State Chemistry*, *290*, pp. 121576. doi:10.1016/j.jssc.2020.121576

Kazanci, M. (2014). Solvent and temperature effects on folding of electrospun collagen nanofibers. *Materials Letters*. Elsevier, 130, pp. 223–226. doi: 10.1016/j.matlet.2014.05.114.

Lin, J., Li, C., Zhao, YI., Hu , J., and Zhange, Li. (2012). Co-electrospun Nanofibrous Membranes of Collagen and Zein for Wound Healing. *ACS Appl. Mater. Interfaces*, 4, pp. 1050-1057. doi.org/10.1021/am201669z

Liu, S. (2015). Cooperative adsorption on solid surfaces. *Journal of Colloid and Interface Science*, 450, pp. 224–238. doi:10.1016/j.jcis.2015.03.013

Moriyama, S., Sasaki, K., & Hirajima, T. (2014). Effect of calcination temperature on Mg-Al bimetallic oxides as sorbents for the removal of F- in aqueous solutions. *Chemosphere*, 95, pp. 597–603. doi:10.1016/j.chemosphere.2013.10.018

Proctor, A., & Toro-Vazquez, J. F. (2009). The Freundlich Isotherm in Studying Adsorption in Oil Processing. In *Bleaching and Purifying Fats and Oils: Theory and Practice* , 2, pp. 201-219 7. doi:10.1016/B978-1-893997-91-2.50016-X

Purkait, M. K., Gusain, D. S., DasGupta, S., & De, S. (2004b). Adsorption behavior of chrysoidine dye on activated charcoal and its regeneration characteristics by using different surfactants. *Separation Science and Technology*, *39*(10), pp. 2419–2440. doi:10.1081/SS-120039347

Qureshi, U. A., Khatri, Z., Ahmed, F., Khatri,M. and Kim, I. (2017). Electrospun Zein Nano fibre as a Green and Recyclable Adsorbent for the Removal of Reactive Black 5 from the

Aqueous Phase. *ACS Sustainable Chem. Eng.*, 5, pp. 4340-4351. doi: 10.1021/acssuschemeng.7b00402.

Sahin, R., & Tapadia, K. (2015). Comparison of linear and non-linear models for the adsorption of fluoride onto geo-material: Limonite. *Water Science and Technology*, *72*(12), pp. 2262–2269. doi:10.2166/wst.2015.449

Selling, G. W., Biswas, A., Patel, A., Walls, D.J., Dunlap, C., Wei, Y. (2007). Impact of Solvent on Electrospinning of Zein and Analysis of Resulting Fibres. *Macromolecular Chemistry and Physics*, 208, pp. 1002–1010. doi: 10.1002/macp.200700056

Tanhaei, B., Ayati, A., Lahtinen, M., & Sillanpää, M. (2015). Preparation and characterization of a novel chitosan/Al_2O_3/magnetite nanoparticles composite adsorbent for kinetic, thermodynamic and isotherm studies of Methyl Orange adsorption. *Chemical Engineering Journal*, 259, pp. 1–10. doi:10.1016/j.cej.2014.07.109

Zanatta, A. R. (2019). Revisiting the optical bandgap of semiconductors and the proposal of a unified methodology to its determination. *Scientific Reports*, *9*(1), pp. 11225. doi:10.1038/s41598-019-47670-y

Zhang, M, Liu Y., Yi., H., Luan, J., Zhang, Y., Cai, H., and Sun, D. (2014). Electrospun zein / PVA fibrous mats as three- dimensional surface for embryonic stem cell culture. *The Journal of The Textile Institute*, 105(3), pp. 246–255. doi: 10.1080/00405000.2013.835902.

CHAPTER 5

SUMMARY AND RECOMMENDATIONS

5.1. Summary

Zein nanofibres were successfully fabricated with no beads present using electrospinning technique. The prepared polymer fibres were found to be affected by the solution concentration and applied voltage. The SEM results showed that an increase in zein concentration resulted in more uniform fibres with increased average diameters. It was also observed that increasing the applied voltage resulted in decreased average diameters and ribbon-like amorphous nanofibre morphology. Therefore, the highest yield of zein nanofibres was obtained 25 wt% and 25 kV. The XRD patterns indicated that zein nanofibres were amorphous. The FTIR spectra confirmed the functional groups of zein nanofibres were present and were of α-helices. Optimisation preparations of collagen were unsuccessful due to the insufficient sample, which resulted in low concentration of sample preparation which favoured electrospraying instead of electrospinning.

Zein/PVA fibre blends were successfully fabricated using the electrospinning technique. The addition of PVA increased electrospinnabilty and improved fibre formation. The zein (80/20) fibre blends weight ratio had higher fibre yield due higher charge density that contributed to rapid rate of fibre formation. It was also observed that voltage had an influence on the morphology of the fibre blends. The optical properties showed that the polymer fibre blends were immiscible except for the zein/PVA (80/20) blend weight ratio. FTIR also confirmed that zein/PVA (80/20) fibre blend was the only miscible blend weight ratio and this was due to stronger intermolecular interactions which were induced via hydrogen bonding. The XRD results illustrated that zein/PVA (80/20) fibre blend displayed no peak associated with the polymers that suggested that the zein/PVA (80/20) fibre blend favored complete miscibility. The TGA and DTA curves confirmed that zein/PVA fibre blends were thermally stable and endothermic. Therefore, the enhancement of electrospinnabilty and mechanical strength of zein was dependent on the presence of PVA.

Iron oxide nanoparticles were effectively synthesized by hydrothermal method and manganese oxide nanoparticles were successfully prepared in a single step precipitation method. Temperature had a significant influence on the structural, optical and thermal stability of the nanoparticles. The detailed structural characterizations revealed that α-Fe_2O_3 nanoparticles were well defined nanocubes at 140 ºC with crystal size of 27.97 nm .The α-Mn_2O_3 nanoparticles calcined at 800 ºC produced rod-spherical shaped nanoparticles with a crystal size of 27.89 nm. The TGA curves showed that nanoparticles synthesized at high temperatures were thermally stable.

The SEM results of the nanocomposites showed that the addition of α-Fe_2O_3 and α-Mn_2O_3 nanoparticles into zein/PVA (80/20) fibre blend weight ratio increased the conductivity of the solutions which led to improved morphology and increased surface area to volume ratio. Therefore concentration of 5.25 wt% of the metal oxide nanocomposites showed that increment of nanoparticle loading had an effect on the nanocomposites fibre morphology and average diameter. The XRD patterns showed that there were no visible crystal peak of the nanoparticles embedded onto the zein/PVA fibre blends hence the nanoparticle loading concentrations were below XRD detection limit. The FTIR spectra of the nanocomposite fibres and composite fibre blends gave almost similar features. The TGA curves showed a significant effect on the thermal properties of the nanocomposites due to the concentration loading of nanoparticles onto zein/PVA (80/20) fibre blends. Therefore zein/PVA (80/20), 5.25 wt% of α-Fe_2O_3/zein/PVA and α-Mn_2O_3 /zein/PVA were the optimum nanocomposites utilized for adsorption studies due to improved morphology, optical properties and thermal stability.

Adsorption studies carried out in a batch system on the effects of contact time, pH and initial concentration were investigated. Both equilibrium and kinetic studies were undertaken. Langmuir isotherm was found to be suitable for chrysoidine G adsorption onto zein/PVA (80/20) fibre blend, α-Fe_2O_3/zein/PVA and α-Mn_2O_3/zein/PVA nanocomposite adsorbents. The pseudo second-order kinetic explained the kinetic data well. Indicating that the adsorption of chrysoidine was dominated by chemisorption. All three nanoadsorbents showed that the equilibrium data were best described by the Langmuir model. The α-Fe_2O_3/zein/PVA nanocomposite was considered the most effective nanoadsorbent for the uptake of chrysoidine G hence it possessed the highest adsorption capacity (366, 5 mg/g), correlation coefficient of pseudo second order (R^2 = 0.9998) and Langmuir isotherm model (R^2 = 0.9824). Therefore the

chosen polymeric materials were promising adsorbents for the removal of chrysoidine G from wastewater. The adsorbent materials were cost effective, easily available, hence, this process is expected to be economical.

5.2. Recommendations

The effect of voltage on all zein/PVA fibre blend weight ratios can be explored in order to understand the influence of applied voltage on the morphology and average diameters of the polymer fibre blends. Adsorption studies of the fabricated material onto chrysoidine G should be explored.

The study was supposed to show how the interaction between the polymer, nanocomposites and chrysoidine dye occurs. However, it is still a challenging subject to most researchers. Therefore the study can explore the chemical bond interaction between electrospun metal oxide nanoparticles embedded onto polymer fibre blends, the composite fibres and chrysoidine G.

This study did not explore leaching and desorption studies of zein/PVA fibre blend and the α-Fe_2O_3/zein/PVA and α-Mn_2O_3/zein/PVA nanocomposites. Therefore leaching and desorption studies of the polymer fibre blend and nanocomposites can be explored.

The behaviour, adsorption equilibrium and kinetics of further studies needs to be done in order to understand metal oxides (Mn and Fe) embedded onto zein/PVA fibre blends for the adsorption of chrysoidine G and R dye. Higher concentrations of nanoparticles embedded onto the polymeric nanoadsorbents can be explored in order to understand the effect on morphology, crystal size, thermal stability and chemical composition of the adsorbents.

Appendix A

The α-Fe_2O_3 nanoparticles were analyse using UV-visible spectroscopy and were dispersed in deionized water. **Fig. 3-13** (b) and (c) showed UV-visible spectroscopy and Tauc plot results of α-Fe_2O_3 nanoparticles prepared at 110 °C and 140 °C . For α-Fe_2O_3 nanoparticles prepared at 110 °C it displayed two peaks at 472 nm and 563 nm, the peaks were observed to be red shifted with a band edge of 563 nm suggesting that at low temperature there was a decline in the band gap, and the particle size were smaller (Reda, 2011). **Fig. 3-13** (b) and (c) showed the α-Fe_2O_3 nanoparticles prepared at 140 °C which displayed a peak at 324 nm, the peak was blue shifted with a band edge of 551 nm suggesting that as the temperature increased there was an increase in nucleation due to the increment of the particle size. It might also be due to the prolonged duration during the reaction or slight excess of water content in the preparation of the α-Fe_2O_3 nanoparticles solution. The optical band gap (Eg) for hematite nanoparticles can be determined by extrapolation from the absorption edge which is given by the following equation (Shen *et al.*, 2012):

$$(\alpha h\nu)^{n} = A\,(h\nu - Eg)$$

Where α is the absorption coefficient, A is constant, hν is the energy of light and n is a constant depending on the nature of the electron transition (Beranek & Kisch, 2008). Hematite has a direct band gap (n=2) (Lassoued et al., 2017). **Fig. 3-13** (c) showed the band gap energies were 2.20 eV (α-Fe_2O_3 at 110 °C)and 2.25 eV (α-Fe_2O_3 at 140 °C) which are respectively, close to the typical literature values for the indirect band gap of α-Fe_2O_3 (1.9 ~ 2.2 eV) (Wheeler *et al.*, 2012).

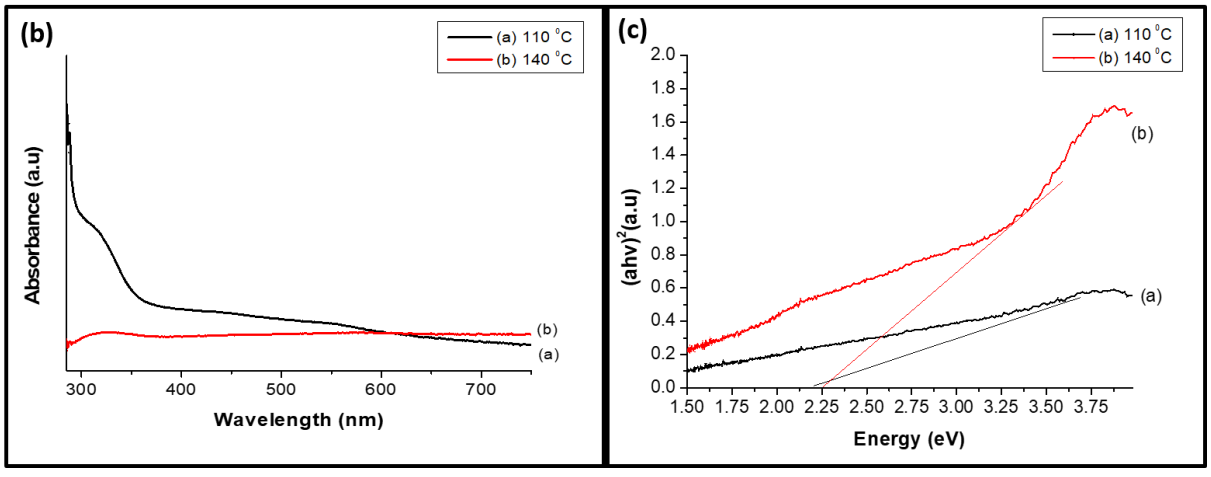

Fig. 3-13. (b) UV spectrum and (c) Tauc plot for direct transitions of Fe_2O_3 nanoparticles synthesized by hydrothermal process.